

Diplomarbeit

# A Tunable Bose-Einstein Condensate in a Three-dimensional Optical Lattice Potential

zur Erlangung des akademischen Grades  
eines Magisters der Naturwissenschaften  
vorgelegt von

Gabriel Rojas Kopeinig

Institut für Experimentalphysik  
der Naturwissenschaftlichen Fakultät  
der Leopold-Franzens-Universität Innsbruck

Juni 2007



# Contents

<b>1</b>	<b>Introduction</b>	<b>1</b>
<b>2</b>	<b>Creating a Bose-Einstein Condensate of a Dilute Cesium Gas</b>	<b>5</b>
2.1	What is a BEC? . . . . .	5
2.2	Why Cesium? . . . . .	5
2.2.1	Scattering . . . . .	6
2.2.2	Feshbach Tuning . . . . .	7
2.3	Producing a Cesium BEC . . . . .	8
2.3.1	Experimental Setup . . . . .	9
2.3.2	Experimental Sequence . . . . .	11
<b>3</b>	<b>Optical Lattice Potentials</b>	<b>15</b>
3.1	Theory . . . . .	15
3.1.1	Dipole Potential . . . . .	15
3.1.2	Periodic dipole potentials . . . . .	17
3.2	Experimental Setup . . . . .	22
3.2.1	Laser System . . . . .	23
3.2.2	Light Control . . . . .	24
3.2.3	Optical Fiber . . . . .	27
3.2.4	Aiming at the atomic ensemble . . . . .	32
<b>4</b>	<b>BEC in an Optical Lattice Potential</b>	<b>39</b>
4.1	Theoretical Introduction . . . . .	39
4.1.1	Band structure, Bloch and Wannier functions . . . . .	39
4.1.2	Bose-Hubbard Model . . . . .	43
4.1.3	Superfluid to Mott Insulator Transition . . . . .	46
4.1.4	Loading of a BEC into the Lattice Potential . . . . .	50
4.2	Testing and Characterizing the Lattice . . . . .	55
4.2.1	Bloch Oscillations . . . . .	55
4.2.2	Measuring the Lattice Depth . . . . .	57
4.2.3	Lattice-induced Heating . . . . .	62
4.3	Experimental Observations of the Mott Insulator Transition . . . . .	68
4.3.1	Driving the Transition via the Lattice Depth . . . . .	68
4.3.2	Driving the Transition via the Scattering Length . . . . .	71
4.3.3	Probing the Excitation Spectrum . . . . .	74



# 1 Introduction

The development of quantum theory in the early half of the last century paved the way for major advances in many scientific fields. Although there is still controversy on its interpretation, the theory successfully predicts the behavior of the microscopic world with many of its intriguing phenomena. In an attempt to observe some of the predicted quantum phenomena on a more 'macroscopic' scale, experimentalist had to find ways on how to reduce or even freeze out thermal excitations. The development of laser cooling techniques gave birth to the field of ultracold atomic gases with its first sensational breakthrough in 1995, the creation of Bose-Einstein condensates (BEC) in dilute atomic alkali gases [And95, Dav95]. This feat was recognized with the Nobel prize in 2001 for Eric Cornell, Wolfgang Ketterle and Carl Wieman. Since then, atomic quantum gases have led to new developments and research efforts well beyond traditional atomic, molecular, and optical physics. Atomic quantum gases have opened up new fields that investigate matter wave lasers and nonlinear matter wave optics, and they have contributed to diverse areas such as condensed matter physics, plasma physics, quantum information and, recently, quantum chemistry. Experimental highlights include the observation of matter wave interference from independent condensates [And97], the first realization of a matter wave amplifier [Ino99], the excitation of matter wave solitons and vortices [Den00, AS01], and the direct observation of the quantum phase transition from a superfluid to a Mott insulator [Gre02a]. For quantum gases with fermionic atoms, the first realization of a degenerate Fermi gas [DeM99] in 1999 was an important milestone.

The success of experiments with ultracold atomic and molecular gases is the result of an exceptionally high degree of experimental control over most, if not all degrees of freedom and the ability to prepare very 'clean' systems in well defined states. In fact, the control over the quantum degrees of freedom is so high that one can speak of 'quantum engineering' of wavefunctions. Internal and external degrees of freedom for atoms in an ultracold gas can be manipulated using magnetic, radio-frequency and optical fields in such a way that coherence can be preserved while the system is shielded from the potential perturbations of the environment. It has now become routine to control the interaction properties of atoms via magnetic and also optically induced Feshbach resonances.

Alkali atoms, such as Li, K, Na, Rb, and Cs, are still used in the majority of neutral atom quantum optic experiments. Due to their single valence electron, they have the simplest electronic structure. Cesium was first treated as a prime candidate for condensation [Tie92], but as a result of an unusually high two-body loss rate, it is not suited for experiments relying on evaporation in magnetic traps.

Therefore an all optical approach is used in the Cs BEC experiments here in Innsbruck [Web03b, Ryc04]. The great advantage of Cs is that it features a combination of broad and narrow Feshbach resonances at technically easily accessible magnetic fields of a few ten Gauss [Chi00]. This offers great tunability of the interaction and enables the production of pure molecular quantum gases [Her03]. Optical trapping allows the preparation of atomic samples in the lowest internal quantum state, which is immune to inelastic two-body processes, and also permits to fully exploit the tunability.

An additional and very attractive prospect is the possibility to spatially order the atoms. The optical dipole force offers the ability to create periodic lattice potentials for neutral ultracold atoms in one, two or three dimensions. Lattice potentials can serve a wide variety of purposes, like the investigation of phenomena known from solid state physics, e.g. the observation of Bloch oscillations [BD96], the suppression of atomic or molecular collisions [Tha06] or the implementation in laser cooling, e.g. sisyphus cooling.

Loading a BEC into an optical lattice opens the possibility for a great number of exciting experiments. So far, the experimental highlights with optical lattices include macroscopic quantum interference from atomic tunnel arrays [And98], number squeezing in a 1D lattice [Orz01], quantum phase transition from a superfluid to Mott insulator [Gre02a], collapse and revival of the matter wave field [Gre02b], and repulsively bound pairs in an optical lattice [Win06].

This is the point where the work presented in this diploma thesis ties up to. By loading a *cesium* BEC into an optical lattice, we gain experimental access to yet another key parameter in the investigation of the involved many body dynamics. The capability to tune the atomic interaction properties at will, allows a new generation of experiments. The superfluid (SF) to Mott insulator (MI) transition can now not only be driven by varying the lattice depth, but also by tuning the atomic interaction strength. This setup also offers the possibility to investigate the properties of the MI phase as a function of the interaction. Or along the same lines, the evolution of the MI state while ramping the scattering length to zero or to negative values can be explored. In continuation of the measurements involving Bloch oscillations in a 1D lattice, we can now study the interaction-induced decoherence effects. The combination of the MI state and tunability of the atomic interaction strength allows for a controlled association of dimer and possibly trimer molecules, enabling the measurement of collisional properties for two or three atoms a time. It may also serve as a starting point for the realization of ground state molecules.

The thesis is organized as follows. In chapter 2, a brief summary on how we create a BEC of a dilute Cs gas is given. The particular properties of Cs are introduced, followed by an overview of the experimental setup and of the experimental sequence as used for the creation of the BEC.

Chapter 3 presents the work that I was mostly involved with during my time as a diploma student, the implementation of a three-dimensional (3D) optical lattice. The theoretical background for the creation of a periodic dipole potential is

reviewed in the first part, whereas the technical details are described in the second part of chapter 3. A special emphasis is given to the challenges encountered when working with relatively high laser powers.

Chapter 4 comprises the presentation of the first experiments using the optical lattice. For better understanding, the theoretical basics describing the single and many particle physics in a lattice are briefly reviewed. Then, the relevant characterization measurements, like the calibration of the lattice depth, are described. The main section of this chapter covers the observation of the quantum phase transition from the superfluid (SF) to the Mott insulating (MI) regime. It reports on our ability to drive the transition by changing the lattice depth, and the promising indications that we are also able to drive the transition by varying the interaction strength. The latter is unprecedented so far, and should allow us to examine the dynamics of the SF to MI transition from a different perspective. Last but not least, the measurement in which we probe the excitation spectrum of the system in the MI regime is described.

Finally, chapter 5 gives a short summary of the work presented here, and a brief but exciting outlook on future experiments.



# 2 Creating a Bose-Einstein Condensate of a Dilute Cesium Gas

## 2.1 What is a BEC?

Bose-Einstein Condensation (BEC) in a gas of particles obeying Bose statistics was predicted by Einstein in 1924 [Ein25]. His work was based on the ideas of Bose addressing the statistics of photons [Bos24]. The prediction basically stated, that if noninteracting atoms were cooled below a critical temperature, the whole atomic ensemble would start behaving as *one* big matter wave, strikingly demonstrating the wave nature of matter. A BEC of a weakly interacting dilute gas of Rubidium atoms was experimentally first demonstrated 71 years after Einstein's publication [And95]. Such a system provides an unique opportunity for exploring quantum phenomena on a macroscopic scale.

To produce a BEC in a dilute gas, the atoms have to be cooled to extremely low temperatures of around 1/1,000,000 degree Kelvin above the absolute zero. For this a whole range of sophisticated laser cooling techniques have been developed in the 80's and 90's. The realization of a BEC requires a complex experimental setup, including a vacuum chamber, different laser systems for cooling and/or trapping, magnetic fields for trapping and/or manipulation of the internal states, an imaging system and a control unit.

## 2.2 Why Cesium?

- Cesium is an atom of particular interest in physics. It has various important applications in fundamental metrology, such as in measurements of the fine-structure constant [Hen00], of a possible electric dipole moment of the electron [Chi01b], parity violation [Bou82], and in measurements of the Earth's gravitational field [Sna98]. Furthermore, due to its large hyperfine splitting in the ground state, it serves as our primary frequency standard [BIP98]. By definition, one second is 9,192,631,770 periods of the microwave transition associated with the hyperfine transitions of the ground state.
- Cesium is very suitable for laser cooling applications. Due to its large mass, the recoil energy is very low. The laser cooling transitions can be readily

addressed by low-cost diode laser systems. This and the technical significance made cesium an interesting and a very promising candidate for Bose-Einstein condensation [Tie92]. However, the particular scattering properties complicate the condensation process substantially, and so the first successful attempt to condense Cs was carried out here in Innsbruck [Web03b], seven years after the first realization of Bose-Einstein condensation of  $^{87}\text{Rb}$  atoms in 1995 [And95].

- Cesium is an excellent candidate for experiments with tunable interaction. For Cs in its absolute electronic ground state, the scattering length can be varied via 'Feshbach tuning'. This provides a unique opportunity to gain experimental access to a key parameter in the investigation of ultracold atoms, the interaction energy.

### 2.2.1 Scattering

Scattering is a result of the interaction between two or more colliding particles. Understanding the possible collision processes is essential for experiments with ultracold gases. For two-body scattering one can basically distinguish between two types of collisions:

- The Good: Elastic scattering, it leads to a redistribution of kinetic energy without changing the internal state of the atom. This type of collision is responsible for the thermalization of an atomic ensemble. It is fundamental for evaporative cooling.
- The Bad: Inelastic scattering, it changes the internal state of at least one of the involved atoms. This type of collision usually leads to loss and heating of the atomic cloud.

In general, the theoretical description of scattering process requires the exact knowledge of the corresponding two-body interaction potential. In the case of ultracold gases and BEC's the involved scattering energies are extremely low. This fact reduces the description of the elastic scattering properties to just one parameter, the *s-wave scattering length*  $a_s$ . It directly characterizes the interaction between the atoms: A positive scattering length corresponds to repulsive interaction, and a negative  $a_s$  implies attractive interaction. For the case of ultra-low energies, where  $ka_s \ll 1$ , with  $\hbar k$  being the relative momentum between two particles, the elastic cross section becomes

$$\sigma(k) \simeq 8\pi a_s^2, \quad (2.1)$$

in analogy to a hard-sphere scattering with a radius  $a_s$ . Note that in this regime the elastic cross section is independent of  $k$ .

Inelastic two-body collisions can be endothermic or exothermic, respectively converting kinetic energy into potential energy or vice versa. Endothermic collisions are usually excluded in our experiments due to the low kinetic energy available

at  $\mu\text{K}$ -temperatures. An exothermic collision mainly occurs as a result of a spin-exchange process (with the total  $m_F$  conserved) or, in particular for Cs, due to the magnetic dipolar interaction (in a spin relaxation process with the total  $m_F$  not being conserved). These type of collisions release energy into the sample and cause heating and/or loss from the trap. For this reason, we work with Cs atoms in the absolute electronic ground state ( $F = 3, m_F = 3$ ), where all inelastic two-body collisions are fully suppressed. For a detailed description of the basic principles I refer the reader to one of many review articles on this subject, e.g. Ref. [Dal99].

In the absence of inelastic two-body collisions the dominant loss mechanism is due to three-body recombination [Web03c]. It is the process of two atoms forming a dimer molecule in a collision with a third atom. The third atom needs to be present to satisfy momentum and energy conservation. In the context of atom trapping, three-body recombination primarily leads to particle loss, but it also leads to heating of the sample. Luckily, Bose-Einstein condensation occurs in a regime where densities are sufficiently low so that the probability for a three-body recombination event is rather small. Condensates can have lifetimes of 30 s and beyond, quite often limited by collisions with the background gas and not by internal processes. For Cs, the three-body loss rate coefficient  $L_3$  is on the order of  $10^{28} \text{ cm}^6/\text{s}$  [Kra06]. The atom density should then be well below  $10^{14} \text{ atoms}/\text{cm}^3$  to allow for sufficiently long lifetimes for the atomic sample.

## 2.2.2 Feshbach Tuning

For inelastic collisions the incident and outgoing scattering wave functions experience different interaction potentials. These potentials are also called entrance and outgoing channels. If the energy of an outgoing channel is lower than the total energy of the incident channel, inelastic exothermic collisions to that channel are possible. This channel is then called open channel. If the energy of the outgoing channel is higher, inelastic scattering to this channel is not possible. It is therefore called a closed channel. Since the two colliding atoms in ( $F = 3, m_F = 3$ ) have the lowest internal energy, there are no open channels available. However, closed channels can also alter the (elastic) scattering parameters dramatically.

Usually, as illustrated in Fig. 2.1, it is sufficient to consider two channels, an entrance channel and a closed channel with a single molecular bound state. A Feshbach resonance [Ino98] occurs when the state of two free atoms in the entrance channel is allowed to couple to the closed channel with a molecular bound state. For this, the bound state has to be brought into degeneracy with the entrance channel, usually by means of an external magnetic field and the Zeeman effect, making use of the fact that different channels have different magnetic moments. As the energy level of the molecular state approaches that of the entrance channel, the scattering length  $a_s$  diverges. If the molecular state is close to but below (above) the energy of the incident state, the scattering length is large and positive (negative). The coupling between entrance channel and closed channel is the result of strong electronic interactions such as the exchange interaction and weaker dipole-

dipole and spin-orbit interactions. The former interaction preserves orbital angular momentum and leads to strong s-wave Feshbach resonances, the latter leads to weaker higher-order d-wave, g-wave, etc. Feshbach resonances [Chi04].

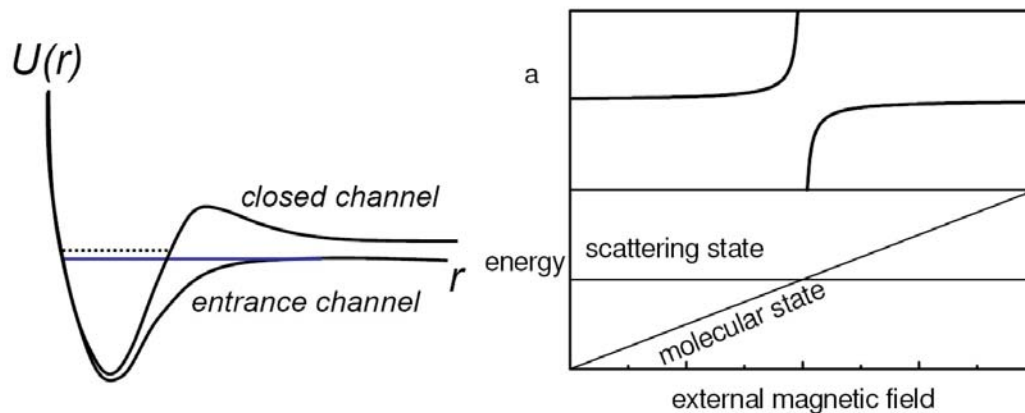


Figure 2.1: The Feshbach resonance scenario: (left) By applying an external magnetic field, the scattering state of two free atoms in the entrance channel can be brought into energetic degeneracy with a molecular state belonging to the closed channel. (right) In the vicinity of the state crossing (bottom) the scattering length  $a$  shows a dispersive divergence (top).

The width  $\Delta B$  of a Feshbach resonance is determined by the magnetic moment of the bound state and the coupling strength between the two states. If the scattering length far from any resonance is  $a_{bg}$  then the scattering length around the resonance position  $B_{res}$  can be calculated by

$$a(B) = a_{bg} \left( 1 - \frac{\Delta B}{B - B_{res}} \right). \quad (2.2)$$

Figure 2.2 shows several Feshbach resonances the  $(F = 3, m_F = 3) \times (F = 3, m_F = 3)$  scattering channel, where  $a_s$  is plotted against the magnetic field  $B$ .

Feshbach resonances offer the possibility to tune the scattering length and thus the interatomic interaction. This is often referred to as *Feshbach tuning*. Feshbach resonances can also be used to create molecules [Her03, Reg03]. A detailed discussion on Feshbach resonances in general and their use as a tool for the production of cold molecules is found in a review by T. Köhler [Köh06]. A discussion on Feshbach resonances particularly for Cs can be found in [Chi01a].

## 2.3 Producing a Cesium BEC

The realization of a Cs BEC requires an involved experimental setup, including a vacuum chamber, different laser systems for cooling and trapping, magnetic fields for the application of magnetic forces and for a control of the interaction strength

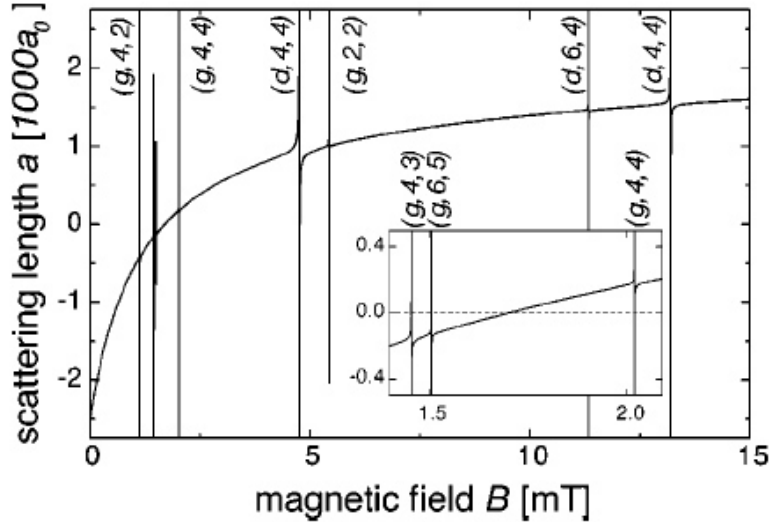


Figure 2.2: Scattering length in units of Bohr’s radius  $a_0$  as a function of the magnetic field for the electronic ground state of cesium,  $F = 3, m_F = 3$ . There is a Feshbach resonance at 48.0 G due to coupling to a  $d$ -wave molecular state. Several very narrow resonances at 11.0, 14.4, 15.0, 19.9 and 53.5 G are visible, which result from coupling to  $g$ -wave molecular states. The quantum numbers characterizing the molecular states are indicated as  $(l, f, m_f)$ . This plot is taken from [Chi01a].

via Feshbach tuning, and an imaging system. A control system switches and adjusts these devices on a micro-second timescale to produce an elaborate experimental sequence with a typical duration of about 10 seconds. This chapter gives a quick overview on our experimental setup and sequence as used for the creation of a Cs BEC. For an further details the reader is referred to the diploma theses of my predecessors [Unt05, Fli06].

### 2.3.1 Experimental Setup

The setup used for this work is the third and newest in a series of cesium BEC experiments performed here in Innsbruck. The layout is basically based on the first generation setup [Web03a, Web03b], with one essential improvement: The experimental chamber made of steel has been replaced by a glass cell, offering, among other things, a greater optical access for the implementation of a three-dimensional optical lattice. Another main advantage is that it also allows for faster switching of the magnetic fields.

#### Vacuum Chamber

Experiments with ultracold gases require that the collision rate with the background gas has to be kept as low as possible. Thus the experiments are performed

within an ultrahigh-vacuum (UHV) chamber, which is comprised of various elements (Fig. 2.3). It can be roughly divided into two sections: The oven section, which consists of the cesium oven, a series of vacuum pumps and a small cell allowing optical access. The main section includes the Zeeman slower, the experimental glass cell and more vacuum pumps. They are joint via a differential pump section to accommodate the pressure difference of more than 7 orders of magnitude ( $\sim 3 \cdot 10^{-4}$  mbar in the oven and  $< 10^{-11}$  mbar in the experimental chamber).

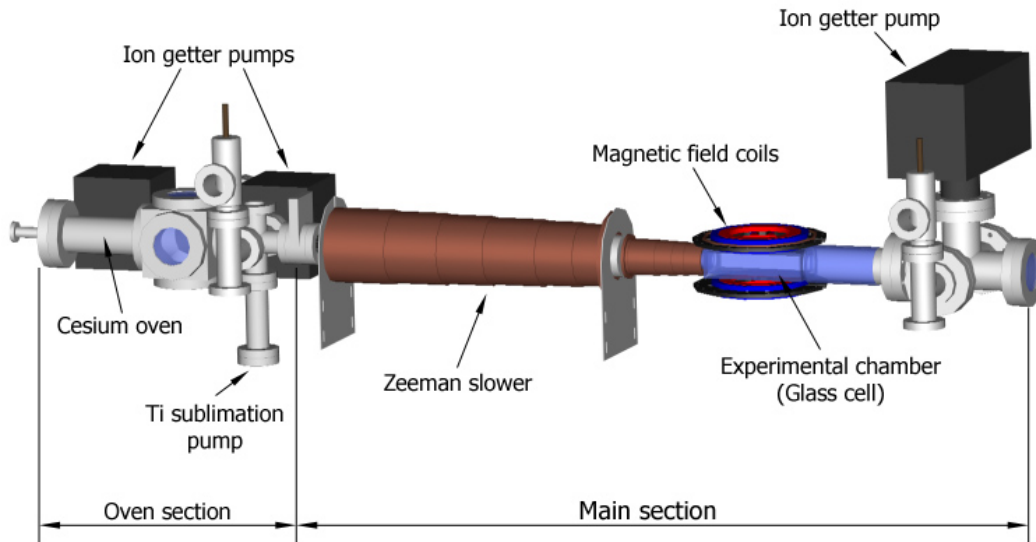


Figure 2.3: Schematic drawing of the vacuum chamber. The apparatus has a length of 180 cm and can be divided into an oven section and a main section. Magnetic coils to generate the gradient and bias magnetic fields surround the glass cell. The compensation coils are not shown.

## Laser Systems

Laser cooling of Cs requires laser light at a wavelength of 852 nm and a line width of  $< 100$  kHz. It is generated by two home-built grating-stabilized diode lasers in Littrow configuration serving as so-called master lasers, and three home-built injection-locked diode lasers, serving as slaves. They provide the light for the following applications: Zeeman slowing, magneto optical trap (MOT) operation, Raman-sideband cooling, and for the imaging system.

The far detuned laser light for trapping the atoms is provided by a commercial high power Ytterbium fiber laser operating at 1070 nm delivering up to 100 W of laser power (model number YLR-100LP, IPG).

## Magnetic coils

The magnitude and direction of the magnetic field plays a key role during the entire experimental sequence. Therefore a total of 16 coils have been installed, forming the following magnetic coil systems:

- Bias and gradient field coils: They can generate bias fields of up to 200 G and field gradients of up to 70 G/cm along the vertical direction. The precise and fast control of these fields is substantial for various applications, e.g. for the MOT, for Feshbach tuning, for atom levitation, etc.
- Compensation coils: These coils enclose the whole main section of the vacuum chamber and are mostly responsible for the compensation of various stray fields, like the earth's magnetic field, or the fields produced by the ion getter pumps. They also control the field during Raman sideband cooling.
- Zeeman slower coils: In combination with the Zeeman laser beam, these coils effectively decelerate the atoms from about 260 m/s to almost zero.

## Imaging system

The atom cloud is imaged using the standard absorption imaging method [Ket99]. A resonant laser beam is shone onto the cloud, producing a shadow image on the chip of a CCD-camera. This image can be directly translated to a (projected) atom density. The pictures are immediately analyzed to give the relevant data, e.g. atom number, atom cloud position and width, etc. The processing and analyzing of the images is performed with a MATLAB-program. Ensemble temperatures are determined by the time-of-flight (TOF) technique.

## Control System

The experimental sequence can be controlled by a computer program written in Visual C++. It was adapted for our setup from the original version developed by F. Schreck [Sch]. The software communicates with the different experimental devices via a computer card (NI6533, National Instruments) and a home-built bus system. The card outputs the digital data onto the bus with 200 kHz, which allows a timing resolution of  $5 \mu\text{s}$ . Currently, we use about 20 analog and 50 digital outputs and 6 direct digital synthesis devices (DDS) connected to the bus system, addressing the numerous experimental devices.

### 2.3.2 Experimental Sequence

The following experimental steps (see also Fig. 2.5) are performed to create a Bose-Einstein condensate of up to 200,000 atoms:

- Zeeman slowing: The atomic beam coming from the Cs oven with a temperature of about 380 K is decelerated from about 260 m/s to a few m/s in 68 cm [Met99]. At this point the atoms are slow enough to be trapped in the following step.
- Magneto-optical trap: Within 2 s around  $2 \cdot 10^8$  atoms are captured in the magneto-optical trap (MOT). For the last 25 ms the detuning is decreased from -10 to -70 MHz in order to spatially compress the atom cloud to a diameter of  $\sim 600 \mu\text{m}$  [Met99]. After this step, the temperature has dropped to about  $45 \mu\text{K}$ .
- Raman sideband cooling: After the compressed MOT, the lasers for Raman sideband cooling (RSC) are turned on. This dark state cooling scheme not only decreases the temperature of the atoms, but also polarizes the atoms into their electronic ground state ( $F = 3, m_F = 3$ ) [Dav94]. After only 6.5 ms the ensemble has reached a temperature of  $\sim 700 \text{ nK}$  at a phase space density of  $\rho \sim 10^{-3}$ . At this point the total atom number has decreased to about  $7 \cdot 10^7$  [Fli06].
- Reservoir trapping: The reservoir trap can be viewed as an intermediate step for loading the atoms into the so-called dimple trap [SK98, Kra04]. It consists of two crossed red-detuned high power laser beams at 1070 nm with a relatively large beam diameter of  $\sim 0.5 \text{ mm}$ . Since the reservoir trap and the subsequent trapping schemes are too weak to hold the atoms against gravity, it is necessary to switch on the magnetic levitation fields at this stage. Imperfect mode matching heats the atoms during the loading of the reservoir trap to a couple of  $\mu\text{K}$ . Therefore the trap is left on for 1 s at a scattering length  $\sim 1500 a_0$ . During this time the hottest atoms evaporate out of the trap. After this process we have about  $1 \cdot 10^7$  atoms at  $\sim 1 \mu\text{K}$  with a phase space density of  $\rho \sim 5 \cdot 10^{-3}$ .
- Dimple trapping: To further increase the phase space density toward the point of condensation, we use the dimple-trick [SK98, Kra04]. Therefore two additional tightly focused laser beams are adiabatically ramped up (Fig. 2.4), creating a dimple in the existing potential of the reservoir trap. This increases the density in the tight dimple trap without an increase in temperature as the atoms in the reservoir trap act as a temperature bath. During this process the scattering length is reduced to  $\sim 470 a_0$  to avoid three-body losses. After the loading of the dimple (1 s) one of the reservoir beams is switched off. This way the atom reservoir is drained, leaving only the compressed atoms in the dimple. With the scattering length set to  $\sim 330 a_0$  (low three-body collision rate) we wait for 300 ms for the ensemble to thermalize. This procedure gives nearly  $1.7 \cdot 10^6$  atoms with a similar temperature than after RSC, but with a phase space density  $\rho \sim 10^{-1}$  that is about two orders of magnitude larger.

- **Forced evaporation:** During this final process the depth of the dimple potential is successively reduced. In 3-4 steps the light power of the dimple beams is slowly ( $\sim 5$  s) ramped down, allowing the hottest atoms to escape. This effectively lowers the temperature of the remaining ensemble. At the point where the ensemble has reached the critical temperature  $T_c \simeq 20$  nK, condensation sets in, and a macroscopic population of the atoms populate the quantum mechanical ground state. This is the actual starting point for the experiments presented in this work.

We usually work with a condensate of about  $1.5 \cdot 10^5$  atoms. At the end of a typical evaporation procedure the trap frequencies of the dimple trap are  $\nu_x = 20$  Hz,  $\nu_y = 18$  Hz, and  $\nu_z = 27$  Hz. The BEC fraction is then around 80% and the Thomas-Fermi radius  $r_{TF} \simeq 13 \mu\text{m}$  (with a scattering length  $a_s$  of  $210 a_0$ ).

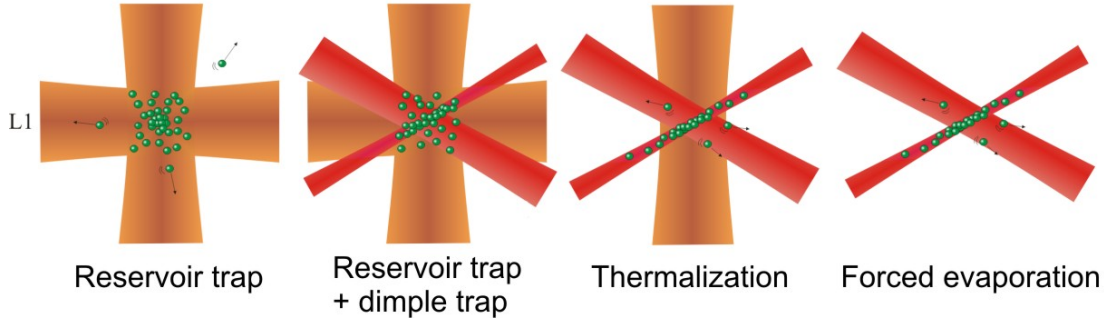


Figure 2.4: Illustration of the dipole trapping stages: In the reservoir trap the atoms are trapped by two crossed high power laser beams with relatively large beam diameters. To increase the phase space density, two additional tightly focused beams are superimposed, effectively increasing the density without raising the temperature, since the atoms in the reservoir act as a temperature bath. Then the atom reservoir is drained by switching off one of the reservoir beams. After some thermalization time, the dimple potential is slowly ramped down, allowing hottest atoms to escape, effectively lowering the temperature of the remaining ensemble.

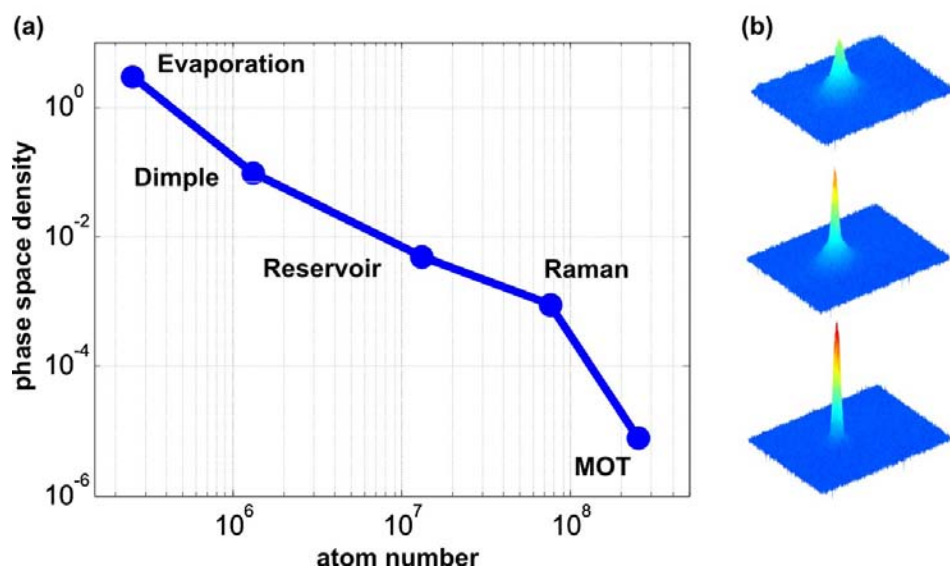


Figure 2.5: Toward a Cs Bose-Einstein condensate. (a) Schematic plot showing phase space density and atom number after the corresponding experimental step. (b) TOF density distribution of the atoms extracted from absorption images, taken after 45 ms of levitated expansion, showing the phase transition from a thermal cloud to a BEC from top to bottom.

# 3 Optical Lattice Potentials

An accessible way of manipulating the external states (e.g., position and velocity) of a neutral atom is through its interaction with an electromagnetic wave. The interaction can be of a dissipative and/or conservative nature. Both are fundamental for our experiments with neutral atoms. Dissipation of energy arises through the absorption of a photon followed by a spontaneous reemission of a photon with a slightly different wavelength. The resulting momentum transfer forms part of the underlying principles of all laser cooling schemes. On the other hand, the interaction of the light-field-induced dipole moment of the atom with the light field itself, can be used to create a conservative potential for the atoms by the way of the so-called *ac Stark shift*. This chapter describes how we use this fact to create a three-dimensional lattice potential.

## 3.1 Theory

### 3.1.1 Dipole Potential

In this section we will recapitulate the results for the dipole potential due to the conservative part of the interaction between the light field and light-field-induced dipole moment. We will also introduce the basic equations for the photon scattering rate and show that the residual photon scattering can be neglected for the case of a far-detuned optical trap. For a more detailed discussion please refer to one of the more comprehensive review articles, e.g. [Gri00].

#### Two-level atoms in a near-resonant trap

The following expressions for dipole potential  $V_{dip}$  and scattering rate  $\Gamma_{sc}$  can be used for optical traps with a laser frequency that is relatively close to an atomic resonance. These traps can be considered far-detuned in the sense that the detuning  $\Delta$  is large with respect to the atomic line width  $\Delta \gg \Gamma$ . However, the absolute value of the detuning has to be much smaller than the resonance frequency  $|\Delta| \ll \omega_0$ , since the rotating wave approximation (RWA) has been applied to obtain

$$V_{dip}(\mathbf{r}) = -\frac{3\pi c^2}{2\omega_0^3} \frac{\Gamma}{\Delta} I(\mathbf{r}) \text{ and} \quad (3.1)$$

$$\Gamma_{sc}(\mathbf{r}) = \frac{3\pi c^2}{2\hbar\omega_0^3} \frac{\Gamma^2}{\Delta^2} I(\mathbf{r}). \quad (3.2)$$

Here,  $c$  is the speed of light,  $\Delta = \omega - \omega_0$  is the detuning of the laser frequency  $\omega$  from the atomic resonance frequency  $\omega_0$ ,  $\Gamma$  is the linewidth of the atomic transition corresponding to the spontaneous decay rate of the excited state, and  $I(\mathbf{r})$  is the spatial laser light intensity distribution.

For our setup with a 1064 nm light source, the requirement for the rotating wave approximation  $|\Delta| \ll \omega_0$  is not really fulfilled, so that errors in the order of 10% and 50% respectively would be made (see Tab 3.1). Nevertheless, Eq. (3.1) and (3.2) help us to stress two important points:

- Sign of detuning: Atoms that are in the light field of a red detuned ( $\Delta < 0$ ) laser beam will be attracted to positions of maximum intensity, whereas atoms in a blue detuned light field ( $\Delta > 0$ ) will be drawn to positions of minimum light intensity. Therefore we can use the dipole-force to order atoms in space by applying laser light with spatially modulated intensity.
- Scaling with intensity and detuning: Both the dipole potential and the scattering rate, scale linearly with the light intensity, but the potential is proportional to  $1/\Delta$ , whereas the scattering rate exhibits a  $1/\Delta^2$  dependence. That means that one can create deep potentials with low scattering rates by using laser light with high intensity and large detuning from atomic resonance.

### Multi-level atoms in a far off-resonant trap

For optical traps that are far off the atomic resonance, the above relations become erroneous. Not only because  $|\Delta| \not\ll \omega_0$ , but also because one has to consider a multi-level atom with more complex transition structure. In our case, the detuning  $\Delta$  is of the order of the fine-structure splitting but much larger than the hyperfine splitting  $\Delta_{FS} \approx |\Delta| \gg \Delta_{HFS}$ , so that we can ignore the unresolved hyperfine substructure. This means that the polarizability  $\alpha$  is only significantly different for the (unresolved)  $D_1$  and  $D_2$  transitions, so that we can average the dipole potential for the  $D_1$  and  $D_2$  line weighted with the line strength factors of  $\frac{1}{3}$  and  $\frac{2}{3}$  respectively. We obtain

$$V_{dip}(\mathbf{r}) = -\frac{1}{3} \frac{3\pi c^2}{2\omega_{0D1}^3} \left( \frac{\Gamma_{D1}}{\omega_{0D1} - \omega} + \frac{\Gamma_{D1}}{\omega_{0D1} + \omega} \right) I(\mathbf{r}) - \frac{2}{3} \frac{3\pi c^2}{2\omega_{0D2}^3} \left( \frac{\Gamma_{D2}}{\omega_{0D2} - \omega} + \frac{\Gamma_{D2}}{\omega_{0D2} + \omega} \right) I(\mathbf{r}) \quad (3.3)$$

for the dipole potential, and

$$\Gamma_{sc}(\mathbf{r}) = \frac{1}{3} \frac{3\pi c^2}{2\hbar\omega_{0D1}^3} \left( \frac{\omega}{\omega_{0D1}} \right)^3 \left( \frac{\Gamma_{D1}}{\omega_{0D1} - \omega} + \frac{\Gamma_{D1}}{\omega_{0D1} + \omega} \right)^2 I(\mathbf{r}) + \frac{2}{3} \frac{3\pi c^2}{2\hbar\omega_{0D2}^3} \left( \frac{\omega}{\omega_{0D2}} \right)^3 \left( \frac{\Gamma_{D2}}{\omega_{0D2} - \omega} + \frac{\Gamma_{D2}}{\omega_{0D2} + \omega} \right)^2 I(\mathbf{r}) \quad (3.4)$$

for the scattering rate.

At this point it should be noted that these results only account for E fields with linear polarization and that for circular polarization the line strength factors depend on the magnetic quantum number  $m_J$ , and on the sign of the rotation ( $\sigma^+$  or  $\sigma^-$ ). See review of dressed state approach [Gri00]. In other words, the ac Stark shift depends not only on the intensity, but also on the state of polarization ( $\pi, \sigma^+, \sigma^-$ ) (see e.g. sisyphus effect [Gui99]).

## Typical Values

To conclude this chapter some values for realistic beam parameters are given in Tab. 3.1. It is always convenient to specify the potential depth in energy units of possible perturbations. When working with ultra cold gases in dipole potentials a possible perturbation is a photon scattering process. Therefore units of recoil energies

$$E_r = \hbar^2 k^2 / 2m, \quad (3.5)$$

where  $m$  is the atom mass, and  $k = 2\pi/\lambda$  the wave vector of the laser light, are used throughout this work.

For a Cesium atom and a laser wavelength of  $1064 \text{ nm}$  it can be converted as follows:

$$1 E_r = 8.78 \cdot 10^{-31} \text{ J} = 64 \text{ nK} = 1325 \text{ Hz}$$

	853 nm		1064 nm		10000 nm	
	no RWA	with RWA	no RWA	with RWA	no RWA	with RWA
$V_{dip}$	$8450 E_r$ $840 \mu\text{K}$	-0.01%	$10.4 E_r$ $660 \text{ nK}$	-9.3%	$307 E_r$ $220 \text{ nK}$	-46%
$\Gamma_{sc}$	$2 \cdot 10^4 \text{ s}^{-1}$	+0.02%	$4 \cdot 10^{-3} \text{ s}^{-1}$	+51%	$5 \cdot 10^{-7} \text{ s}^{-1}$	+400%

Table 3.1: Potential depth and photon scattering rate for a Cs-atom in a Gaussian laser beam with a power of 1 W, a waist of  $500 \mu\text{m}$  and different wavelengths. The values are calculated without rotating wave approximation (RWA). The respective errors of the RWA are also given. Note that the unit  $E_r$  is not very suitable for comparing potential depths for different wavelengths as it is wavelength dependent itself.

### 3.1.2 Periodic dipole potentials

As we have seen in the previous section, one can use laser beams to trap atoms in positions of maximum light intensity. By creating a spatially intensity-modulated laser light field, e.g. a standing wave, one can produce periodic lattice potentials in 1, 2 or 3 dimensions.

## 1D lattice potentials

The simplest realization of a spatially modulated light field is to let two counter-propagating laser beams interfere. If they have identical wavelengths  $\lambda$  and parallel polarizations, the result is a standing wave with a periodicity in  $z$ -direction of  $\lambda/2$ , with  $\lambda$  being the laser wave length. The E field takes the form

$$E = 2E_0 \cos kze^{-i\omega t}, \quad (3.6)$$

where  $E_0$  is the amplitude of the electric field, and  $k = 2\pi/\lambda$  and  $\omega$  are the wave vector and the frequency of the laser beam with propagation direction  $z$ . In vacuum,  $k$  and  $\omega$  relate via  $k = \omega/c$ . If we also consider the fact that the laser beams have a Gaussian intensity-profile of the form

$$I(r) = I_0 e^{-\frac{2r^2}{w^2}}, \quad (3.7)$$

the potential can be written as

$$V(r, z) = V_{0,1D} e^{-\frac{2r^2}{w^2}} \cos^2 kz. \quad (3.8)$$

Here  $r$  is the radial distance from the beam center,  $I_0 = \frac{2P}{\pi w^2}$  is the peak-intensity,  $w = w(z) = w_0 \sqrt{1 + (z/z_R)^2}$  is the  $\frac{1}{e^2}$ -radius (waist) of the beam,  $z_R = \pi w^2/\lambda$  is the Rayleigh length and  $V_{0,1D} = 4V_{dip}(r = 0)$  is the maximum potential depth in the 1D lattice. The potential  $V_{dip}(r = 0)$  is calculated from Eq. (3.3) for  $I_0$ . Because of the  $|E|^2$ -dependence we obtain a four times deeper dipole potential for two interfering beams, than for a single beam. As we are only interested in spatial

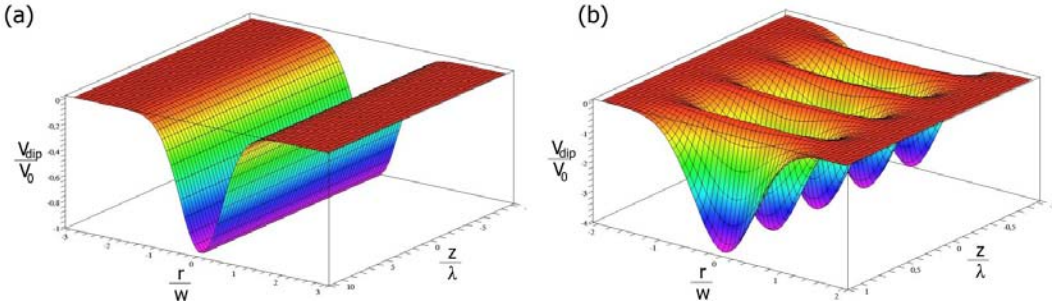


Figure 3.1: Illustration of a dipole potential for a Gaussian laser beam (a) and a 1D lattice potential formed by two counter-propagating Gaussian laser beams (b).

regions of the order of the waist  $w_0 \ll z_R$ , we will neglect the  $z$ -dependence of the waist in the following discussions.

## 2D lattice potentials

The standard way to create a periodic lattice in two dimensions is to superimpose two pairs of counter-propagating beams in an orthogonal configuration. (See

Fig. 3.2 for the effect of different angles between orientation and polarizations of the two beam-pairs.) Assuming identical amplitudes for the four beams, the E field can be expressed as

$$\begin{aligned} E &= E_{00}(\mathbf{e}_1 e^{i(kx - \omega t + \varphi_x)} + \mathbf{e}_1 e^{i(-kx - \omega t + \varphi_x)} + \mathbf{e}_2 e^{i(ky - \omega t + \varphi_y)} + \mathbf{e}_2 e^{i(-ky - \omega t + \varphi_y)}) \\ &= 2E_{00}(\mathbf{e}_1 \cos kx + \mathbf{e}_2 \cos ky e^{i(\varphi_y - \varphi_x)}) e^{i\omega t}, \end{aligned} \quad (3.9)$$

with  $\mathbf{e}_1$  and  $\mathbf{e}_2$  being the polarization vectors of the beam pairs in x- and y-direction, respectively. Since we are only interested in length scale on the order of the atomic cloud we will neglect the Gaussian beam profile. For equal frequencies the potential takes on the form:

$$V(x, y) = V_{01D}(\cos^2 kx + \cos^2 ky + 2\mathbf{e}_1 \cdot \mathbf{e}_2 \cos \Delta\varphi \cos kx \cos ky) \quad (3.10)$$

We can see that in general the result still depends upon the phase difference between the beam-pairs  $\Delta\varphi = \varphi_y - \varphi_x$ , making it sensitive to phase fluctuations. To avoid this undesired effect (which could lead to heating of the atoms) one can choose orthogonal polarizations between the standing waves so that  $\mathbf{e}_1 \cdot \mathbf{e}_2$  vanishes. As one can see in Fig. 3.2 the effective potential depth (being the potential barrier from one lattice site to the nearest) is four times smaller than for parallel polarization vectors in this case, but it makes a experimentally involved implementation of a phase-stabilization unnecessary (see Fig. 3.3). Instead, or additionally to the orthogonal polarizations, one can introduce a slight frequency difference (MHz) between the two laser beams. In this case the potential varies its depth and form on a  $\mu\text{s}$  time scale, which is much too fast for the atom to follow. The time-averaged potential 'seen' by the atoms is then identical to a potential produced with two standing waves with orthogonal polarizations.

### 3D lattice potentials

In general a 3D optical lattice can be realized in many different ways. In [Pet94] it is shown that the Bravais lattice is determined from the propagation directions of the laser beams while, the basis is associated with the polarizations of the incident waves. In the 'standard tetrahedron' configuration one could generate a three dimensional lattice with only four beams, but because we want to accommodate a 1D, 2D and 3D lattice with the same experimental setup, we use six beams to form three standing waves that are mutually orthogonal. Again, to be insensitive to phase fluctuations, one can set the polarizations between the standing waves to be mutually orthogonal, or one can offset the frequencies between the different standing waves by a few MHz by means of acousto-optical modulators. Both methods create a simple cubic lattice potential for the atoms with a periodicity of  $\lambda/2$  (see Fig. 3.4). The resulting lattice potential is just the sum of three independent 1D lattice potentials (see Eq. 3.8), so that we can write

$$V(x, y, z) = V_{01D,x} e^{-2\frac{y^2+z^2}{w_x^2}} \cos^2 kx + V_{01D,y} e^{-2\frac{x^2+z^2}{w_y^2}} \cos^2 ky + V_{01D,z} e^{-2\frac{x^2+y^2}{w_z^2}} \cos^2 kz. \quad (3.11)$$

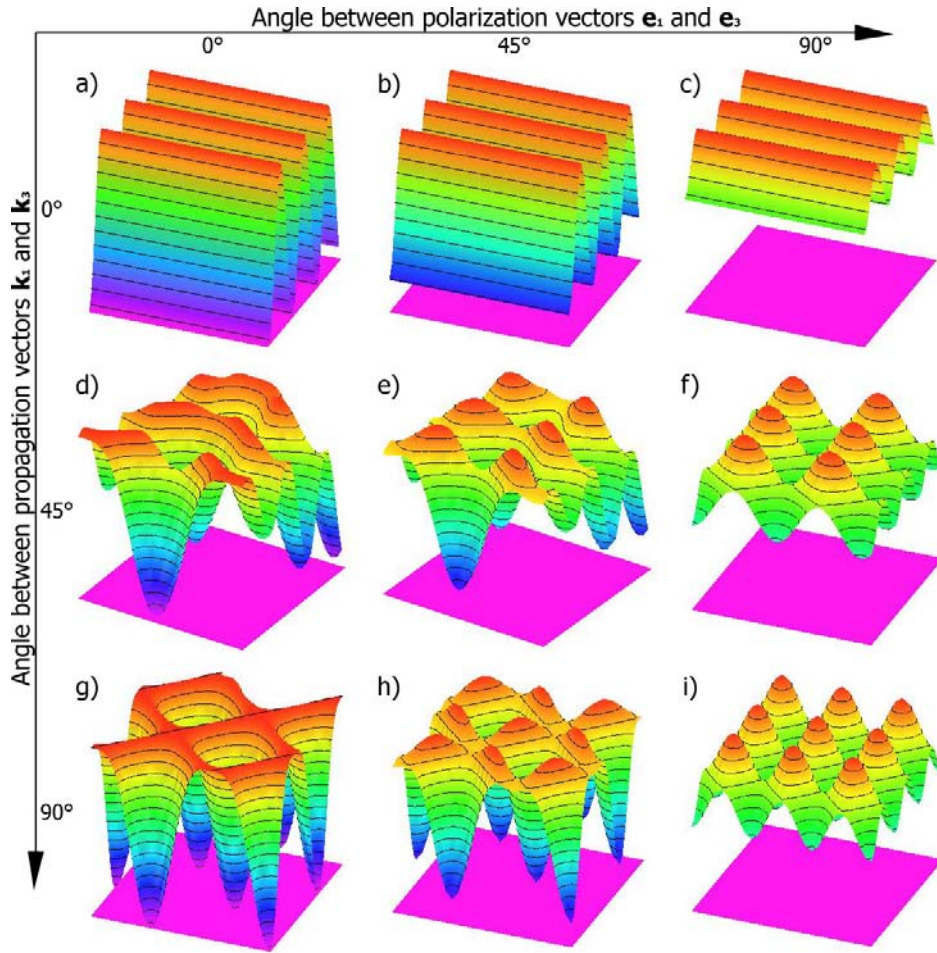


Figure 3.2: 2D lattice potentials formed by two pairs of counterpropagating beams for different configurations. Here  $\mathbf{k}_1 = -\mathbf{k}_2$ ,  $\mathbf{k}_3 = -\mathbf{k}_4$ ,  $\mathbf{e}_1 = \mathbf{e}_2$  and  $\mathbf{e}_3 = \mathbf{e}_4$  are the wave- and polarization-vectors of the four plane waves.

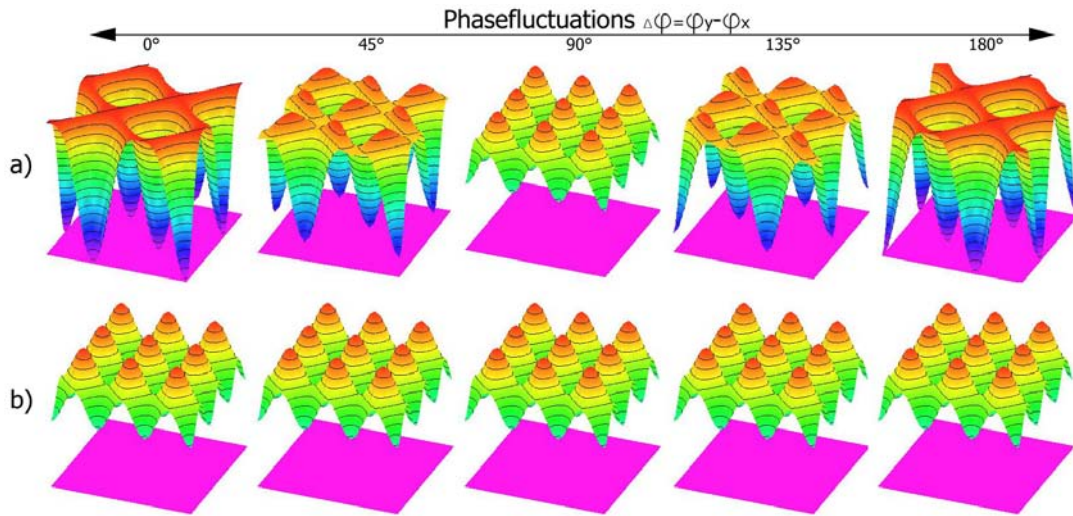


Figure 3.3: 2D lattice potentials for two orthogonal standing waves for various phase differences  $\Delta\varphi$  with a) parallel polarizations and b) orthogonal polarizations

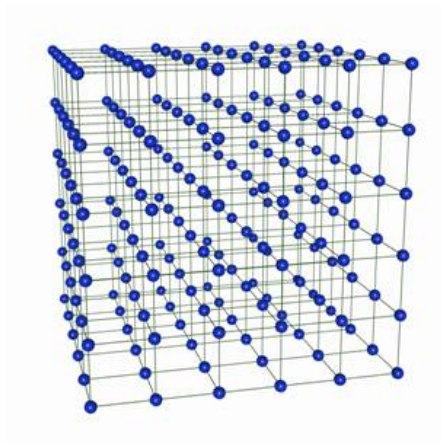


Figure 3.4: Schematic illustration of the equipotential surface of a simple cubic lattice as formed by superimposing three orthogonal standing waves.

Here  $V_{0_{1D,x}}$ ,  $V_{0_{1D,y}}$  and  $V_{0_{1D,z}}$  are the maximum potential depths for 1D lattices formed by counter-propagating laser beam pairs in x, y and z direction respectively. Remember that, e.g.  $V_{0_{1D,x}} = 4V_{dip_x}$  is the potential barrier between lattice sites in x direction, generated by *two* interfering beams each with intensity  $I_{0_x}$ , with  $V_{dip_x}$  being the potential depth created by *one* single beam in x direction with intensity  $I_{0_x}$  (see Eq. [3.3]).

### Typical Values

The following table 3.2 is intended as a quick reference for the expected lattice depth for a laser wavelength of  $1064\text{ nm}$ . Note that, if the standing waves have mutually orthogonal polarizations or are mutually detuned, then the potential barrier to the nearest neighbors in a 2D or 3D lattice is the same as in a 1D lattice. Whereas the potential barrier to the next neighbor in diagonal direction (in the plane spanned by two standing waves, e.g., in x and y direction) is then  $V_{0_{1D,x}} + V_{0_{1D,y}}$ , and in the direction of the space-diagonal (for a 3D lattice only) the potential barrier is  $V_{0_{1D,x}} + V_{0_{1D,y}} + V_{0_{1D,z}}$ . Throughout the rest of this work, if not otherwise stated, the term lattice depth refers to the (physically significant) potential barrier between nearest neighbor sites  $V_{0_{1D}}$  (at the center of the Gaussian beams) rather than to the actual potential depth. Obviously, this lattice depth can be different for each lattice axis.

Laser Power $P$	Beam Waist $w$	Lattice Depth $V_{0_{1D}}$
1 W	$500\ \mu\text{m}$	$41.6 E_r$
$P$ in W	$w$ in $\mu\text{m}$	$41.6P \left(\frac{500}{w}\right)^2$ in $E_r$

Table 3.2: Lattice depth calculated for a laser wavelength of  $1064\text{ nm}$  for a one-dimensional lattice, corresponding to the potential barrier between nearest neighbors for a multi-dimensional lattice with mutual orthogonal polarizations or mutual detuning.

## 3.2 Experimental Setup

The general idea for the experimental implementation of a 1D, 2D or 3D optical lattice is very simple: One takes 1, 2 or 3 laser beams (from a single or different sources) and creates a standing wave for each desired dimension by just retro-reflecting each beam on a mirror as shown in Fig. 3.5.



Figure 3.5: A simplified picture on how to create a one-dimensional optical lattice

The actual realization is a bit more involved: One needs to take into account the usual components for the ability to control and adjust the laser light, e.g. acousto-optic modulators (AOM's), lenses, adjustable mirrors and so on. Because there is only a limited amount of space around the experimental chamber, we built the light source and necessary hardware to split and control the laser light a couple of meters away from the glass cell (see Fig. 3.6). For increased stability in terms of beam pointing and for better beam-profile quality, the laser light is guided to the experimental chamber using optical fibers. We chose to create two standing waves by retro-reflection, and the third by interfering two counter-propagating beams. This allows us to accelerate the lattice along one direction, a feature that will be used in future experiments.

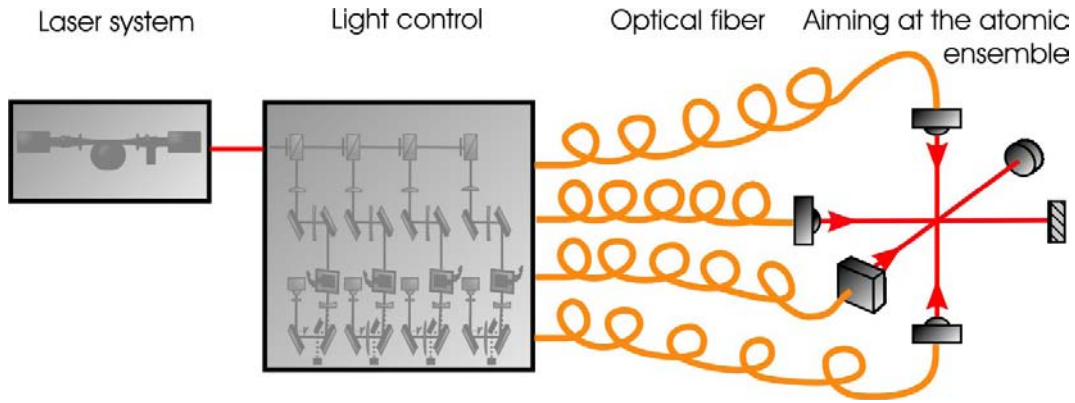


Figure 3.6: Schematical drawing of the experimental setup divided into its four main parts: laser system, light control, optical fibers, and aiming at the atomic ensemble.

The following sections describe the technical aspects of the experimental setup in more detail. Table 3.3 shows summarizes of the requirements that had to be taken into account.

Requirements		Dependence	Measures	
lattice depth	$V_0 > 30 E_r$	$\propto P \left( \frac{1}{\Delta w^2} \right)$	high power	$P \sim 1 \frac{W}{\text{beam}}$
scattering rate	$\Gamma_{sc} < 10^{-1} \text{ s}^{-1}$	$\propto \frac{1}{\Delta^2} \left( \frac{P}{w^2} \right)$	far detuned	$\lambda = 1064 \text{ nm}$
uniform lat. depth	$\frac{\Delta V_0}{V_0} < 5\%$	$\propto \left( \frac{1}{w^2} \right)$	large b. waist	$w \sim 500 \mu\text{m}$

Table 3.3: Table showing the requirements on the experimental setup and their dependence from the laser beam power  $P$ , the detuning  $\Delta$ , and the beam waist  $w$ . The chosen and the corresponding values are also shown.

### 3.2.1 Laser System

A uniform lattice depth of up to  $50 E_R$  would be desirable. For beam diameters of about 1 mm one thus needs around 1.25 W of optical laser power per beam.

Having four beams (two retro-reflected and two counter-propagating) and with a total transmission efficiency of the optical components of roughly 50%, we need a laser output of  $>10$  W. For this purpose the light of a commercial narrow band Nd:YAG laser at 1064 nm (model name Mephisto, Innolight) is amplified by a home-built Ytterbium-doped large-mode-area fiber [AL03], providing up to 15 W of narrow-band light. The output beam is collimated to a waist of about  $900 \mu\text{m}$ . With a line width of about 1 kHz, this light source exceeds the required coherence length of a couple of meters by many orders of magnitude. Further details will be available in [Hal].

### 3.2.2 Light Control

Experiments with optical lattices require good control over the applied laser light. One needs to be able to ramp and switch the light intensity on a  $\mu\text{s}$ -timescale which can easily be done with acousto-optic modulators (AOM's). Because the use of optical fibers always introduce intensity fluctuations (see next chapter), an active stabilization of the light intensity is essential.

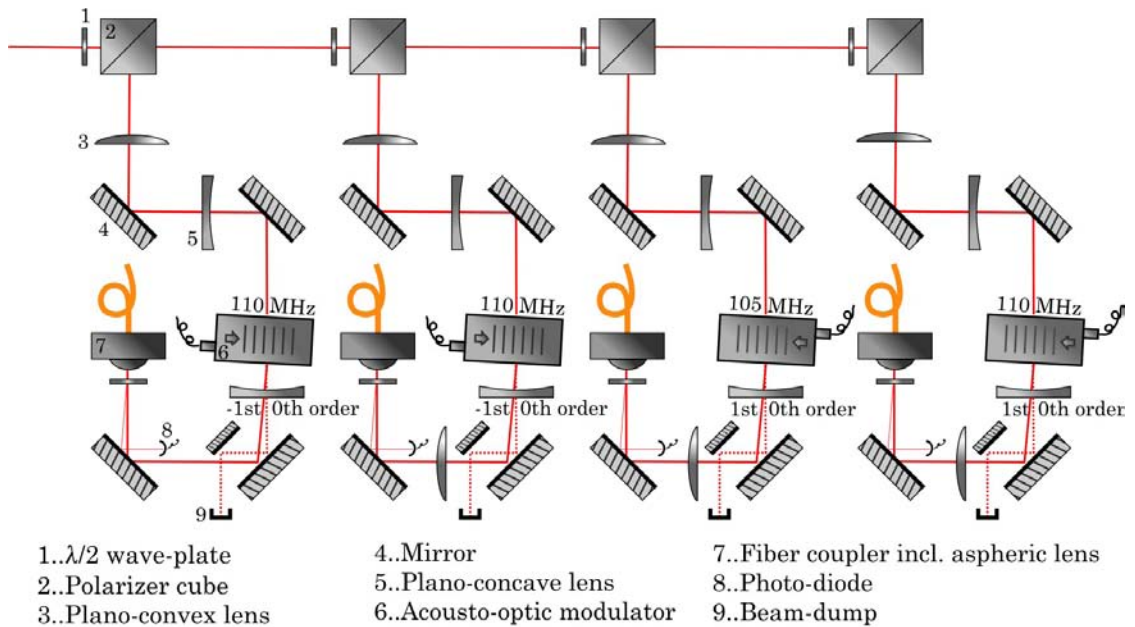


Figure 3.7: Schematical drawing of the optical setup used to control the laser light.

#### General Setup

The collimated beam from the fiber amplifier is split into four beams using thin-film polarizer cubes (model number G335723000, Linos). The ratio of the intensities of the divided beams can arbitrarily be chosen by placing a  $\lambda/2$ -waveplate in front of each polarizer cube (see Fig. 3.7). For an efficient AOM operation a  $1/e^2$ -beam

waist of about  $500\ \mu\text{m}$  is needed. Therefore the waist is reduced by means of a telescope. The diffracted beam (the  $1^{\text{st}}$  or  $-1^{\text{st}}$  order) is then expanded with a pair of lenses to obtain the necessary mode-matching for a efficient air-fiber coupling. This is critical, since the damage threshold of the fiber decreases with the coupling efficiency (see section 3.2.3). A  $\lambda/2$ -waveplate is placed in front of the fiber-coupler to match the polarization axis with the fast axis of the polarization-maintaining fiber.

## Mirrors

We use standard dielectric mirrors with high-reflectivity coatings at 1064 nm. They have the highest reflectivity for light with the linear polarization direction perpendicular to the plane of incidence (s-polarized), and they are designed to be used at an angle of  $45^\circ$  to the beam. These facts were taken into account whenever possible. One must also consider that the reflected light experiences a different phase-jump for its s- and p-component. For reasons that are described later, it is important to maintain the linear polarization of the light. Therefore one must exclusively use the mirrors for s- or p-polarized light.

## AOM / rf-driver / PI-control

An AOM uses the acousto-optic effect to diffract the beam and to shift the frequency of light using sound waves in a crystalline material. These sound waves are generated by a piezo that needs to be driven with a radio-frequency (rf) signal. The AOM's used in our setup (model number 3110-197, Crystal Technology) require power of up to 2.5 W at a center frequency of 110 MHz. Their bandwidth is 15 MHz. The rf-signal is generated by a direct digital synthesis device (DDS, model number AD9852, Analog Devices) [Mey], which can be directly addressed by the experiment control program to set frequency and amplitude to the desired values. This signal is amplified in two steps to a maximum power of 34 dBm. The home-built amplifier circuit includes a variable attenuator, which is used to stabilize the light intensity after the optical fiber to a desired value with a proportional-integral (PI) control circuit. (See Appendix A for the electronic circuits.) The transmitted light power is deduced via a photo-diode (PD) that is placed behind the first mirror after the optical fiber (see Fig. 3.13 and Fig. 3.14). Because the mirrors have a reflectivity of about 99.5% and because we work with intensities of the order of 1 W, the 'leaking' light is sufficient to be detected by a regular PD. The desired light power can be entered in the experiment-control-program and is passed on to the PI-control through a digital analog converter (DAC). A useful feature of the PI-control is, that the stabilization can be switched on and off (sample and hold mode) during the experimental sequence. When the stabilization is on, the ramping speed of the lattice depth is limited by the PI-control ( $\sim 500\ \mu\text{s}$ ). For measurements where faster switching is required (see e.g. sec. 4.2.2), the stabilization is turned off during ramping.

## Thermal effects

A serious problem are the thermal effects of the AOM when it is switched on abruptly. This effect is especially pronounced when the AOM is cold. It is due to the heat generated by the rf-signal, causing thermal dilation of the AOM crystal. The effect manifests itself, among other things, in a spatial drift of the diffracted beam on timescale on the order of a couple of seconds. As a consequence, the fiber coupling efficiency decreases, which can, if one tries to switch high-power laser light, permanently damage the optical fiber. See section 3.2.3 for a more detailed discussion of the damage threshold of the fiber. This beam pointing error can be reduced if the AOM is placed in the focus of two lenses forming a telescope, resulting in a fairly small beam waist at the position of the AOM. For a wavelength of 1064 nm, the AOM's need a relatively large beam waist ( $> 500 \mu\text{m}$ ) to obtain decent diffraction efficiencies. Therefore we chose a trade-off where we positioned the AOM in the collimated beam with a waist of  $400 - 450 \mu\text{m}$ , and tried to minimize the optical distance between AOM and fiber-coupler.

## Damage threshold of optical components

As we are working with laser beams with up to 15 W of power, one has to consider the manufacturer-specified damage threshold of the optical components used in the setup. Table 3.4 summarizes the collected data on damage threshold for several components.

Component	Specified DT	Applied peak-int.	Comment
Cube(PBS)	2 kW/cm <sup>2</sup>	$\sim 1.2\text{kW}/\text{cm}^2$	thin film polarizers, Linos
$\lambda/2$ -waveplate	2 MW/cm <sup>2</sup> unknown	$\sim 1.2\text{kW}/\text{cm}^2$ $\sim 1.2\text{kW}/\text{cm}^2$	multi-order, Thorlabs <sup>1</sup> multi-order WP, Casix
Lenses	unknown	$\sim 2\text{kW}/\text{cm}^2$	BK7 with AR-coating, Casix
AOM	10 MW/cm <sup>2</sup>	$\sim 2\text{kW}/\text{cm}^2$	Crystal Technology
Aspheric lens	100 W/cm <sup>2</sup>	$\sim 400\text{W}/\text{cm}^2$	for fiber coupler, Thorlabs <sup>2</sup>

Table 3.4: Specified damage threshold (DT) and applied laser intensities for the optical components used in our setup. <sup>(1)</sup> Reflections from other optical components melted the glue in the mounting. Therefore these waveplates were replaced by ones with a bigger aperture from Casix Inc. <sup>(2)</sup> According to the information provided by customer support, the DT is limited by the AR-coating. Although we are exceeding the specified DT, we have not observed any signs of damage.

## Thermal lensing

An unforeseen and limiting problem is the gradual decrease of available laser power. In a time frame of a couple of weeks, the fiber coupling efficiency continuously

diminishes from its initial value of  $\sim 80\%$  to only 60%, 50%, or even 40%. It can not be restored by re-aligning the beam that is coupled into the fiber. As it turns out, the problem stems from the fact that a 'milky' looking layer 'grows' on the optical components with high intensity exposure. In our setup the  $\lambda/2$ -waveplates and polarizer cubes after the fiber amplifier are mostly affected. We assume that this layer is responsible for an increased absorption of light on the surface of the component, reducing the transmittance, and creating some sort of a thermal lensing effect. Thermal lensing occurs as a result of a temperature gradient causing a density gradient in the optical material. Because of the Gaussian profile of the laser beam, the temperature gradient caused by absorption can produce a lensing effect. Hence, the beam diameter and the beam divergence is altered resulting in a reduced mode-matching of the beam-fiber coupling. We believe, that the formation of the layer is due to an enhanced dust deposition under the influence of the light force, as we have only observed it on the incident face. The layer can be removed with the usual cleaning agents (e.g. methanol), restoring the initial fiber coupling efficiency. For some unknown reason, the deposition is stronger on  $\lambda/2$ -waveplates than on the polarizer cubes. Although the deposition of dust is the most probable explanation of this effect, it is very surprising that it occurs in a clean laboratory environment. The setup is on an optical table, that is covered and equipped with a flow box. So far, the only effective measure is to clean the affected components every couple of weeks.

### 3.2.3 Optical Fiber

In its most simple form, an optical fiber is a glass fiber designed to guide light along its length by total internal reflection. The use and demand for optical fibers has grown tremendously and optical-fiber applications are numerous, ranging from telecommunication, biomedicine, military, industrial, and many other applications, including quantum optic experiments.

Except for the fiber-amplifier sec. 3.2.1, we use standard single-mode (SM) fibers to guide the laser light from its source to the region of interest. Their use, allows for a spatial separation of laser source and experiment without an increase of the beam-pointing error due to mechanical instabilities. SM fibers also filter the laser beam from unwanted higher order spatial modes, reducing the beam to one with an exactly defined intensity profile, a Gaussian distribution. The drawback is that a considerable amount of light power is lost at the air-fiber interface. Even the best fiber coupling efficiencies hardly exceed 90%, with typical values ranging from 60% to 80%. The laser light that is not coupled into the fiber is mostly absorbed, limiting the total amount of transmittable laser power.

For our optical lattice setup we require a single-mode (SM) fiber that can transmit up to  $\sim 3$  W of optical laser power. The general rule of thumb is -or better was- that a standard SM fiber, like the ones typically used in our group, has a damage threshold of about 1 W. As it turned out no special measures were required and the fiber used, a standard SM fiber, fulfills our requirements. Nonetheless, this chapter

summarizes the knowledge gained, and points out possible methods to increase the damage threshold of a SM fiber.

### **What limits the damage threshold of a typical fiber?**

The 'burning' of a fiber is a self-enhancing process. A certain fraction of the laser light focused onto the fiber-tip is absorbed (rather than coupled into) and generates heat in the direct vicinity of the air-fiber interface. Excessive absorption can be caused by imperfect mode-matching or dirt on the fiber tip. If the threshold temperature of the epoxy, used to glue the fiber to the connector, is surpassed it will melt and burn locally, which will worsen the coupling efficiency because of two reasons: The produced gases will deposit on the air-fiber interface and the mode-matching worsens because the fiber can move in the melted glue. Therefore the decreasing coupling efficiency translates into a continuously increasing amount of absorbed light power until the fiber-tip cracks or burns away. One needs to keep in mind that, although we are talking of optical powers of only a couple of Watts, the beam is focused to a diameter of about only  $5\ \mu\text{m}$  (equivalent to the core of the fiber). The resulting light intensities are of the order of tens of  $\text{MW}/\text{cm}^2$ .

### **Options to increase the damage threshold**

- Use of a large-mode-area (LMA) fiber: This type of fiber has, as its name indicates, a larger core and is also available for SM operation. Since it has a larger mode-area the light intensity is reduced, and therefore the damage threshold is increased.
- High-power connectors: The idea behind the design of high-power connectors is straightforward: The vicinity of the fiber-tip is kept free of any absorbing material like especially epoxy. This is nicely realized in the air-gap style connectors as shown in Fig. 3.8. The main disadvantages from our point of view is that it complicates the process of connectorizing substantially. The connector face of this connector style can not be polished as usual to obtain a clean end-face after gluing. Instead the fiber-end must be cleaved which basically eliminates the possibility of having an angled end. Some companies claim to make angled cleaves, although not for polarization maintaining fibers. For fibers without an angled end undesirable interference effects can arise within the fiber due to back-reflections at the fiber ends. Other companies specialized in making patchcords (a fiber with connectors on both ends) use a trick in which the air-gap is filled with a soluble epoxy for polishing and is washed out afterward. Since both these methods are technically quite involved, the use of high power connectors for home made patchcords was not feasible for us.

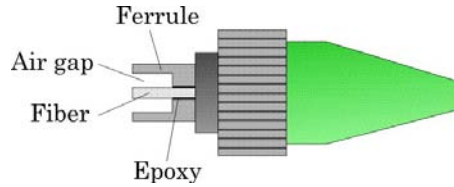


Figure 3.8: Air-gap style connector for high power applications

- Passive end-caps: Another method to decrease the light intensity at the air-fiber interface (and therefore to increase the damage threshold) is to put a passive end-cap on the end-faces of the fiber. It consists of a short piece of core-less fiber that is spliced, the fiber-specific expression for 'welded', onto the fiber-end as shown in Fig.3.9. This way no dirt particle can be deposited in the spot of the tightest focus (the fiber-end-face) and the beam waist at the air-fiber interface is increased for a  $\sim 0.5$  mm long end-cap by more than a factor of 10. Although this protects the fiber effectively from damage due to inefficient coupling as a result of dirt, it does certainly not protect the fiber from damage as a result of bad mode-matching. By applying passive end-caps, the NA of the fiber is not altered.

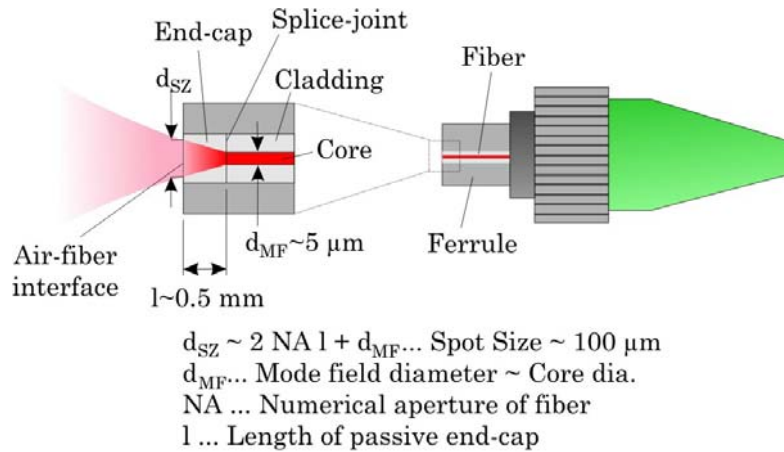


Figure 3.9: Schematic drawing of a connectorized fiber with a passive end-cap

### Polarization maintaining fibers

In general the form of polarization, linear or circular, and the orientation of the polarization vector of the guided light in an optical fiber is not maintained. This is obviously not desirable if the light is used to generate a standing wave. Additionally, if polarization-selective optics are used after the out-coupler, variations of the polarization axis would directly translate into intensity fluctuations. These variations, that are due to temperature fluctuations and acoustic perturbations of the fiber, can be suppressed by the use of a polarization maintaining (PM) fiber.

Such a fiber possesses a pair of 'stress rods', a certain geometric variation of the refractive index in its cladding (see Fig. 3.10). These stress rods effectively create a slow and a fast axis in the fiber. If the direction of polarization of the light that is coupled into the fiber coincides with the slow or fast axis of the PM fiber, the orientation of the polarization axis of the out-coupled light is maintained within an angle of  $\pm 3^\circ$  or  $\pm 5^\circ$  respectively and the intensity fluctuations can be reduced to 3 – 5%. The fluctuations are usually on a minute timescale, but they can be accelerated (e.g. for testing) by heating the fiber, e.g. with a hair dryer. To suppress the remaining  $\sim 5\%$  we actively stabilize the light intensity with a PI-controller.

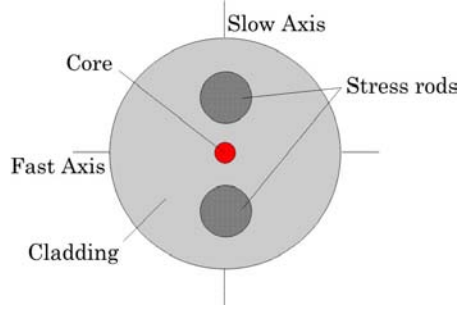


Figure 3.10: Cross section of a polarization maintaining fiber

### Coupling efficiency

Throughout this work the coupling or fiber efficiency  $\eta_{coupling}$  simply refers to

$$\eta_{coupling} = \frac{P_{before}}{P_{after}},$$

with  $P_{before}$  and  $P_{after}$  being the laser power before and after the fiber. As the damage threshold directly depends on the coupling efficiency, some care should be taken when coupling the light into the fiber. Given the numerical aperture and the core diameter of the fiber, the beam diameter and the focal length of the collimating lens need to be chosen accordingly. The following straightforward relations can be used to obtain a set of parameters [Bes99, New]:

$$d_{SZ} = \frac{4\lambda f}{\pi d_B} \sim d_{MF}$$

$$NA_{rays} \sim \frac{d_B/2}{f} < NA_{fiber}$$

Here  $d_{SZ}$  stands for spot size of the focused laser beam at the fiber end face,  $f$  is the focal length of the lens used, and  $d_B$  is the beam diameter at the lens. The mode field diameter  $d_{MF}$  is a measure of the width of the guided mode and is similar to the core diameter of the fiber.  $NA_{rays}$  is the numerical aperture of the

focused beam and  $NA_{fiber}$  is the numerical aperture of the fiber. Fig. 3.11 shows the possible beam diameters that fulfill these two relations for three different lenses for a LMA fiber. For the type of fiber used in our setup (see below) we expanded the four beams to a diameter of  $1.8\text{ mm}$  and used aspheric lenses with  $f = 11\text{ mm}$ . This way a maximum efficiency of  $88\%$  was achieved, with typical values being around  $80\%$ .

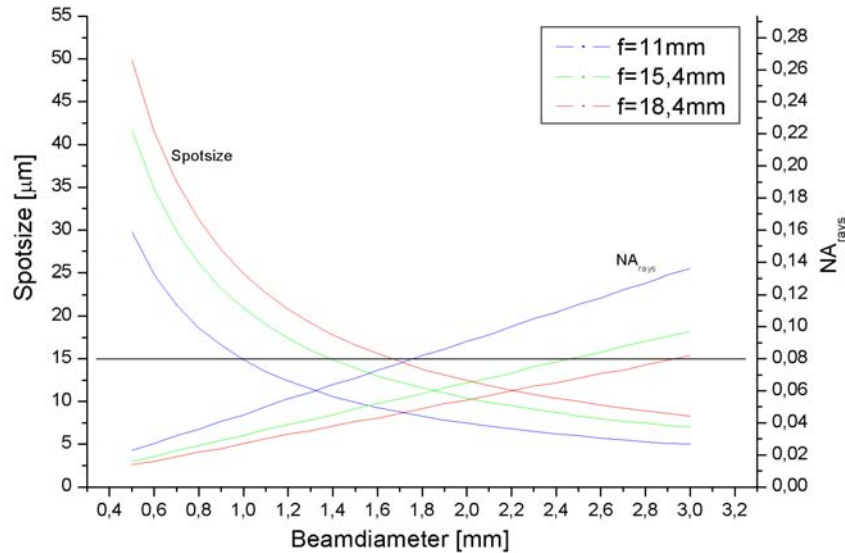


Figure 3.11: Determining the right parameters for a good coupling efficiency. This plot is made for large-mode-area fiber with a core diameter of  $15\ \mu\text{m}$  and a NA of  $0.08$ . The beam diameter must be chosen such, that the resulting spot size, and the NA of the rays for the chosen lens is smaller than indicated by the black line.

### The fiber chosen

We tested home made patchcords with and without passive end-caps and we looked into using LMA fibers, but as it turned out none of the above mentioned high power measures were necessary for our requirements and so the simplest option was chosen. We now use a standard polarization-maintaining single-mode fiber (Nufern PM980-HP) with a mean-field-diameter of  $6.6\ \mu\text{m}$ , for a nominal wavelength of  $980\text{ nm}$ , and a second mode cut-off wavelength of  $900\text{ nm}$ . We terminated the fiber with standard FC/APC connectors. In high-power tests performed at a laser wavelength  $1064\text{ nm}$ , we were not able to destroy the fiber with laser powers of up to  $5\text{ W}$ . But one has to keep in mind that the fiber coupling efficiency may deteriorate during long term operation from the original  $\sim 80\%$ . For this reason we deliberately reduced the coupling efficiency to  $50\text{-}60\%$  several times for a couple of seconds.

During operation one should always keep an eye on the evolution of the fiber efficiency. If it drops below a critical value of around 60% the transmittance of laser powers  $> 1\text{ W}$  should be avoided or at least limited to short time intervals. For this reason a whole array of photo-diodes (PD) was installed in the setup. For every fiber there is a PD before and after the fiber. They can be used to check the current coupling efficiencies.

### 3.2.4 Aiming at the atomic ensemble

The preparation of a Bose-Einstein condensate with Cs atoms is in itself a major experimental challenge and requires a complex experimental setup [Fli06, Her05]. For this purpose our setup includes 16 laser beams aiming into the experimental chamber. Accordingly, the space around the glass cell is quite valuable, and it gets somehow challenging to find optical access to the region of interest (ROI) in the experimental chamber. This is particularly the case for a 3D-lattice, where one needs optical access from both directions along three mutually orthogonal axes. But optical accessibility was one of the main requirements while planning this third generation Cs-BEC experiment, and therefore a glass cell was chosen (see sec. 2.3.1).

#### General Setup

We decided to arrange the four laser beams for the optical lattice as follows (see Fig.3.12):

- Two mutually orthogonal and retro-reflected beams oriented horizontally at a near  $45^\circ$  angle in respect to the glass cell.
- Two counter-propagating beams along the vertical direction..

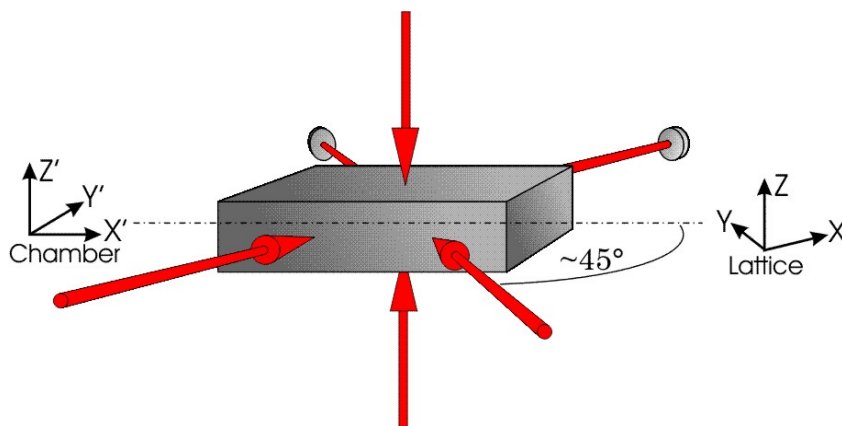


Figure 3.12: Schematical drawing of the beam arrangement in respect to the experimental chamber

The reasons for this arrangement are straightforward: The vertical beams allow for experiments with an 1D-lattice and a variable external force (e.g. the observation of Bloch-oscillations). This way we can use gravity and/or accelerate the lattice by slightly detuning the two counter-propagating beams. For now, the beams deviate about half a degree from a perfect vertical alignment, since it is blocked by the set-up for Raman-sideband-cooling. The near  $45^\circ$ -arrangement ( $\sim 50^\circ$ ) of the vertical beams offered the simplest technical realization, and it has the advantage that we can distinguish between the different momentum peaks in our time-of-flight (TOF) images. (The imaging axis is orthogonal to the long axis of the chamber.)

For the horizontal beams the setup is realized as shown in Fig. 3.13. This setup is installed at the same height as the vacuum chamber and hence some riser-platforms are required. The light is coupled out of the fiber with a waist of around  $900\ \mu\text{m}$  and is then reduced with a pair of lenses to the desired beam-waist of  $500\ \mu\text{m}$  at the ROI. Two mirrors at  $45^\circ$  angle offer the necessary degrees of freedom to align the laser beams with the atom cloud. At the other side of the glass cell another pair of lenses is placed in front of the  $0^\circ$ -mirror to obtain a beam-waist of  $500\ \mu\text{m}$  for the retro-reflected beam at the ROI. An optical isolator protects the fiber from the retro-reflected beam.

The setup for the vertical beams is implemented as shown in Fig. 3.14. The beam with the propagation direction bottom-to-top (beam  $Z_{b-t}$ ) is coupled out of the fiber one level below the glass cell. It passes the optical diode, three mirrors, and a pair of lenses before it is reflected upward into the ROI by a fixed  $45^\circ$ -mirror. This mirror is, as it is also used for other laser beams (MOT, Raman-cooling), a  $2''$  diameter broadband mirror, which only preserves polarization if the incident beam is either s- or p-polarized (see sec 3.2.2). Due to historic reasons, this  $2''$  mirror is mounted such that the propagation direction of the incident beam has to be orthogonal in respect to the long axis of the experimental chamber, for the reflected beam to be vertical. As a consequence we were obliged to choose a polarization axis for the vertical lattice beams that is in  $\sim 45^\circ$  angle to the horizontal lattice beams. This current setup makes a 3D beam configuration with mutual orthogonal polarizations, as mentioned in section 3.1.2, not possible. Since the same effect as with orthogonal polarizations can be achieved by mutually detuning the lattice axes, a beam configuration as shown in Fig. 3.15 was chosen. With a relative detuning in the MHz-range, the atoms 'see' an average potential that is basically identical to one produced with mutual orthogonal polarizations (see Fig. 3.3 (b)).

The setup for the beam with the propagation direction top-to-bottom (beam  $Z_{t-b}$ ) is analogous to its counter-part, except that it is arranged on the breadboard above the glass cell (see Fig. 3.14).

## The aiming process

The lattice beams in our setup have a relatively large waist of around  $500\ \mu\text{m}$ , therefore the aiming process turns out to be quite simple.

1. Pre-alignment:

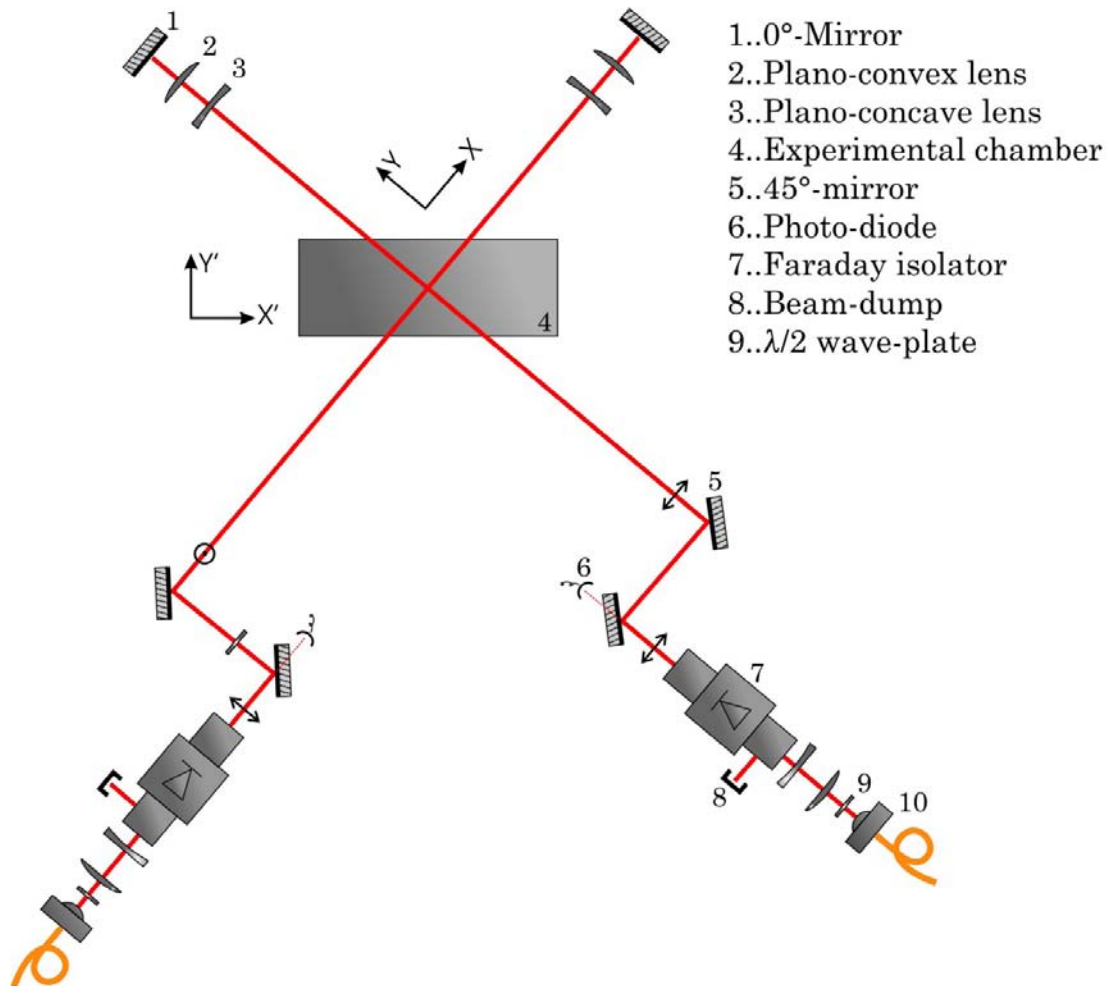


Figure 3.13: Schematical drawing of optical setup of the horizontal lattice beams

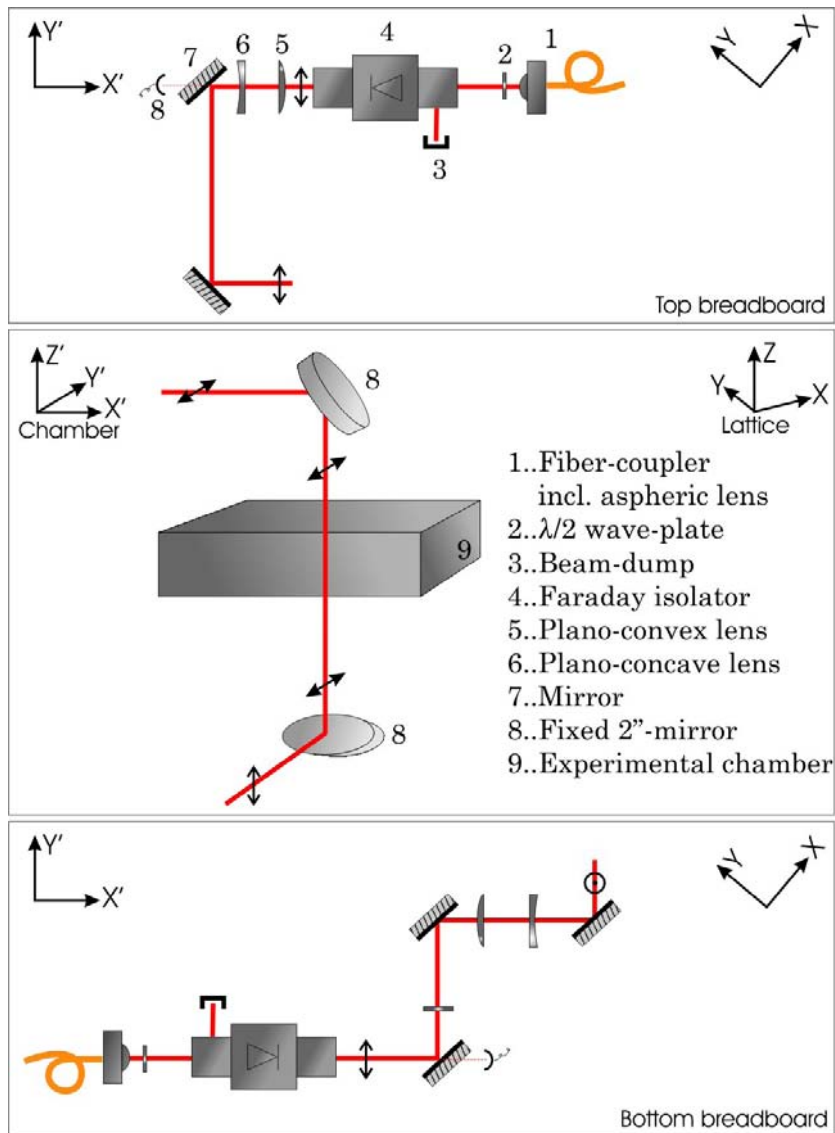


Figure 3.14: Schematical drawing of optical setup of the vertical lattice beams

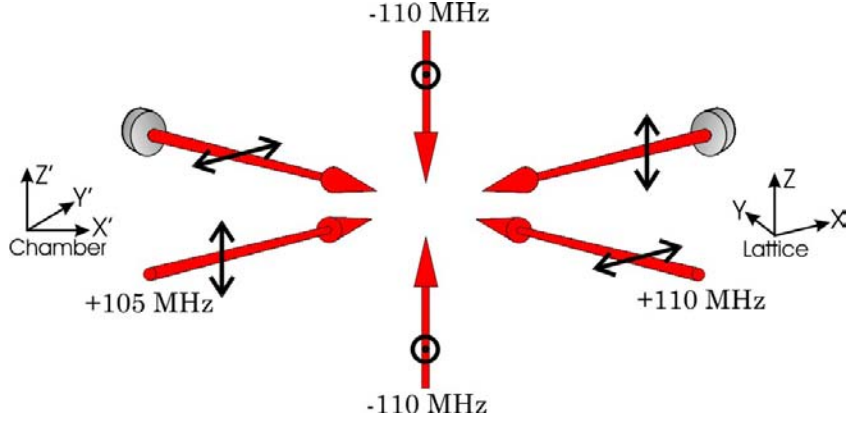


Figure 3.15: Experimentally realized beam configuration including polarization and detuning.

At first we align the beams per eye in respect to the existing -already aligned- beams (e.g. Raman-sideband-cooling). At this and the next step we do neither worry about the retro-reflected nor the counter-propagating beam by blocking the  $0^\circ$ -mirror and by only using one of two Z-beams (e.g.,  $Z_{t-b}$ ).

2. Alignment of incident beams:

Next we aim at the atoms by using the three beams, one by one, as a simple dipole trap without forming a standing wave. We do this by producing samples of ultracold Cs atoms with a temperature of about  $1 \mu\text{K}$  while shining the beam into the experimental chamber. By using a power of up to 2 W we can achieve a dipole potential depth of  $> 1 \mu\text{K}$ . The effect of the beam on the atom cloud is easily seen on the absorption or even fluorescence image after a levitated time-of-flight (TOF) of about 100 ms. As we work with relatively large beam waists, we were usually able to see the effect of the beam even with a bad pre-alignment. At this point one only needs to exactly align the center of the beam with the desired position. The desired position has to be previously marked on the absorption image. It indicates the spatial position in two dimensions of the BEC after evaporation. For aligning the beam along the third dimension, we use a second camera providing fluorescence pictures of the atom cloud from a different angle. See Fig. 3.16 for typical images of this alignment process.

3. Alignment of the retro-reflected / counter-propagating beams:

For the horizontal lattice beams we use the  $0^\circ$ -mirror to couple the retro-reflected beam back into its own fiber. Even with the optical diode adjusted to maximal isolation, one can detect a very weak beam after the AOM when sufficient high powers are used (1-2 W). Here, 'after the AOM' refers to the propagation direction of the retro-reflected beam. If the signal of this beam is maximized one can assume to have a perfect overlap of the incoming and retro-reflected beam. To find this signal one can of course deliberately de-

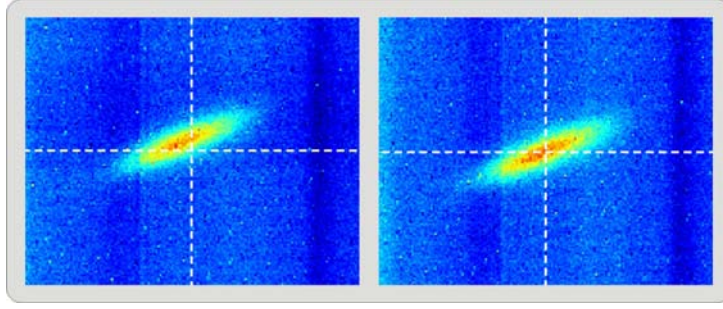


Figure 3.16: Alignment of incident beams. Two fluorescence pictures taken after a levitated TOF of 60 ms during the alignment process as described in the text.

adjust the Faraday isolator, but one needs to keep in mind that the settings of the optical diode should not be changed after step 2 of this alignment-process. This is especially true for Faraday isolators with Brewster polarizers designed for high laser power. They introduce a substantial beam pointing error when rotating the polarizer. The alignment is done similarly for the remaining vertical beam. So, if e.g. beam  $Z_{t-b}$  was aligned in step 1 and 2, we now overlap beam  $Z_{b-t}$  as good as possible with beam  $Z_{t-b}$ , and couple it into the fiber of beam  $Z_{t-b}$ . The same considerations as above are valid, except that it is much easier to find the weak beam transmitted through the isolator and the second fiber, since we can now place a photo-diode directly behind the fiber out-coupler.



# 4 BEC in an Optical Lattice Potential

The first part of this chapter briefly introduces the theory describing the physics of a BEC trapped in a 3D lattice potential. In particular the Bose-Hubbard model describing the quantum phase transition from the superfluid (SF) to the Mott insulator (MI) state is reviewed. The following section presents some of our measurements performed in order to test and characterize the lattice. The last section of this chapter reports on the observation of the SF to MI quantum phase transition, as the lattice depth, i.e. the ratio between kinetic energy and interaction energy, is varied. Additionally -and this is unprecedented- we present first indications of the ability to drive the phase transition via tuning of the scattering length, i.e. as only the interaction term in the Hamiltonian is varied.

## 4.1 Theoretical Introduction

### 4.1.1 Band structure, Bloch and Wannier functions

In order to describe the effect of a periodic potential on an atom cloud, we must first review the single-particle physics in such a system. As known from solid state physics, the movement of a single particle in a periodic potential implies the emergence of a band structure.

The dynamics of a single particle in a 1D periodic potential can be described by the Schrödinger equation

$$H\phi = E\phi, \quad \text{with} \quad H = \frac{\hat{p}^2}{2m} - V_{01D} \cos^2(kx) \quad (4.1)$$

being the Hamiltonian for an atom in an 1D lattice potential, and  $\hat{p} = -i\hbar\nabla$  being the momentum operator. According to the Bloch-Theorem (see e.g. [Kit04]), the solutions (*Bloch functions*) must have the form

$$\phi_q^n(x) = e^{iqx} u_q^n(x), \quad (4.2)$$

where  $u_q^n(x)$  are functions with the same periodicity  $a = \lambda/2 = \pi/k$  as the potential. It is found that the solutions can be completely characterized by their behavior in the first Brillouin zone ranging from  $q = -\hbar k$  to  $\hbar k$ . Remember that here  $k$  is the wavevector of the laser light field and represents the lattice constant.

The so-called quasimomentum  $q$  characterizes the phase difference of the particle's wavefunction between neighboring lattice sites.

Inserting this ansatz into Eq. 4.1 leads to a Schrödinger equation for  $u_q^n(x)$ :

$$H_q u_q^n(x) = E_q^n u_q^n(x), \quad \text{with} \quad H_q = \frac{(\hat{p} + q)^2}{2m} - V_{0_{1D}} \cos^2(kx). \quad (4.3)$$

In general  $u_q^n(x)$  are complicated functions. They can be found numerically after expanding  $u_q^n(x)$  and  $V_{0_{1D}} \cos^2(kx)$  as discrete Fourier sums (see Appendix B). The eigenvectors define the Bloch functions  $\phi_q^n(x)$ . They are, as one can see in Fig. (4.2), completely delocalised over the whole lattice. The eigenvalues  $E_q^n$  represent the eigenenergies for the  $n^{\text{th}}$  energy band. Figure 4.1 shows the *band structure* for different potential depths. Depending on the lattice depth  $V_{0_{1D}}$ , atoms in the lowest bands ( $E_n^q < V_{0_{1D}}$ ) are in bound states of the potential, whilst the higher bands ( $E_n^q > V_{0_{1D}}$ ) correspond to free particles. For deep lattices the potential on each lattice site can be approximated by a harmonic potential so that the level spacing  $\hbar\omega_{lat}$  corresponds to the energy separation of the two lowest bands  $E_{q=\pi/a}^1 - E_{q=\pi/a}^0$ .

The tunneling matrix element  $J$ , which describes the tunnel coupling between neighboring lattice sites, is directly related to the width of the lowest energy band through [Jak99]

$$J = \frac{\max(E_q^0) - \min(E_q^0)}{4}. \quad (4.4)$$

It is often convenient to express the Bloch functions in terms of *Wannier functions* [Wan37], which also form a complete set of orthogonal basis states and are wave functions that are maximally localized to individual lattice sites.<sup>1</sup> For 1D the Wannier functions are given by

$$w_n(x - x_i) = \sqrt{\frac{a}{2\pi}} \int_{-\pi/a}^{\pi/a} \phi_q^n(x) e^{-iqx_i} dq, \quad (4.5)$$

where  $x_i$  are the minima of the 1D lattice potential. The absolute-square of these wave functions can be interpreted as the probability distribution of a particle in the  $n^{\text{th}}$  energy band that is spatially localized to the  $i^{\text{th}}$  lattice site. The basis transformation can also be reversed to give

$$u_q^n(x) = \sqrt{\frac{a}{2\pi}} \sum_i w_n(x - x_i) e^{-iqx_i}. \quad (4.6)$$

---

<sup>1</sup>The Wannier functions are not uniquely defined by Eq. (4.5) because each Bloch wave function is arbitrary up to a complex phase. But for every band there exist only one Wannier function which has all three of the following properties (Kohn1959):

- It is real.
- It is either symmetric or antisymmetric about either  $x=0$  or  $x=a/2$ .
- It falls off exponentially.

Throughout rest of this work we will only refer to these Wannier functions, which are known as maximally localised Wannier functions.

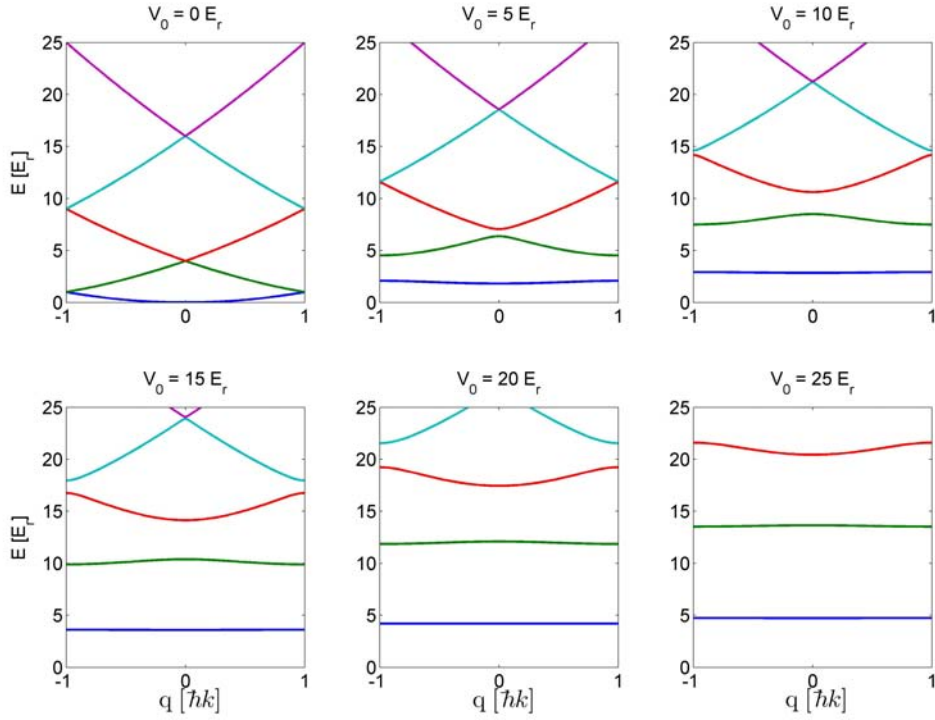


Figure 4.1: Band structure of an 1D optical lattice. Energy of the Bloch state versus quasimomentum, plotted for different lattice depths. For deep lattices the lowest band becomes flat and the width of the first band gap corresponds to the level spacing  $\hbar\omega$  on each lattice site.

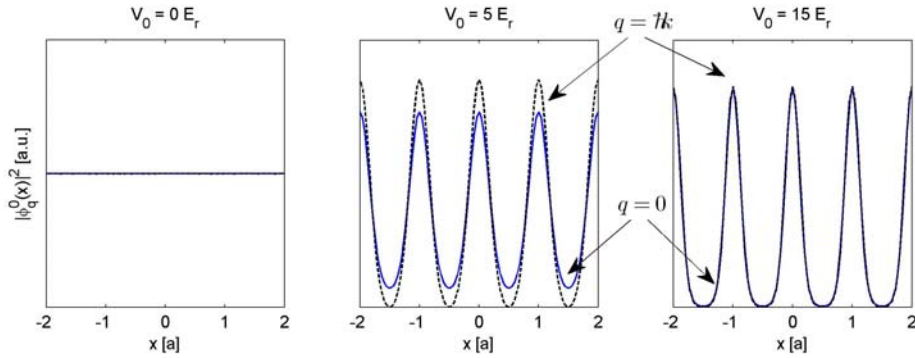


Figure 4.2: Probability density of the Bloch wave functions for  $q = 0$  and  $q = \hbar k$  in the lowest band  $n = 0$  for different lattice depths  $V_0$ . Bloch states are completely delocalized over the whole lattice.

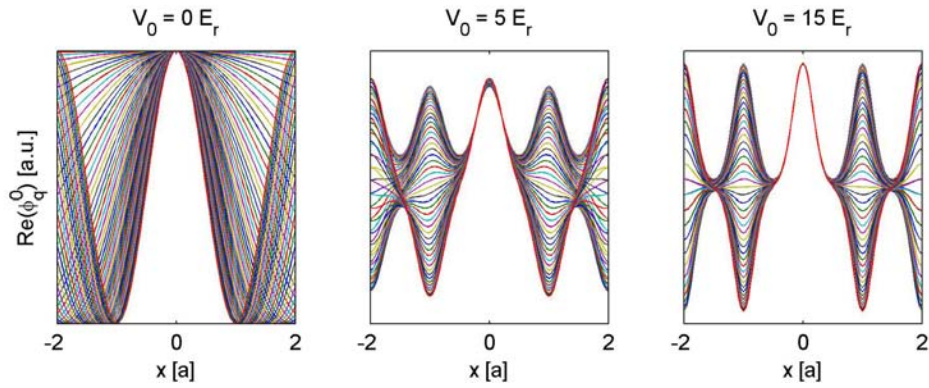


Figure 4.3: Real part of the Bloch functions in the lowest band for many different quasimomenta  $q$  and for three different lattice depths  $V_0$ . By summing the Bloch functions of all possible  $q$ 's one obtains a localized wavefunction at position  $x_i = 0$ .

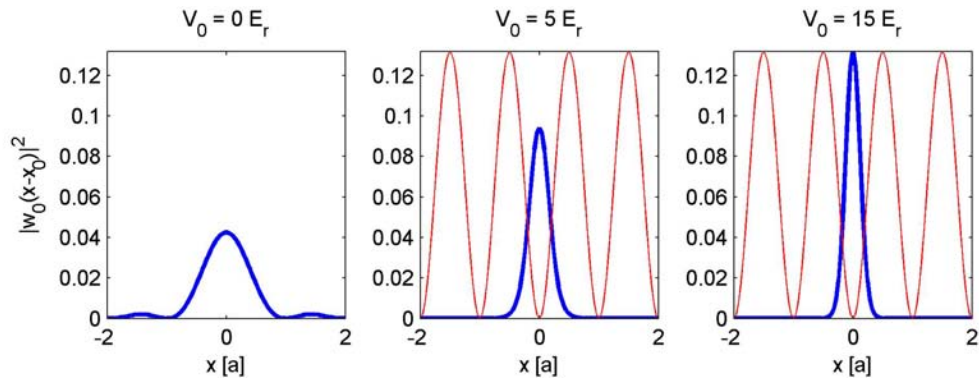


Figure 4.4: Probability density of a Wannier function for various lattice depths. Wannier functions constitute an orthogonal set of localized wavefunctions. The lattice potential is also illustrated.

For sufficiently deep lattices the Wannier functions for lower bound bands may be replaced by the harmonic oscillator wave functions. The major error in this approximation is that the Wannier functions fall off exponentially, whereas wave functions of the harmonic oscillator decay more rapidly in the tails ( $e^{-x^2/(2a_0)^2}$ ).

## 4.1.2 Bose-Hubbard Model

The simplest system for which one can investigate the Mott insulator phase transition at zero temperature are repulsively interacting bosons with spin zero in an optical lattice. Such a system is nicely described by the Bose-Hubbard model, an extension of the Hubbard model from solid state physics to bosonic particles. This was first realized by Jaksch et al. [Jak99]. The resulting physics of the corresponding Hamiltonian is governed by the competition between kinetic- and interaction energy of the strongly interacting bosons.

### Bose-Hubbard Hamiltonian

The Bose-Hubbard Hamiltonian is deduced from the many body Hamiltonian describing  $N$  interacting bosons confined by an external potential  $V_{ext}$

$$H = \int d^3x \hat{\psi}^\dagger(\mathbf{x}) \left( -\frac{\hbar^2}{2m} \nabla^2 + V(\mathbf{x}) \right) \hat{\psi}(\mathbf{x}) + \frac{1}{2} \frac{4\pi a_s \hbar^2}{m} \int d^3x \hat{\psi}^\dagger(\mathbf{x}) \hat{\psi}^\dagger(\mathbf{x}) \hat{\psi}(\mathbf{x}) \hat{\psi}(\mathbf{x}) \quad (4.7)$$

where  $\hat{\psi}^\dagger(\mathbf{x})$  is a boson field operator for atoms in a given internal atomic state.  $V(\mathbf{x})$  is the sum of the lattice potential (see Eq. 3.11) and a possible additional external confinement  $V_{ext}(\mathbf{x})$ . Since in our setup the waists of the lattice laser beams are much larger than the atom cloud and also much larger than the possible external confinement produced by the dimple-beam, we can approximate the lattice potential (Eq. 3.11) by  $V(\mathbf{x}) = V_{0_{1D,x}} \cos^2 kx + V_{0_{1D,y}} \cos^2 ky + V_{0_{1D,z}} \cos^2 kz$ .

The second term in the Hamiltonian represents the interactions between the atoms, with  $a_s$  being the s-wave scattering length and  $m$  the mass of the atom.

Because we are interested in the local atom-atom interactions, it is favorable to expand the field operator in the Wannier basis (see section 4.1.1). If one assumes the energies involved in the system dynamics to be small compared to excitations energies to the second band, only Wannier functions of the lowest band have to be considered, so that the field operator can be written as

$$\hat{\psi}(\mathbf{x}) = \sum_i b_i w_0(\mathbf{x} - \mathbf{x}_i), \quad (4.8)$$

and the Bose-Hubbard Hamiltonian reduces to

$$H = -J \sum_{\langle i,j \rangle} b_i^\dagger b_j + \sum_i (\epsilon_i - \mu) \hat{n}_i + \frac{1}{2} U \sum_i \hat{n}_i (\hat{n}_i - 1). \quad (4.9)$$

Here  $b_i$  and  $b_i^\dagger$  denote the annihilation and creation operator for the  $i^{th}$  lattice site, and the operator  $\hat{n}_i = b_i^\dagger b_i$  counts the number of atoms at lattice site  $i$ . The three terms can be interpreted as follows:

- The first term describes the hopping (tunneling) of atoms between adjacent lattice sites, with  $J$  being the tunnel matrix element for a particle to go from site  $i$  to one of its nearest neighbors  $j$ . Therefore  $\langle i, j \rangle$  denotes all pairs of nearest neighbors. Delocalization of the atoms minimizes this term since (in a very simplified picture) the ground state energy of the atoms decreases as the confinement volume increases.
- The second term accounts for the energy offset due to the external confinement  $\epsilon_i = \int d^3x V_{ext}(\mathbf{x}_i) |w(\mathbf{x} - \mathbf{x}_i)|^2 \approx V_{ext}(\mathbf{x}_i)$ . Please note that  $\mu$  was introduced to act as a Lagrangian multiplier when a grand canonical ensemble is considered. It ensures that  $\sum_i \langle n_i \rangle = N$  and represents the chemical potential. The difference  $(\mu - \epsilon_i)$  can therefore be viewed as the effective local chemical potential at the lattice site  $i$ .
- The repulsive interaction between particles in the same lattice site is described by the third term. Here  $U$  quantifies the cost in energy due to the repulsion of two adjacent atoms. The number of possible atom pairs in one lattice site is given by  $\frac{1}{2} \hat{n}_i (\hat{n}_i - 1)$ . Therefore this term is reduced if the atoms are localized to certain lattice sites.

For a given optical lattice potential the hopping matrix element  $J$  and the on-site repulsion parameter  $U$  can be evaluated numerically by calculating the band structure and its corresponding Wannier functions and evaluating the following expressions:

$$J = - \int d^3x w(\mathbf{x} - \mathbf{x}_i) \left( -\frac{\hbar^2}{2m} \nabla^2 + V(\mathbf{x}) \right) w(\mathbf{x} - \mathbf{x}_j) \quad (4.10)$$

$$U = \frac{4\pi a_s \hbar^2}{m} \int d^3x |w(\mathbf{x})|^4. \quad (4.11)$$

The dependence of  $J$  and  $U$  from the lattice depth  $V_0$  is further discussed in the next section and can be seen in Fig. 4.8. Note that the hopping term decreases exponentially whereas the interaction term increases slightly due to a tighter confinement of the interacting bosons. Therefore the ratio  $U/J$  is adjusted when varying the lattice depth, whereas, by scanning the scattering length  $a_s$  the on-site interaction  $U$  can be tuned separately.

Solving for the ground state of Bose-Hubbard Hamiltonian in mean field theory yields two different regimes: the *superfluid phase* with the number of atoms per lattice site fluctuating, and the *Mott-insulator phase*, where the particle number fluctuation at each site tends to zero.

## Superfluid Regime

For  $U/J$  small, i.e., for a small on-site interaction compared to energy associated with tunneling, the ground state is superfluid (SF). The tunneling term dominates

and it is energetically favorable to have atomic wavefunctions that are delocalized over the whole lattice. For  $N$  bosons and  $M$  lattice sites the many-body ground state can approximately be written as a product of *identical* single particle states [Jak99]

$$|\Psi_{SF}\rangle \propto \left( \sum_{i=1}^M a_i^\dagger |0\rangle \right)^N, \quad (4.12)$$

where  $|0\rangle$  denotes the vacuum state. Therefore the system can be described by a macroscopic wave function, with a constant phase across the lattice, giving rise to an interference pattern in our TOF images in form of discrete momentum peaks (see Fig. 4.5).

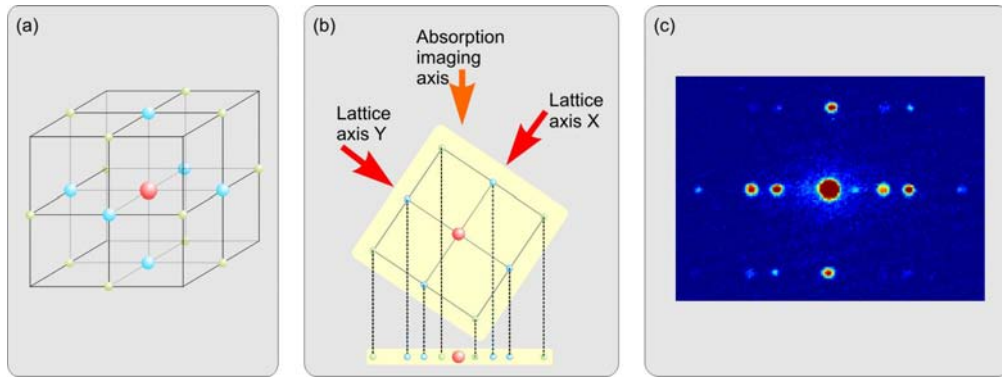


Figure 4.5: Momentum distribution of a BEC in a 3D optical lattice in the superfluid regime. (a) Schematic drawing showing the momentum peaks in 3D. (b) Because imaging axis and the horizontal lattice axes are at an off-45° angle, the momentum peaks corresponding to the X and Y axis appear side by side. (c) Actual absorption image after a TOF of 50 ms showing the momentum distribution of a Cs BEC in a  $4 E_r$  deep lattice.

Neglecting on-site interactions and assuming a homogeneous lattice (no external potential), the atoms are distributed with equal probability over all lattice sites, which results in a Poissonian atom number distribution with a mean of  $\bar{n} = N/M$  and a standard deviation of  $\sigma_i = \sqrt{\bar{n}}$ .

## Mott Insulator Regime

By increasing the repulsive interaction  $U$  compared to  $J$ , a quantum phase transition at zero temperature takes place. The system passes from the SF, as described above, to the Mott insulator (MI) phase, in which it becomes energetically costly for the particles to jump from one site to the next, since the interaction between two (or more) particles in one site increases the energy. Hence, the many-body ground state is -for a commensurate filling- a product of  $M$  *local* states with  $N/M$

atoms per lattice site. It is approximately given by [Jak99]

$$|\Psi_{MI}\rangle \propto \prod_{i=1}^M (a_i^\dagger |0\rangle)^{N/M}, \quad (4.13)$$

where  $N$  is the atom number and  $M$  the number of lattice sites. Commensurate filling means that  $N/M$  is an integer. If the filling is not commensurate the remaining particles will act as a SF. Thus, a MI state *in a homogeneous system* is only possible with commensurate filling. This not necessarily true for an inhomogeneous system, as argued in the following section.

In the Mott insulator phase each atom is localized to a single lattice site, and the atom number for each site is exactly determined and integer. Thus there is no coherent matter wave function spreading across the whole lattice anymore and the phase relations between the local wave functions become arbitrary. Therefore the interference pattern in the TOF images vanishes (see Fig 4.6).

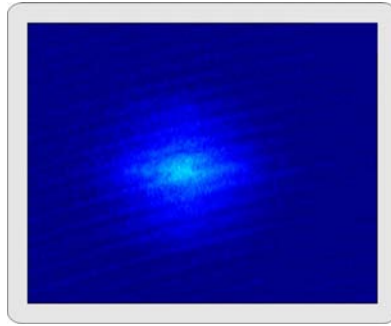


Figure 4.6: Absorption image after a 50 ms levitated TOF showing the momentum distribution of a BEC in a 3D optical lattice. With a lattice depth of  $16 E_r$  the system is clearly in the Mott insulator regime resulting in a loss of long range phase coherence. Therefore no interference peaks are visible.

### 4.1.3 Superfluid to Mott Insulator Transition

As mentioned in section 4.1.2 it is the competition between the interaction term  $\frac{1}{2}U \sum_i \hat{n}_i(\hat{n}_i - 1)$  and the hopping term  $-J \sum_{\langle i,j \rangle} b_i^\dagger b_j$  in the Hamiltonian that is responsible for the SF to MI transition. If we try to minimize the expectation value of the Hamiltonian  $\langle \psi | H_{BH} | \psi \rangle \rightarrow \min$  to obtain the most probable state of our system  $|\psi\rangle$ , the interaction parameter  $U$  tends to localize the atoms to the lattice sites, whereas the hopping parameter  $J$  tends to delocalize the atoms over the whole lattice. So, depending on the ratio  $U/J$  the system at  $T = 0$  energetically favors either the SF ground state (with atoms being delocalized over the whole lattice) or the MI ground state (with a fixed atom number in each lattice site). The critical point  $(U/J)_c$  where the system will undergo this quantum phase

transition is evaluated using mean field calculations [Kam93, Fis89, Ami98], and is given for a homogeneous system with one particle per site by the condition

$$\left(\frac{U}{J}\right)_c = (3 + 2\sqrt{2})z \approx 5.8 \cdot z, \quad (4.14)$$

where  $z$  is the number of nearest neighbors lattice sites. For large occupations  $\bar{n} \gg 1$  the critical value is

$$\left(\frac{U}{J}\right)_c = 4\bar{n} \cdot z, \quad (4.15)$$

with  $\bar{n}$  being the mean atom number per lattice site.

These estimates agree well with more rigorous calculations [Els99]. The resulting phase diagram for a two-dimensional square lattice is depicted in Fig. 4.7. It shows the boundary between Mott insulating and superfluid phase as a function of the chemical potential  $\mu$  and the hopping matrix element  $J$ , both in units of the onsite interaction  $U$ .

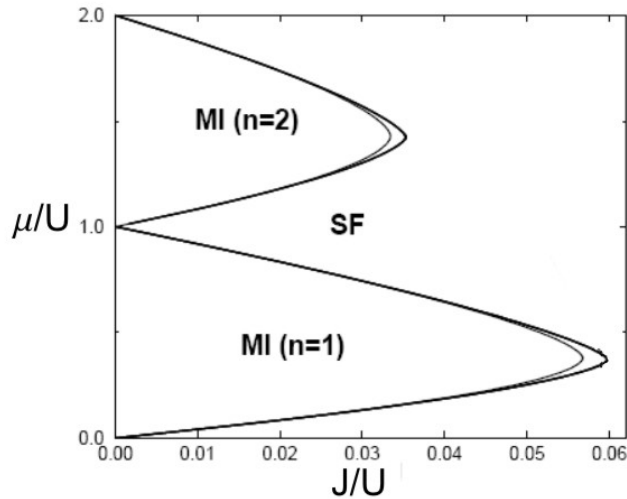


Figure 4.7: Phase diagram showing the boundary between Mott insulating (MI) and superfluid (SF) phase for a two-dimensional square lattice with  $z = 4$  next neighbors. The figure is taken from Ref. [Els99].

At a given  $U/J$  the difference in  $\mu$  between the top and bottom phase-boundary corresponds to the energy gap  $\Delta E$  in the excitation spectrum resulting from a particle-hole excitation. Therefore the tip of the lobe in the phase diagram (Fig. 4.7) corresponds to the critical transition point  $(U/J)_c$ . At this point the energy difference of particle and hole excitations (from a Mott insulator state) vanishes.

In fact, the excitation spectrum can be used to experimentally probe the onset of the MI regime. In the SF phase the system can be excited by any arbitrarily small excitation, but as it enters the insulating phase, an energy gap  $\Delta E$  opens up and one can only excite a particle-hole creation with perturbations corresponding

to  $\Delta E = \hbar\omega_e$ , e.g., by modulating the lattice depth at a frequency  $f_e = \Delta E/h$ . For  $U \gg J$ , i.e. when deep in the MI phase, the energy gap equals the onsite energy  $U$  (see sec. 4.3.3).

### Driving the Transition

The phase transition from the SF to the MI phase can be induced via the following two experimentally accessible parameters:

- The lattice depth:

A variation in the potential depth of the lattice inevitably changes the potential barrier height between lattice sites and therefore the corresponding tunneling/hopping rate of the atoms, but at the same time an increase of the lattice depth pushes the atoms closer together, which results in a higher onsite interaction energy. This energy  $U$  varies almost linearly as shown in Fig. 4.8 (a), whereas the hopping term  $J$  decreases exponentially as depicted in Fig. 4.8 (b) as the lattice is ramped up. Therefore the ratio  $U/J$  can be varied over many orders of magnitude by changing the lattice depth. Figure 4.8 (c) shows  $U/6J$  plotted versus the lattice depth for different scattering lengths  $a$ . The expected value of  $\sim 5.8$  for the phase transition in a three-dimensional lattice is also shown.

- The scattering length:

Because of the existence of suitable Feshbach resonances, one can control the s-wave scattering length  $a$  via the applied magnetic field strength over a wide range. A change in the scattering length directly influences the interaction properties of the atoms, and one can therefore vary the onsite interaction energy  $U$  without affecting any of the other parameters involved. Figure 4.8 (d) shows the required lattice depth as a function of the scattering length for the expected phase transition to take place (given by  $U/6J \sim 5.8$ ).

### Transition in an Inhomogeneous System

So far we have only discussed the transition in a homogeneous system as illustrated in Fig. 4.9 (a). The experimental realizations of a Mott insulator implies (so far) the use of an harmonic external potential as shown in Fig. 4.9 (b). In order to describe the inhomogeneous situation one can use the standard approximation that a slowly varying external potential may be accounted for by an effective local chemical potential  $\mu_{loc} = \mu - \varepsilon_i$  (see Eq. 4.9). Assuming e.g. that the chemical potential at the trap center  $\mu$  falls into the  $n = 2$  Mott-lobe, one obtains two Mott insulating domains separated by a superfluid shell when moving to the boundary of the trap where  $\mu_{loc}$  vanishes. In this manner, all the different phases that exist for a given  $J/U$  are present simultaneously. From Fig. 4.9 (c) it becomes obvious that the critical value of  $J/U$  depends on the distance from the trap center and that

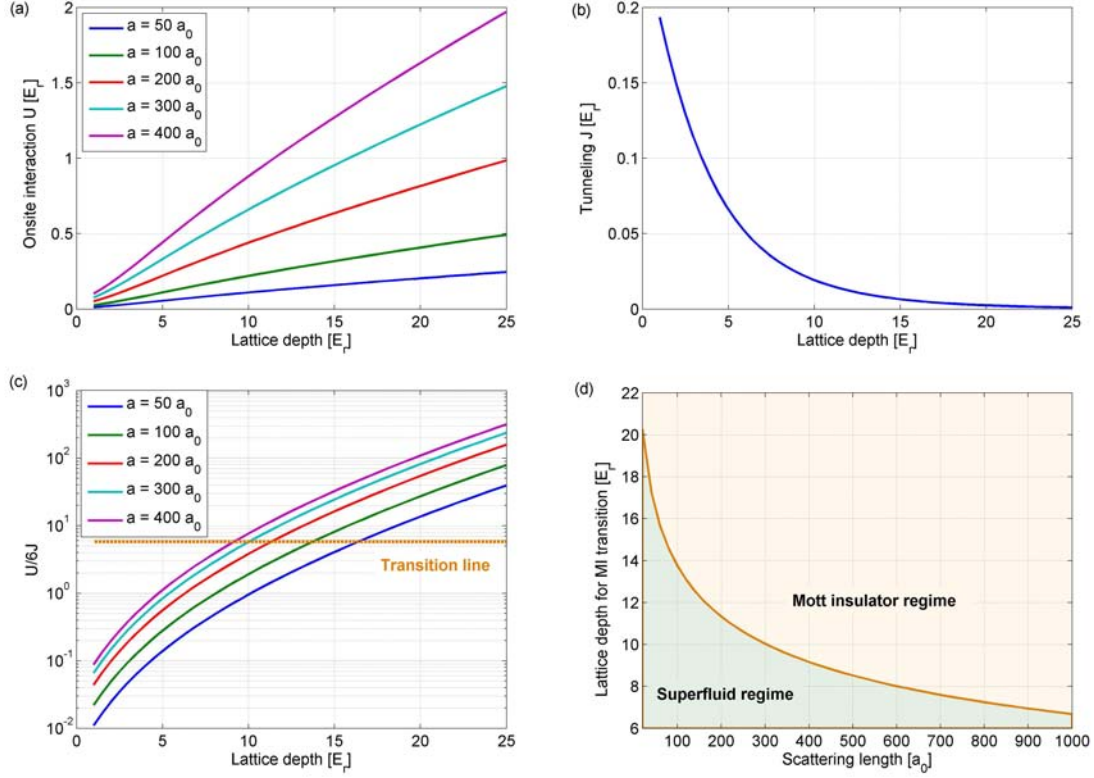


Figure 4.8: Various plots showing the mutual dependence of the key parameters in the superfluid to Mott insulator phase transition. (a) The onsite interaction energy  $U$ , (b) the tunnel matrix element  $J$ , (c) and the critical ratio  $U/6J$  plotted versus the lattice depth. For a simple cubic lattice we have six nearest neighbors lattice sites, and thus  $z = 6$ . Figure (d) shows the critical lattice depth for the onset of the phase transition as a function of the scattering length.

the transition in an inhomogeneous system is therefore continuous. Nevertheless, a rather sharp transition can be observed by ramping the lattice depth over the critical value, because the ratio  $J/U$  depends exponentially on  $V_0$ . In contrast,  $J/U$  depends only linearly on the scattering length  $a_s$ . Hence we expect a rather smooth transition when raising the scattering length beyond the critical value. In any case, signatures of the SF to MI transition should become apparent for a slightly higher value  $U/J$  than predicted for the homogeneous case given in Eq. 4.14. At  $U/J = 5.8 \cdot z$  only a thin outer shell of the atomic cloud is in the Mott insulating regime.

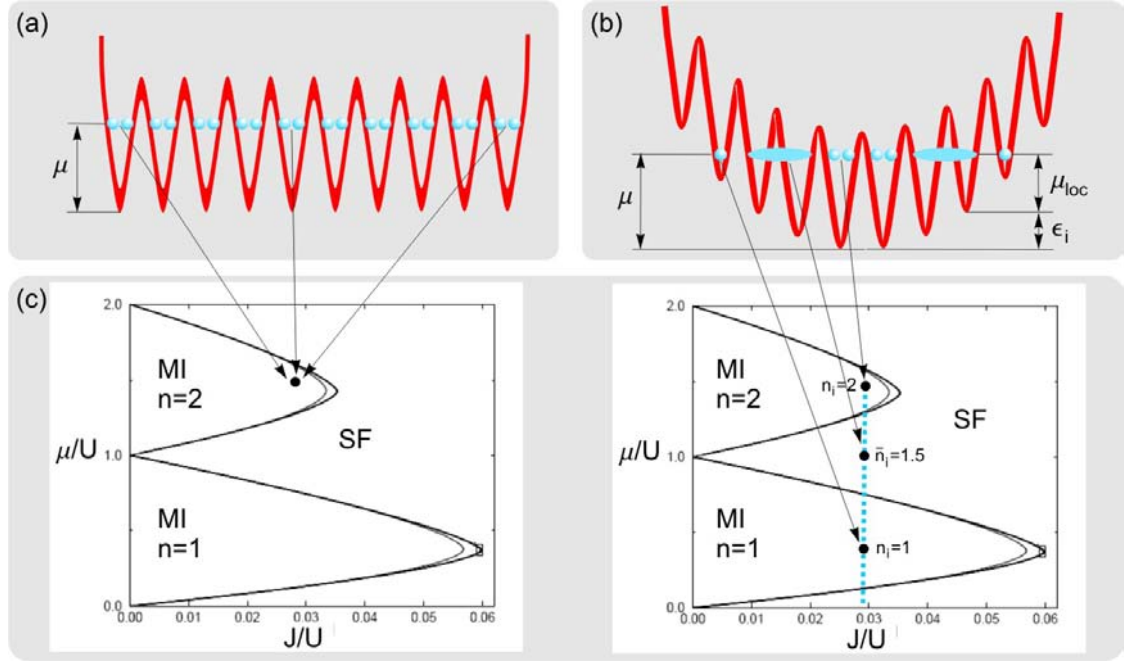


Figure 4.9: Schematic picture illustrating a lattice with homogenous potential depth (a), and a system with inhomogenous potential depth (b). Each point in the inhomogeneous system can approximately be viewed as a homogeneous system with  $\mu = \mu_{loc}$  (c).

#### 4.1.4 Loading of a BEC into the Lattice Potential

##### Adiabaticity Criteria

Most lattice experiments require the atomic ensemble to be in -or very close to- its many body ground state. Therefore an *adiabatic* transfer of the BEC into the lattice becomes substantial. If the lattice is ramped up slow enough, the wave function of the condensate remains in the many body ground state of the system. It is important to note the existence of two time scales of adiabaticity, i.e. one with respect to interband transitions and the other with respect to intraband excitations.

- **Interband:** Adiabaticity with respect to the (single) particle band structure. If the lattice potential is ramped up too fast, higher energy bands can get populated (see sec. 4.2.2). The corresponding time scale is determined by the level spacing, therefore this adiabaticity criterion can be written as [Den02]

$$|\langle n, q | \partial H / \partial t | 0, q \rangle| \ll (E_n^q - E_0^q)^2 / \hbar. \quad (4.16)$$

The left-hand side is always less than  $dV_0/dt$  and for the case of  $q \sim 0$  (stationary BEC) the energy difference between ground state and the first excitable state is at least  $4 E_r$  (e.g. see band structure for  $V_0 = 0$ ). Therefore the condition 4.16 (for  $q \sim 0$ ) is easily fulfilled by choosing a ramp-up speed

$$dV_0/dt \ll 16 E_r^2 / \hbar \sim 1.3 \cdot 10^5 E_r / s, \quad (4.17)$$

meaning, that the first  $E_r$  should be ramped up in a time much longer than  $\sim 7 \mu s$ . Since the level spacing  $E_n^q - E_0^q$  increases for larger lattice depths ( $V_0 > 1 E_r$ ), one can continuously raise the ramp-up speed and still maintain adiabaticity. See e.g. Ref. [Jul05] for the ideal ramp-up function. Note that for a BEC that is moving relative to the lattice potential, it becomes harder to fulfill this adiabaticity criterion, since  $E_n^q - E_0^q \rightarrow 0$  as  $q$  approaches the Brillouin zone boundary.

- **Intraband:** Adiabaticity with respect to many body dynamics within the lowest Bloch band.

Depending on the lattice depth and on the external confinement, the many body ground state has a certain density profile (see below). If parameters are changed, the atoms have to redistribute over the lattice in order to maintain a constant chemical potential. This leads to an adiabaticity criterion with time scales that are considerably longer than discussed above. Theoretical studies of the loading dynamics have been reported in Ref. [Skl02b, Skl02a, Ise05]. An experimental study has been performed in Ref. [Ger07] in which they found a time scale of  $\sim 100 ms$  for adiabatically loading the BEC into the lattice. It is in accordance with the criterion  $|\dot{H}| \ll \Delta E^2 / \hbar$ , where  $\Delta E$  is the energy difference between ground state and possible excitation. If we reduce the question of adiabaticity to whether the atoms can redistribute through tunneling in order to adapt the size of the system to the instantaneous Thomas-Fermi shape, we can take  $\Delta E$  to be of the order of the hopping matrix element  $J$ . For the relevant time scales one can also assume  $|\dot{H}| \sim |\dot{J}|$ , so that we obtain the following adiabaticity criterion [Ger07]:

$$\frac{\hbar |\dot{J}|}{J^2} \ll 1. \quad (4.18)$$

## Density Re-distribution

Using the Thomas-Fermi approximation ( $E_{kin} \sim 0$ ) and the Gross-Pitaevskii equation we obtain the usual relations for a BEC in a harmonic potential [Pit03]:

$$n(\mathbf{r}) = \begin{cases} \frac{\mu - V(\mathbf{r})}{g} & \text{for } \mu - V(\mathbf{r}) > 0, \\ 0 & \text{otherwise,} \end{cases} \quad (4.19)$$

$$\mu = \frac{\hbar\bar{\omega}}{2} \left( \frac{15Na_s}{a_{ho}} \right)^{\frac{2}{5}}, \quad (4.20)$$

$$\hat{n} = \frac{\mu}{g} \quad \text{with} \quad g = \frac{4\pi\hbar^2 a_s}{m}. \quad (4.21)$$

Here  $n(\mathbf{r})$  stands for the atom density,  $\mu$  for the chemical potential,  $V(\mathbf{r})$  for the confining potential,  $\bar{\omega} = \sqrt[3]{\omega_x\omega_y\omega_z}$  for the corresponding geometrically averaged trap frequency,  $a_{ho} = \sqrt{\frac{\hbar}{m\bar{\omega}}}$  the characteristic trap size,  $N$  the total atom number,  $a_s$  the scattering length,  $m$  the atom mass, and  $\hat{n}$  the peak density at the trap center  $V(\mathbf{r} = 0) = 0$ . With these expressions one can calculate the density distribution  $n(\mathbf{r}) = \hat{n}(1 - r^2/R_{TF}^2)$  with the Thomas-Fermi radius  $R_{TF} = 1/\bar{\omega}\sqrt{2\mu/m}$  (defined as the radius at which the density vanishes) for a BEC trapped in a harmonic potential.

If we adiabatically apply a lattice potential we obviously expect these parameters to change: By increasing the lattice depth the atoms are pushed tighter together, thereby increasing the interaction energy  $U$ . In an inhomogeneous external confinement like a harmonic trap, this increase in energy results in an broadening of the density distribution of the atomic ensemble (see Fig. 4.10). In analogy to the argumentation used for calculating the above expressions, we can estimate the extension and density of the atom cloud in an optical lattice as follows [Gre03]:

By applying the Thomas-Fermi approximation to the Bose-Hubbard Hamiltonian the expectation value of the energy for a single lattice site is given by

$$E_i \simeq V_{ext_i}\bar{n}_i + \frac{U}{2}\bar{n}_i \cdot (\bar{n}_i - 1). \quad (4.22)$$

Therefore the chemical potential can be calculated as

$$\mu = \frac{\partial E_i}{\partial \bar{n}_i} = V_{ext_i} + U\bar{n}_i - \frac{U}{2} = const., \quad (4.23)$$

where the index  $i$  refers to the position of the  $i$ -th lattice site. Note that because the constant term  $U/2$  does not alter the solution, but rather complicates the algebra, we will omit it in the subsequent calculations.

Since the extension of the cloud is much smaller than the external potential we can approximate  $V_{ext_i}$  by a harmonic potential  $1/2m\bar{\omega}^2 r^2$ , so that we can write the average atom number per lattice site (at lattice site  $i$ ) as

$$\bar{n}_i = \hat{n}_l \left( 1 - \frac{i^2}{i_{TF}^2} \right), \quad (4.24)$$

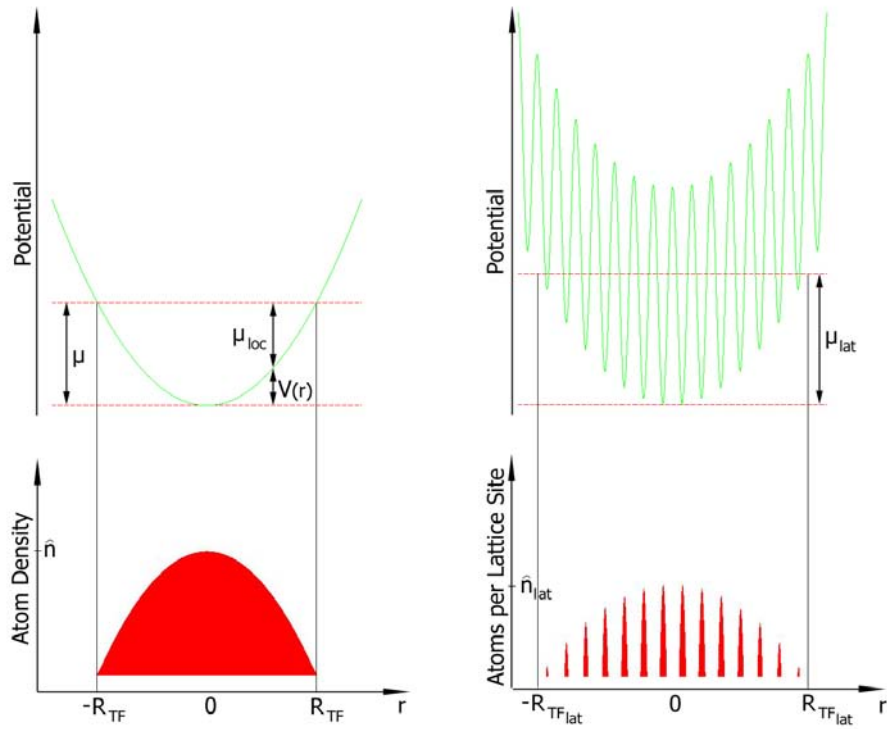


Figure 4.10: Change in density and Thomas-Fermi radius when loading a BEC into a lattice. Because the onsite interaction augments, the chemical potential and therefore the extension of the cloud increases.

with  $\hat{n}_l = \mu/U$  being the peak density in the lattice potential. Note that the density here refers to atoms per lattice site and therefore has different units than its counterpart  $\hat{n}$ , which is in atoms per volume. The spatial coordinate is now expressed by the lattice site  $i = r/(\lambda/2)$ , so that  $i_{TF} = R_{TF} \cdot (2/\lambda) = 1/\bar{\omega} \sqrt{2\mu/m} \cdot (2/\lambda)$  gives the lattice site at which the atom number vanishes.

The chemical potential  $\mu$  can now be calculated by normalizing the atom number per site  $n_i$  to the total atom number  $N$ :

$$N = \sum_i \bar{n}_i \simeq \int \bar{n}_i d^3i = \int_0^{i_{TF}} \frac{\mu}{U} \left(1 - \frac{i^2}{i_{TF}^2}\right) 4\pi i^2 di. \quad (4.25)$$

Since the lattice spacing is much smaller than the extension of the cloud, we can ignore the discreteness of the lattice, and we obtain

$$\mu = \left( \frac{15NU(\lambda/2)^3 m^{3/2} \bar{\omega}^3}{16\sqrt{2}\pi} \right)^{\frac{2}{5}}. \quad (4.26)$$

Note that this result is equivalent to the one obtained above (Eq. 4.20), except that the interaction term is now represented through  $U$  rather than  $g$ . The factor  $(\lambda/2)^3$  accounts for the different units of  $g$  and  $U$ . Figure 4.11 shows the corresponding atom number per lattice site  $\hat{n}_l = \mu/U$  at the center of the external potential as a function of the total atom number and the external trap frequency for different onsite interaction energies  $U$ .

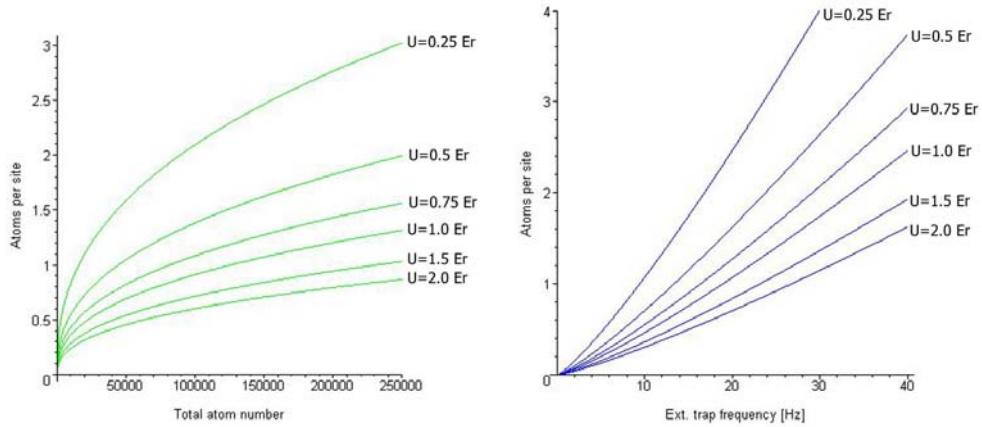


Figure 4.11: Plots showing the peak atom density in atoms per lattice site as a function of the total atom number and the external trap frequency for different onsite interaction energies.

## 4.2 Testing and Characterizing the Lattice

The following section reports on the experiments that were undertaken to test and characterize, the optical lattice.

### 4.2.1 Bloch Oscillations

To get a little sense of achievement after a long period of setting up and fighting the usual obstacles, we performed the simple experiment of observing Bloch oscillations of Cs atoms in an one-dimensional optical lattice.

The early quantum theory of electrons in crystal lattices by Bloch led to the striking prediction that a homogeneous static electric field induces an oscillatory rather than uniform motion of the electrons [Blo29, Zen34]. These so-called Bloch oscillations had been unobserved in solid state crystals for many years, because the resulting time period ( $\sim ps$ ) is much larger than scattering time of the electrons by the lattice defects.

By using ultracold Cs atoms in optical lattices one can nicely make use of the following advantages: the initial momentum distribution can be tailored at will, the periodic potential can be turned on and off and is such that the resulting Bloch period is in the millisecond range, there are no lattice defects, the decoherence can be adjusted via the scattering length. Already in the mid 90's Salomon et al. [BD96] reported the observation of Bloch oscillations of Cs atoms at sub-recoil temperatures.

#### What are Bloch oscillations?

Bloch oscillations are a quantum effect, which arises when a particle is placed in a one-dimensional periodic potential with periodicity  $a$  under the influence of a static force  $F$ . The dynamics are generated by the Hamiltonian

$$H = \frac{p^2}{2m} + V(x) + Fx, \quad \text{with} \quad V(x+a) = V(x). \quad (4.27)$$

The resulting dynamics are quite counter-intuitive in a sense that, instead of an accelerated motion toward infinity, one observes a coherent oscillation with period

$$\tau_B = \frac{h}{|F|a}, \quad (4.28)$$

corresponding to the time required for the quasimomentum  $q$  to scan a full Brillouin zone, and with an amplitude

$$l_B = \frac{\Delta}{2|F|}, \quad (4.29)$$

where  $\Delta$  is the width of the corresponding energy band. A simplistic explanation can be given by assuming an invariance under a translation in space by one lattice period *and* an energy shift  $\delta E = Fa$ , which leads to a phase shift  $\delta Et/\hbar$ . At a time

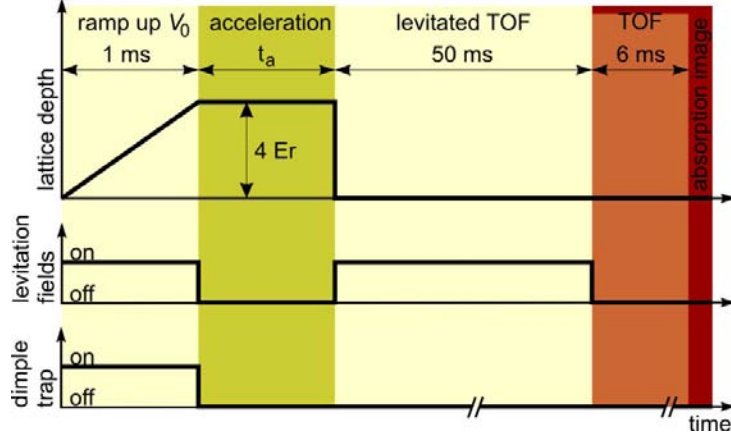


Figure 4.12: Schematic plot showing the ramping procedure for lattice depth, levitation fields, and external optical potential for the observation of Bloch oscillations.

$\tau_B$  this phase shift will equal  $2\pi$ . The available space interval for the oscillatory motion is limited by the fact that the gained kinetic energy  $Fx$  can not be larger than the width of the Bloch-band (see Fig. 4.1).

For a more detailed theoretical discussion of this peculiar phenomenon and its possible applications, please refer to Ref. [TH04, Sco04, Kol04, Car05].

## Experimental Observations

For this measurement we create a BEC with about  $10^5$  Cs atoms. The vertical one-dimensional optical lattice is then ramped up in 1 ms to a lattice depth of  $4 E_r$  and all the trapping and levitation potentials are turned off (see Fig. 4.12). At this point the macroscopic matter wave starts evolving according to Eq. 4.27 with gravity acting as the force  $F = mg$ . After a certain lattice hold time (acceleration time)  $t_a$  the lattice is switched off and the levitation potential is turned back on for a levitated time of flight (TOF) of 50 ms. Subsequently an absorption image is taken to reveal the resulting momentum distribution of the atom cloud. For technical reasons a regular TOF of 6 ms is performed prior to taking the image. Throughout the rest of this work this short TOF will not explicitly be mentioned, it can be viewed as part of the absorption imaging process.

Fig. 4.13 shows the absorption images taken for various lattice hold times. One can nicely see how the momentum distribution scans the first Brillouin zone.

In the near future we certainly plan to investigate this phenomenon more thoroughly, including the measurement of the interaction-induced decoherence of the Bloch oscillations [Buc03, Wit05].

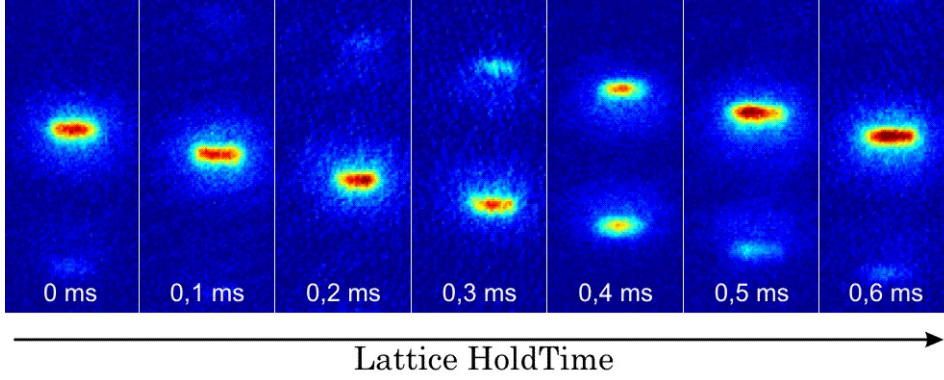


Figure 4.13: Bloch Oscillations: Absorption images taken after a levitated TOF of  $50\text{ ms}$  revealing the momentum distribution for different lattice hold times.

## 4.2.2 Measuring the Lattice Depth

Obviously it is quite crucial to have an exact knowledge of the actual lattice depth for any lattice experiment. Since the effective lattice depth depends on the actual light power within the glass cell (which one can not measure directly), the actual beam waist, and the spatial overlap of the counter-propagating laser beams, it is necessary to verify the depth of our optical lattice potential experimentally, i.e., to have a method for calibration.

For this purpose we use a simple procedure described in [Den02] where we quickly turn on the lattice potential (each axis at a time) once the BEC is produced. After leaving the atom-cloud evolve for a certain lattice hold time  $t_h$  we shut off the lattice abruptly and measure the resulting momentum distribution as a function of  $t_h$ .

### Theoretical background

The eigenstates (Bloch states)  $|n, q\rangle$  of the atom-lattice system can be expanded in a discrete plane-wave basis with momenta  $p = q + 2l\hbar k$  and vice versa:

$$|n, q\rangle = \sum_{l=-\infty}^{\infty} a_{n,q}(l) |\phi_{q+2l\hbar k}\rangle \quad (4.30)$$

$$|\phi_{q+2l\hbar k}\rangle = \sum_{n=0}^{\infty} a_{n,q}^*(l) |n, q\rangle \quad (4.31)$$

Figure 4.14 and 4.15 show the decompositions for  $q = 0$  and a lattice depth of  $25 E_r$ .

A BEC with a momentum spread  $\ll \hbar k$  can be approximated by a plane wave  $|\Psi(t = 0)\rangle = |\phi_{p \sim 0}\rangle$ . When suddenly loaded into a lattice, we can re-write its

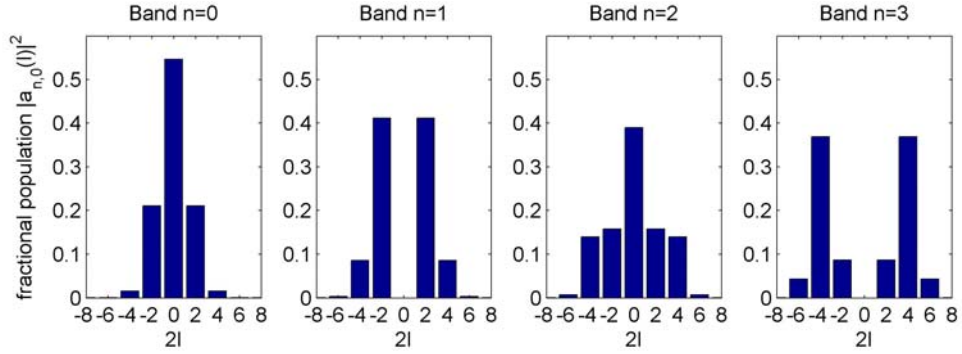


Figure 4.14: The lattice eigenstates can be expressed as a superposition of plane waves with fractional population  $|a_{n,q}(l)|^2$ . Shown is the plane-wave decomposition of the lattice eigenstates  $|n, q = 0\rangle$  for the four lowest bands for  $q = 0$  and a lattice depth of  $25 E_r$ .

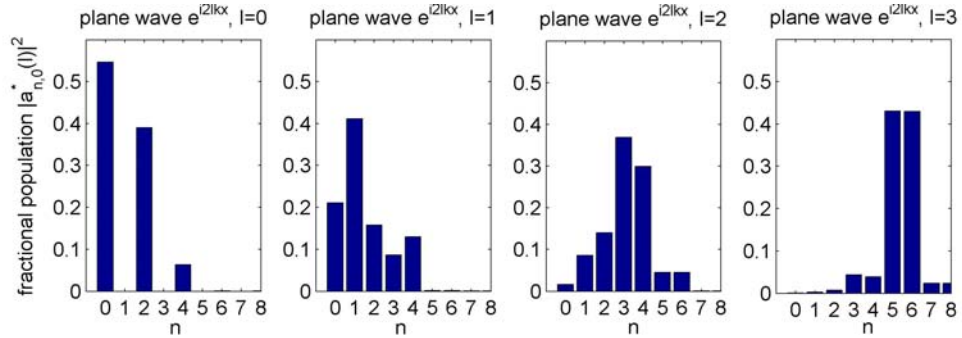


Figure 4.15: The plane waves  $|\phi_{p=q+2l\hbar k}\rangle$  can be expressed as a superposition of Bloch states  $|n, q\rangle$  with fractional population  $|a_{n,q}^*(l)|^2$ . Here, the decompositions of plane waves  $|\phi_{p=2l\hbar k}\rangle$  with  $q = 0$  for  $l$  from 0 to 3 and a lattice depth of  $25 E_r$  are shown.

wavefunction for convenience in the Bloch state basis  $|n, q\rangle$

$$|\Psi(t=0)\rangle = \sum_{n=0}^{\infty} |n, q\rangle \langle n, q | \phi_p \rangle = \sum_{n=0}^{\infty} a_{n,q}^*(0) |n, q\rangle. \quad (4.32)$$

The BEC wavefunction, while held in the lattice, evolves in time according to

$$|\Psi(t)\rangle = \sum_{n=0}^{\infty} a_{n,q}^*(0) e^{-i\frac{E_n(q)t}{\hbar}} |n, q\rangle. \quad (4.33)$$

After a time  $t_h$  we abruptly switch off the periodic potential, projecting the result back onto the plane-wave basis, we obtain the coefficients  $b_q(l)$  of each of the plane-wave components

$$b_q(l) = \sum_{n=0}^{\infty} a_{n,q}^*(0) a_{n,q}(l) e^{-i\frac{E_n(q)t_h}{\hbar}}, \quad (4.34)$$

which correspond to the populations of the discrete momentum peaks of our TOF measurements. The resulting interferences of the differently evolving phases  $e^{-iE_n/\hbar t}$  produce oscillations in the populations of these discrete momentum components as a function of  $t_h$ , e.g. for the case where only band 0 and 2 are significantly populated:

$$|b_q(l)|^2 \propto 1 + \cos\left(\frac{E_2 - E_0}{\hbar} t_h\right). \quad (4.35)$$

Band 1 and all odd bands are not populated because the symmetry of those eigenstates (antisymmetric) does not match the symmetry of the initial BEC wavefunction.

Therefore the oscillation frequency  $f_{0-2} = h/(E_2(q=0) - E_0(q=0))$  is a direct measure of the energy gap between band 0 and 2, which in turn depends on the lattice depth (see section 4.1.1).

## The measurement

The following procedure is performed with only a one dimensional lattice, each axis at a time. After producing a BEC with  $10^5 - 2 \cdot 10^5$  atoms, we switch the lattice on as fast as possible. For this purpose we turn off the active intensity stabilization (PI control, see section 3.2.2). Its use would limit us to ramp-up times of around  $50 \mu\text{s}$ . To avoid shot-to-shot fluctuations of the light intensity an initialization procedure at the beginning of each sequence is performed. In this short procedure the lattice and its intensity stabilization is turned on for a time  $> 50 \mu\text{s}$ , then the direct digital synthesis device (DDS) and thereafter the stabilization is turned off. Using this initialization procedure prior to a short unstabilized operation is almost equivalent to a stabilized operation, since the main intensity fluctuations are due to a drift of the polarization axis (see section 3.2.3), which are on the order of  $30 \text{ s}$  whereas the time between initialization and actual use of the lattice is on the order of  $5 \text{ s}$  (the time it takes to produce a BEC).

Without active stabilization the ramp-up time is only restricted by the DDS (bus-tact frequency) and therefore the ramp-up time should be of the order of  $5 \mu s$  (a measurement of the actual ramp-up time is currently limited by the much slower photo-diodes). After a lattice hold time  $t_h$  the potential is turned off by switching off the DDS. To reveal the momentum distribution, an absorption image is taken after a levitated TOF of  $50 ms$ . During the entire sequence the atoms are levitated using the appropriate magnetic fields.

Fig. 4.16 and Fig. 4.17 show the time evolution of a cesium BEC in a 1D lattice potential for the X-axis and Z-axis respectively. Because of the moderate lattice depth only band 0 and 2 are significantly populated, which results in a sinusoidal variation with frequency  $f_{0-2}$  of the population of the momentum components  $0, \pm 2 \hbar k$ . See Fig. 4.18 for the relation between frequency  $f_{0-2}$  and lattice depth  $V_{01D}$ .

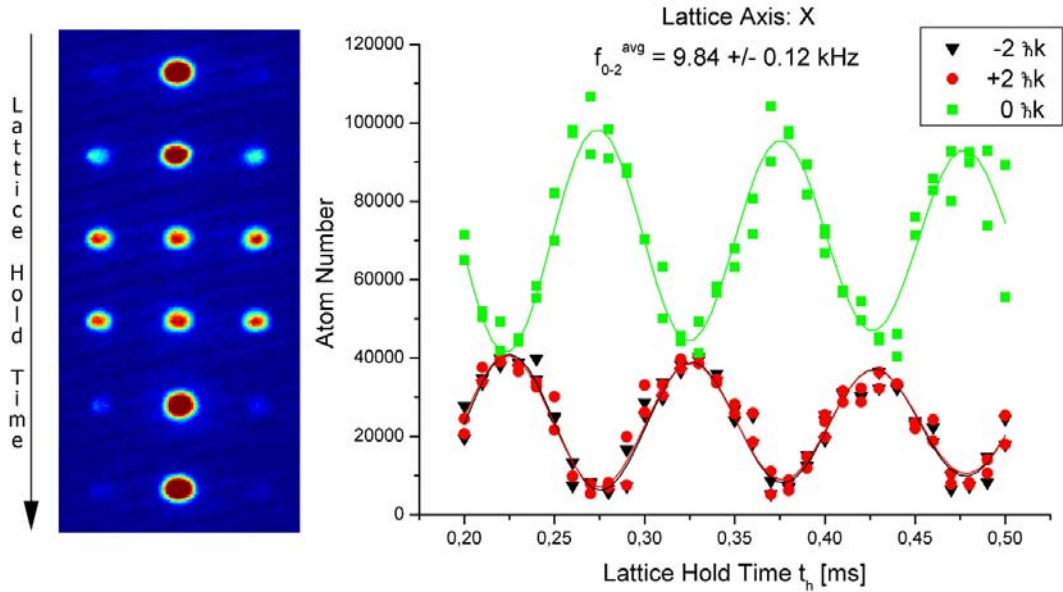


Figure 4.16: Time evolution of a BEC in an abruptly ramped 1D lattice (X-axis) with a laser power of  $440 mW$  (measured before the glass cell). The figure on the left shows a sequence of absorption images. The plot on the right shows the populations of the momentum components  $(0\hbar k, \pm 2\hbar k)$  taken for different lattice hold times  $t_h$ . Damped sinusoidal functions are fitted on the data points (solid lines) and the resulting average oscillation frequency is given in the plot.

Table 4.1 shows the results of our calibration measurements for all three lattice axes. Note that this calibration has to be redone once in a while but especially after any re-alignment of the lattice beams.

Note that the high reflection loss of the lattice beam in X-direction is due to the unfavorable orientation of the polarization with respect to the glass cell. Given the

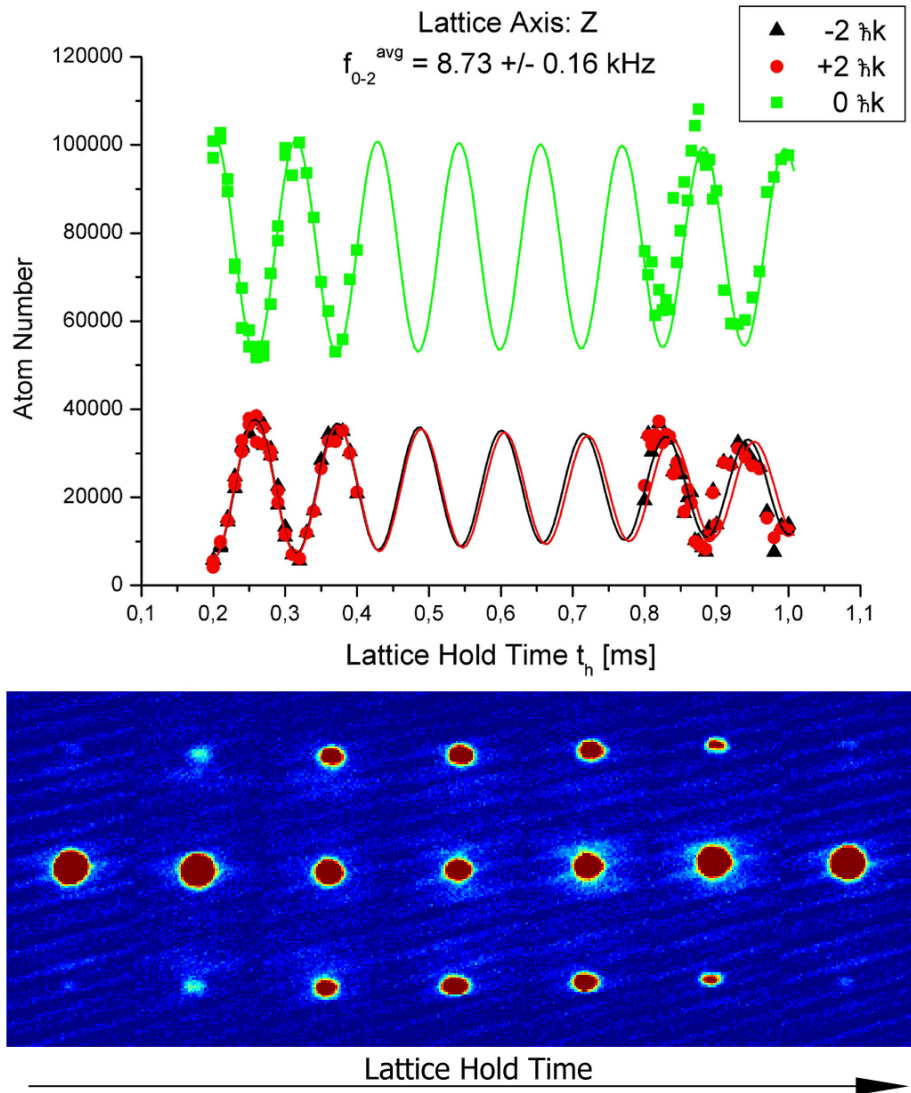


Figure 4.17: Time evolution of a BEC in an abruptly ramped 1D lattice (Z-axis) with a laser power of 250 mW per beam. The figure at the bottom shows a sequence of absorption images. The plot at the top shows the populations of the momentum components ( $0\hbar k, \pm 2\hbar k$ ) taken for different lattice hold times  $t_h$ . Damped sine-functions are fitted on the data points between 0.2 ms and 0.4 ms (solid lines). To test the fit and the coherence of the oscillations some points were taken with higher lattice hold times. The resulting oscillation frequency  $f_{0-2}^{avg}$  (averaged over the three fit-results) is also given in the plot.

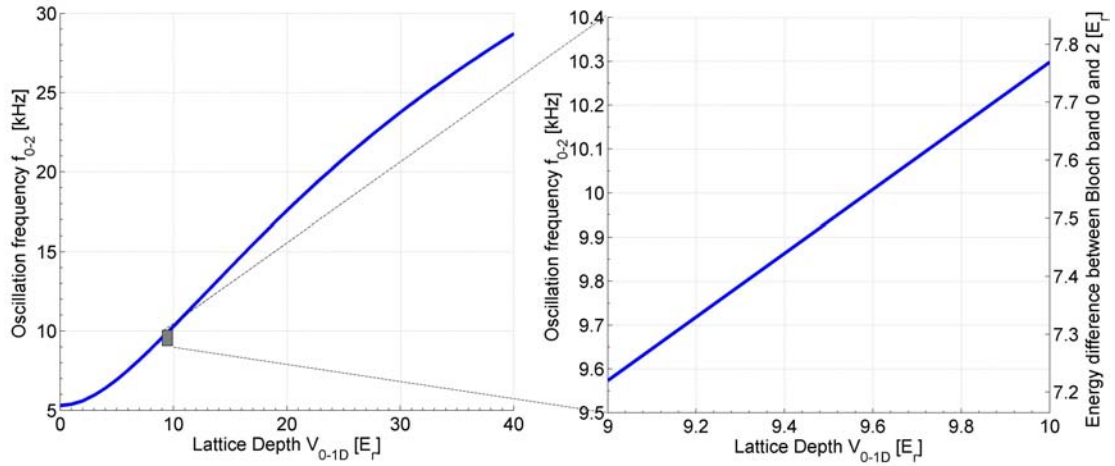


Figure 4.18: Two plots at different scales showing the energy gap between Bloch band 0 and 2 and the corresponding frequency  $f_{0-2}$  as a function of the lattice depth  $V_{0,1D}$ . Both plots are calculated numerically with the Hamiltonian truncated for  $|| > 5$  (see Appendix B).

abundant laser power, it was chosen this way to ensure that it does not interfere with the lattice beam in Y-direction. Since the X- and the Y-beam are mutually detuned to each other by 5 MHz, one could reduce the losses of the beam in X-direction by rotating its polarization by  $90^\circ$  without affecting the form or stability of the lattice potential.

### 4.2.3 Lattice-induced Heating

When working with a Bose-Einstein condensate, it is obviously very important to avoid heating of the atomic ensemble. Heating can be caused by technical limitations of the experimental setup e.g., intensity or spatial fluctuations of the laser beam used to trap the atoms. For conventional optical dipole traps [Geh98] it is fairly easy to keep these fluctuations below the critical limit. But for optical lattice potential the technical stability requirements are more stringent, since phase fluctuations of the light field can also cause heating as illustrated in Fig. 4.19. These phase fluctuations can be caused by the laser source, the rf-driver of the AOM, or even by mechanical vibrations of the opto-mechanical components, i.e. mirror mounts, etc.

Therefore it is necessary to test the effect of the optical lattice on the BEC in terms of heating. Such a test is in principle straightforward and can be performed in many different ways. Here we measure the remaining BEC fraction after the lattice is switched on for a certain amount of time. Obviously one should take care to meet the adiabaticity criteria for ramping the lattice up and down.

Axis	$P_{beam}^{(1)}$	Reflections	Expected $V_{0,1D}$	Measured $V_{0,1D}$	$P_{beam}/E_r$
X	440 mW	38% <sup>(2)</sup>	11.2 $E_r$	$9.37 \pm 0.17 E_r$	47.0 mW/ $E_r$
Y	360 mW	3% <sup>(3)</sup>	14.4 $E_r$	$8.67 \pm 0.31 E_r$	41.5 mW/ $E_r$
Z	250 mW <sup>(5)</sup>	8% <sup>(4)</sup>	9.5 $E_r$	$7.8 \pm 0.2 E_r$	32.1 mW/ $E_r$

<sup>(1)</sup> Laser beam power measured before glass cell, <sup>(2)</sup> calc. for s-polarized @ 40°  
<sup>(3)</sup> calc. for p-polarized @ 50°, <sup>(4)</sup> calc. for 0° incident beam angle, <sup>(5)</sup> per beam

Table 4.1: Summary of the lattice depth measurements. For comparison the expected lattice depth, including the loss due to reflections on the glass cell, is also given. Any discrepancy between expected and measured values are most likely due to misalignment of the incoming and reflected/counter-propagating laser beams and/or the actual beam waist differing from the supposed 500  $\mu\text{m}$ .

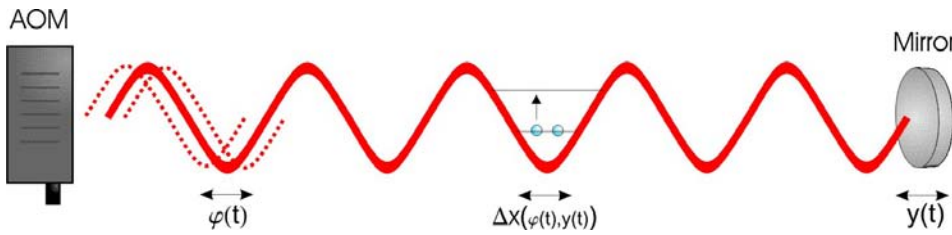


Figure 4.19: Phase fluctuations in the laser light field can cause heating of the atoms trapped in the standing wave. Phase fluctuations can originate from the laser source, the rf-driver of the AOM, or from mechanical instabilities of the opto-mechanical setup. Phase fluctuations translate into a spatial movement of the lattice wells. If this movement has a periodicity of the trap frequency of the lattice well, it will contribute to the heating of the atomic ensemble.

## Experimental Sequence

The starting point is a BEC with about  $1.5 \cdot 10^5$  atoms. The lattice is ramped up exponentially at a constant rate, according to  $V_0(t) = 10E_r \cdot e^{t/100ms}$ . This way, the first part of the ramp is the same for different final lattice depths, and the different measurements can be compared even if adiabaticity is not completely fulfilled. Then the lattice is held a certain depth  $V_0$  for a variable time  $t_h$ , before it is linearly ramped down to zero in 120 ms. See Fig. 4.20. Now, a TOF absorption image with an expansion time of 50 ms is taken. The BEC fraction of the atom cloud is extracted from the image by applying a bimodal fit [Sel04] as shown in Fig. 4.21. The bimodal fit accounts for the fact that the BEC is at the center of the cloud, and that its density distribution is given by the Thomas-Fermi parabola. The atoms that are not in the absolute ground state surround the BEC. This thermal fraction is fitted by a Gaussian distribution.

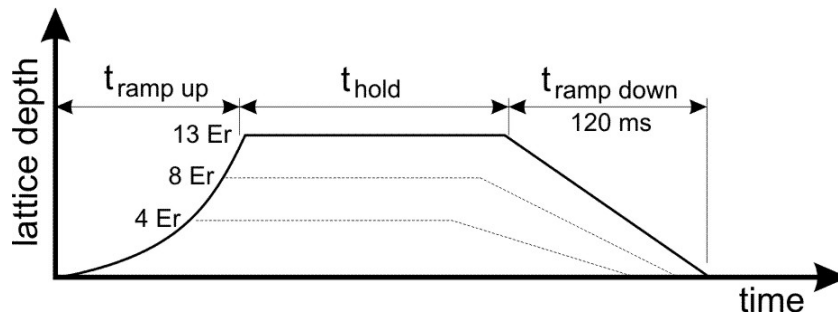


Figure 4.20: Ramping of the lattice depth for the measurement of lattice-induced heating. The ramp up is performed exponentially with a constant rate to ensure the same adiabaticity condition for different final lattice depths during the critical first part of the ramp.

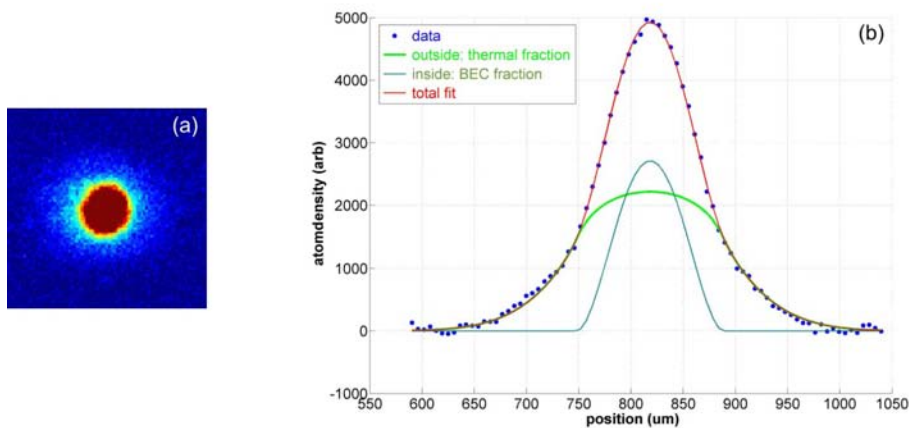


Figure 4.21: Determining the BEC fraction: (a) Absorption image taken after a TOF of 50 ms. (b) Bimodal fit: The BEC fraction is determined by the area under the TF-parabola divided by the area of the total fit.

## Observations - 3D Lattice

Figure 4.22 shows the BEC fraction plotted versus the lattice hold time  $t_h$  for different lattice depths  $V_0$ . For comparison one measurement was made with zero lattice depth. The BEC fraction grows in the first 2 s by almost 20%, indicating an incomplete evaporation during the BEC production sequence. For a shallow lattice ( $4 E_r$ ) some heating effect can already be observed. For a lattice depth of  $13 E_r$  the BEC fraction is substantially reduced on the timescale of 500 ms, a timescale that is about an order of magnitude larger than the longest lattice hold time performed in any of the experiments presented within this work. Nevertheless, for future experiments longer lattice hold times may be required. Therefore the exact causes of the heating and possible improvements have to be investigated.

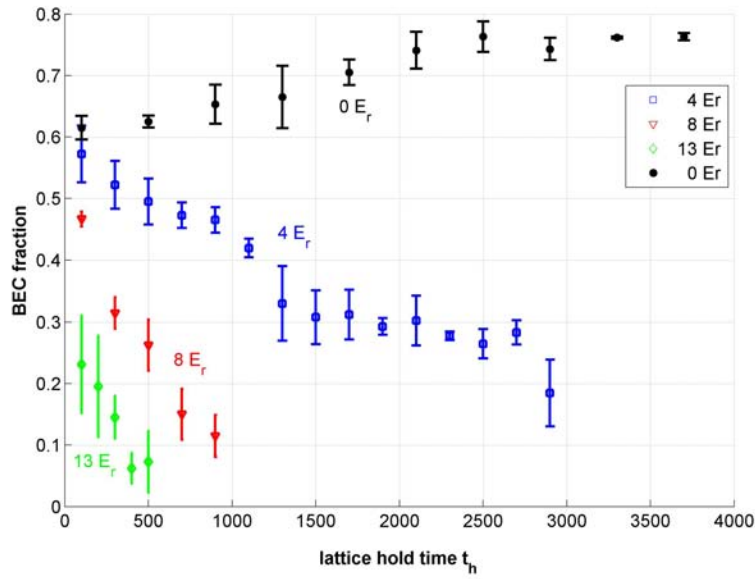


Figure 4.22: Plot showing the remaining BEC fraction after holding the atoms in the 3D lattice for a time  $t_h$  for various lattice depths.

In summary we conclude that the lattice-induced heating of the 3D lattice is at the order of  $\frac{0.5\%}{100 \text{ ms } 1 E_r}$  for now.

## Observations - 1D Lattice

As a second step, the heating caused by each individual lattice axis was examined. In Figure 4.24 (a) the remaining BEC fraction is plotted against the lattice hold time for a depth of  $8 E_r$ . At first sight it seems as only the lattice along the X-axis is responsible for the heating observed in the 3D lattice, as the BEC fraction remains more or less constant for the Y, and Z-axis. But, by also plotting the remaining total atom number versus the lattice hold time, see Fig. 4.24 (b), one can observe a stronger atom loss while holding the atoms in the Z-axis. At this point

we attribute this behavior to the following circumstances: The external confining potential, generated by the two dimple beams, allows for continuous evaporation only along one direction (see Fig. 4.23), the X-axis. So, if a given lattice beam does disturb the atomic ensemble in its ground state, it will either cause a reduction of the BEC fraction or a reduction of the total atom number, depending on its relative orientation to the dimple potential. The 1D lattice in X-direction inhibits the continuous evaporation along its direction, resulting in the reduction of the BEC fraction. On the other hand the 1D lattice generated by the beams along the Z-axis does not inhibit the continuous evaporation, because the atoms with sufficient energy to overcome the dimple potential, can escape along the X-axis. Hence, the BEC fraction remains almost constant, while the total atom number continuously decreases. When loading the BEC into the 1D lattice along the Y-axis, we observe neither a decrease in the BEC fraction nor to a substantial loss in atom numbers.

At this point we do not fully understand as to why the 1D lattices along the Y-axis hardly influences the BEC, whereas the beams along the other two directions do have an observable effect on the atomic ensemble.

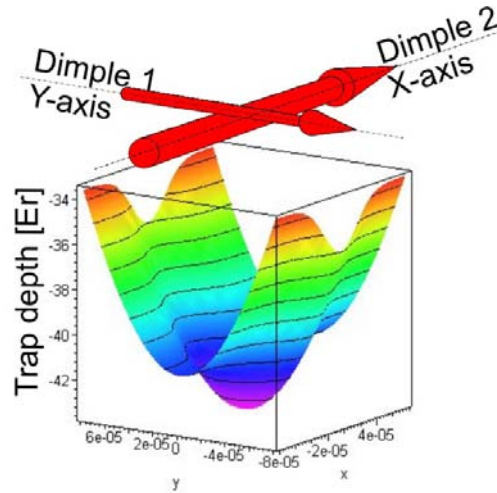


Figure 4.23: Schematic plot showing the shape of the external potential created by the two dimple beams.

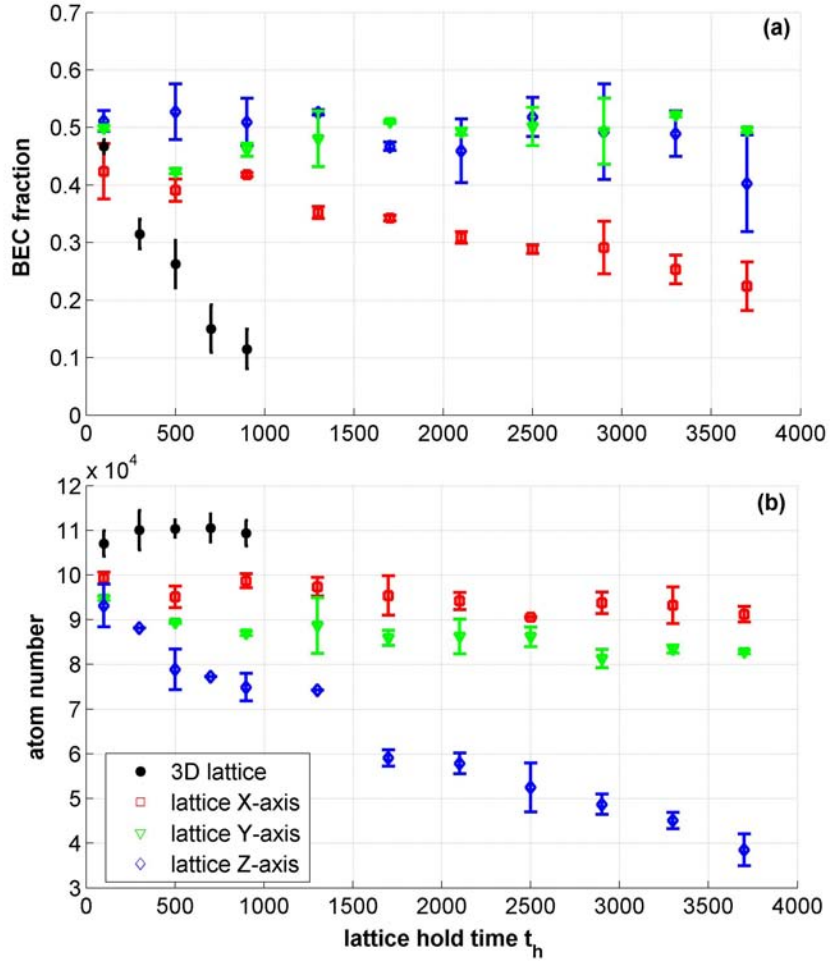


Figure 4.24: Effects of each individual 1D lattice on the atomic ensemble. The BEC fraction (a) and the total atom number (b) after holding the atoms in a 1D lattices is plotted as a function of the lattice hold time for each individual lattice direction. For comparison the effect of the 3D lattice is also shown. The measurement was performed with a lattice depth of  $8 E_r$ .

## 4.3 Experimental Observations of the Mott Insulator Transition

### 4.3.1 Driving the Transition via the Lattice Depth

#### Experimental Sequence

The experiments are performed with a condensate of about  $1.5 \cdot 10^5$  Cs atoms in the ( $F = 3, m_F = 3$ ) state. After evaporation process is completed (see sec. 2.3.2), the atoms are trapped by the two crossed dimple beams, where one has a waist of  $\sim 40 \mu\text{m}$  with a power of 1.5 mW and the other has a waist of  $\sim 250 \mu\text{m}$  with a power of 1000 mW. They generate an approximate harmonic trap with the following trap frequencies:  $\nu_x = 20$  Hz,  $\nu_y = 18$  Hz, and  $\nu_z = 27$  Hz. During evaporation and throughout the rest of this experimental sequence, the gravitational potential is compensated by an appropriate magnetic field gradient.

After the condensate has been prepared, the 3D lattice potential, as described in sec. 3.2, is superimposed. The lattice depth is exponentially ramped up in 60 ms to  $V_{0,max} = 16 E_r$ . At this depth and with a scattering length of  $210 a_0$  the peak atom number per lattice site (corresponding to the SF phase)  $\hat{n}_l = \mu/U$  calculates to approximately 1.3 (see sec. 4.1.4). We therefore expect the trap center to be in the  $n = 2$  Mott-lobe. The atoms are held for a time  $t_h = 10$  ms before the lattice is linearly ramped down again. Figure 4.25 (a) illustrates the ramping of the lattice depth. As the depth is ramped up, parts of the atom cloud (inhomogeneous system) will undergo a transition from the superfluid to the Mott insulator state. In this state, the tunneling of the atoms is greatly suppressed, and the long range coherence of the condensate is lost. If the lattice is ramped below the transition point again, the system restores the phase coherence.

#### Long Range Phase Coherence

The long range phase coherence of the condensate in the optical lattice can be directly tested by observing the multiple matter wave interference pattern. It is formed after ballistic expansion when all trapping potentials are switched off abruptly. The levitation is kept on, to keep the cloud from falling out of the camera's viewing range. After an expansion time of 35 ms an absorption image is taken. If the condensate is superfluid, the resulting TOF image shows the characteristic momentum peaks at  $\pm 2\hbar k$ . If the system is in the Mott insulator regime, the interference peaks in the TOF image vanish [Zwe03, Gre02a].

#### Observations

To observe the phase transition from the superfluid to the Mott insulator state, we take levitated TOF-images at various stages of the sequence. TOF-images in the ramp-up phase are taken with a sequence as shown in Fig. 4.26 (a). For images during the ramp-down phase a ramping sequence as illustrated in Fig. 4.26 (b) is

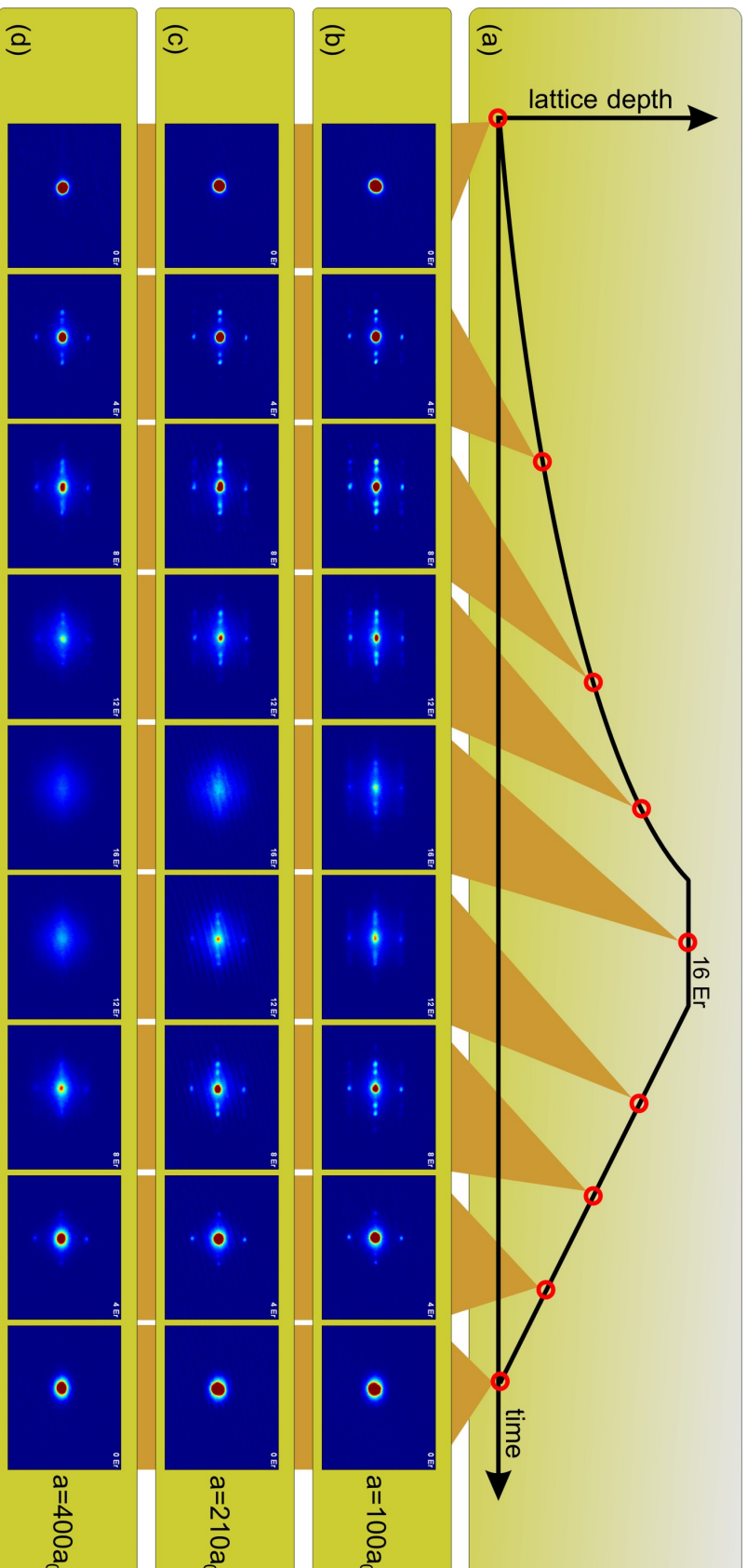


Figure 4.25: Superfluid to Mott insulator transition: (a) Schematic drawing of the ramping procedure of the lattice depth. (b), (c), and (d) TOF-images taken at different stages of the sequence for various scattering lengths. Narrow interference peaks show the long range phase coherence and therefore the superfluidity of the condensate, whereas the absence of interference maxima indicates the transition to the Mott insulator phase.

used. Figure 4.25 (c) shows a series of TOF-images taken with a scattering length of  $210 a_0$ . For a lattice depth up to about  $8 E_r$  nearly perfect phase coherence can be observed, characterized by narrow interference maxima. As the lattice potential is raised, the higher order interference maxima initially increase, because of a tighter localization of the atomic wave functions at a single lattice site. At a potential depth of  $12 E_r$  the interference peaks have not further increased in strength. Instead, an incoherent background shows up and gains more and more strength as the lattice depth is raised higher. At a depth of  $16 E_r$  the higher order momentum peaks have basically vanished, indicating the full loss of long range phase coherence. Figure 4.25 (d) shows a similar series of TOF-images taken with a scattering length of  $400 a_0$ . Due to the higher onsite interactions, the phase transition already takes place at a lower lattice depth. In the sequence with the scattering length set to  $100 a_0$ , shown in Figure 4.25(b), long range phase is still present even for  $16 E_r$ , indicating that the system is not deep in the Mott insulator regime.

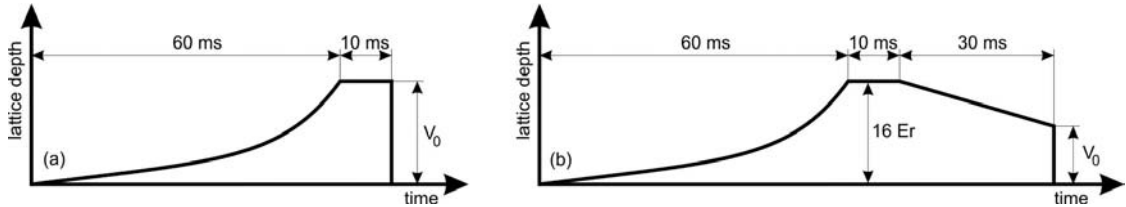


Figure 4.26: Ramping procedure for the lattice depth. (a) For a TOF image taken in the ramp-up phase. (b) For a TOF image taken in the ramp-down phase.

### Comparison with the expected transition point

The exact determination of the transition point for an inhomogeneous system is a non-trivial issue [Zwe03, Kas02]. As already discussed in sec. 4.1.3, we expect any signature related to a superfluid to Mott insulator transition to appear for  $U/6J \sim 5.8$ . Figure 4.27 shows the values of the lattice depth and scattering length of this measurement in the phase diagram. For the measurements with  $210 a_0$  and  $400 a_0$ , corresponding to Fig. 4.25 (c) and (d),  $16 E_r$  were clearly sufficient to enter the Mott insulator regime. This is in good agreement with the total disappearance of the interference peaks in the TOF-images. According to this diagram, even the measurement performed with  $100 a_0$  should have, at least partially, entered the Mott insulating phase. As we are not capable to spatially resolve the different phases within the atomic cloud, the question remains to whether or to what extend the system has performed the phase transition.

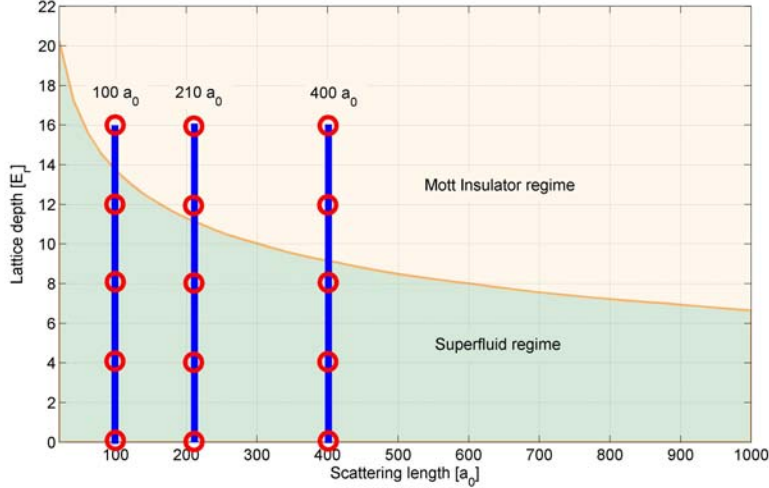


Figure 4.27: Relevant parameters for the SF to MI transition corresponding to the TOF-images shown in Fig. 4.25. The transition line in this plot is for a homogeneous system with  $\bar{n} = 1$ , i.e.  $U/6J = 5.8$ , therefore only indicating the onset of the continuous phase transition.

### 4.3.2 Driving the Transition via the Scattering Length

#### Experimental Sequence

The starting point for this experiment is the same as described in the previous section: A condensate of about  $1.5 \cdot 10^5$  Cs atoms which is optically trapped by the two dimple beams.

With the scattering length set to  $170 a_0$ , the lattice potential is adiabatically ramped up to  $9 E_r$  in 200 ms. At this point the ratio  $U/J$  and therefore the system is deep in the superfluid regime. In contrast to all previous experimental realizations of a Mott insulator, we now intend to drive the phase transition by varying only the interaction term  $U$  via the scattering length  $a_s$ . In our setup,  $a_s$  can be directly changed via Feshbach tuning as described in sec. 2.2.2. Therefore the current in the magnetic coils is raised from 8.2 A to 10.5 A. This corresponds to ramping the scattering length from  $170 a_0$  to  $420 a_0$ . At this stage the system should be in the Mott insulator regime, resulting in a loss of the long range phase coherence. It can be restored by ramping down the scattering length again. The momentum distribution is imaged via a levitated TOF sequence with an expansion time of 40 ms and a scattering length of  $30 a_0$ . Setting the scattering length to low values during the expansion yields more pronounced interference maximas. The ramping procedures are illustrated in Fig 4.28.

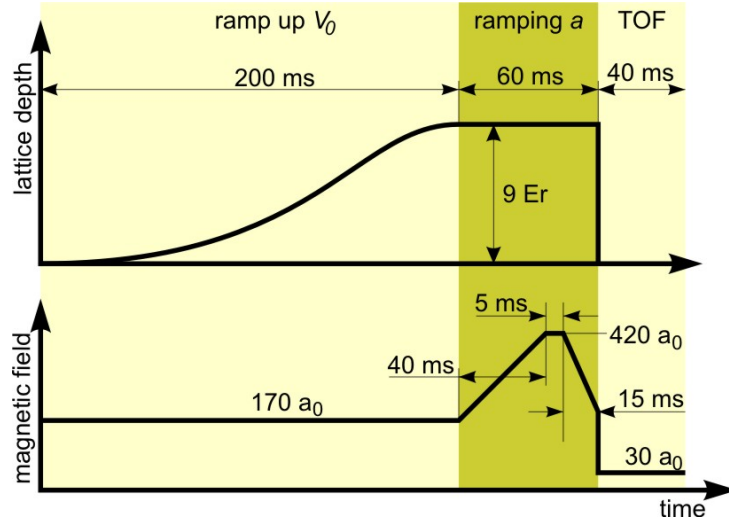


Figure 4.28: Ramping procedure for lattice depth and scattering length for driving the system from the superfluid to the Mott insulator regime and back via the scattering length.

## Observations

Figure 4.29 shows TOF images at various stages of this sequence. At a scattering length of  $190 a_0$  excellent phase coherence can be observed, as even the next higher order interference peaks are visible. As the scattering length is increased, the strength of the momentum peaks decreases and the incoherent background gains considerably in strength and size. The increase in interaction strength makes a delocalization of the atoms over several lattice sites energetically unfavorable. Therefore the long range phase coherence and its related interference pattern disappears. At a scattering length of  $420 a_0$  the momentum peaks have almost completely vanished and the TOF image is dominated by a diffuse momentum distribution. At this point the ratio  $U/6J$  is approximately 6. To drive the system deeper into the Mott insulator regime a higher scattering length would be required. Due to technical reasons, this was yet not possible without decoherence effects, but its realization is currently worked on.

## Comparison with the expected transition point/Required improvements

Figure 4.30 visualizes the parameters corresponding to the TOF-images in Fig. 4.29 (b) within the phase diagram. With a scattering length of  $420 a_0$  and a lattice depth of  $9 E_r$  we barely crossed the transition line. Thus it is even more surprising that a clear decrease in long range phase coherence is already present. As mentioned in sec. 4.1.3, one expects only a thin shell of the atomic cloud to have entered the Mott insulating regime.

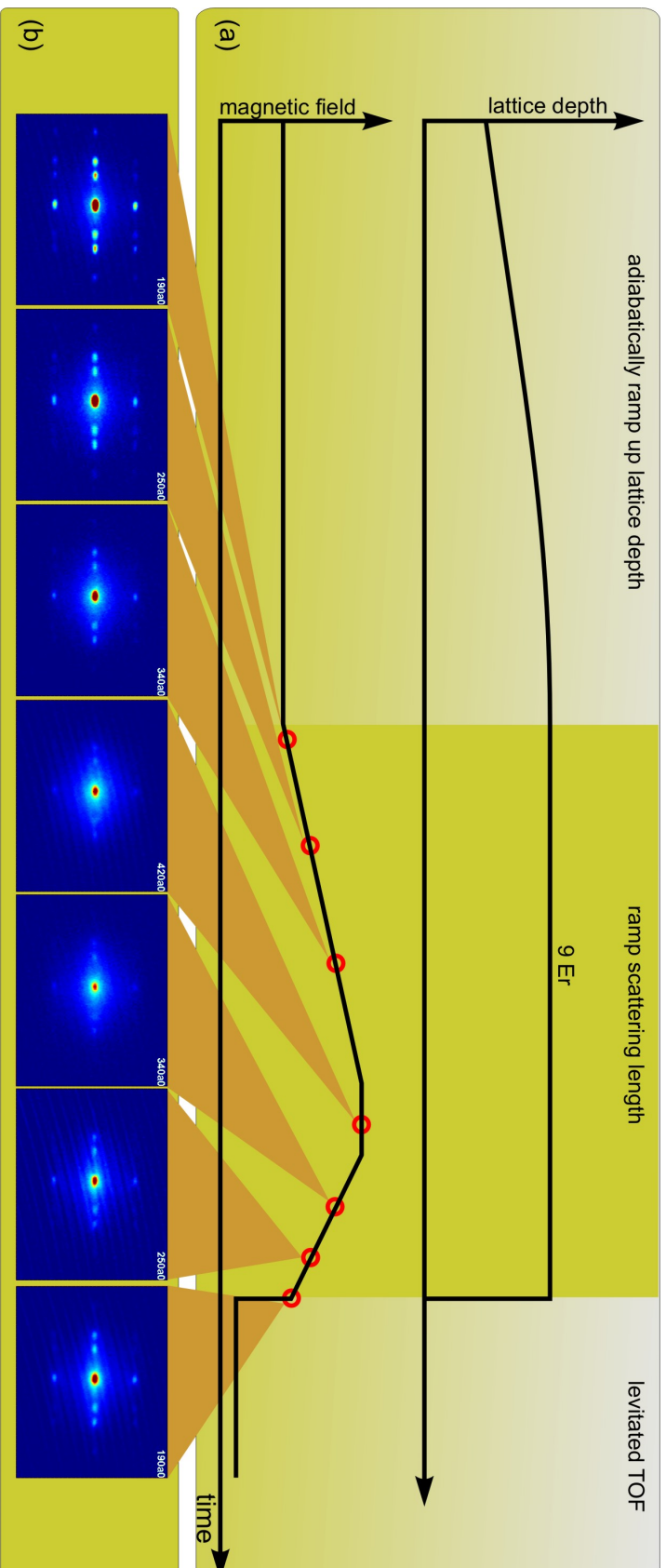


Figure 4.29: Superfluid to Mott insulator transition for a tuning of the interaction: (a) Schematic drawing of the ramping procedure of the lattice depth and scattering length. (b) TOF images taken at different stages of the sequence. Narrow interference peaks show the long range phase coherence and therefore the superfluidity of the condensate. The vanishing of the interference maxima indicates the onset of the Mott insulator regime.

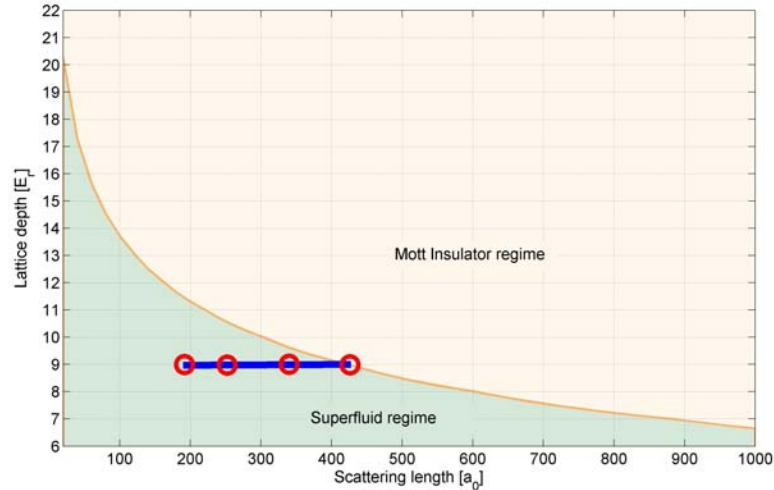


Figure 4.30: Relevant parameters for the SI to MI transition corresponding to the TOF-images shown in Fig. 4.29. The transition line in this plot is for a homogeneous system with  $\bar{n} = 1$ , i.e.  $U/6J = 5.8$ , therefore only indicating the onset of the continuous phase transition.

### 4.3.3 Probing the Excitation Spectrum

The existence of the Mott insulator phase can also be nicely demonstrated by probing the excitation spectrum. In the Mott insulating regime the atoms are localized to a single lattice site. When deep in the MI regime, i.e.  $U \gg J$ , small excitations of the system can only be achieved with energies in multiples of  $U$ . It corresponds to the energy cost due to onsite interaction if an atom hops to an neighboring lattice site (see Fig. 4.31). Therefore one expects to see an enhanced heating of the atomic ensemble only for excitations that correspond to multiples of the onsite interaction  $U$ .

#### Experimental Sequence

To probe the excitation spectrum we load the BEC into the lattice potential. Then the potential depth  $V_0$  is sinusoidally modulated by 20% with a frequency  $f_{mod}$  for a duration of 50 ms (see Fig. 4.32). This can be easily accomplished by modulating the laser intensity of one of the lattice beams via its AOM. For this we vary the amplitude of the appropriate rf-generators (DDS) sinusoidally. After the excitation the lattice is ramped down, and the momentum distribution of the cloud is imaged with the usual levitated TOF procedure. We characterize the heating of the atoms by the spatial extension of the cloud after an expansion time of 50 ms at a scattering length of  $30 a_0$ . This way the change in kinetic energy due to the excitation is better measurable.

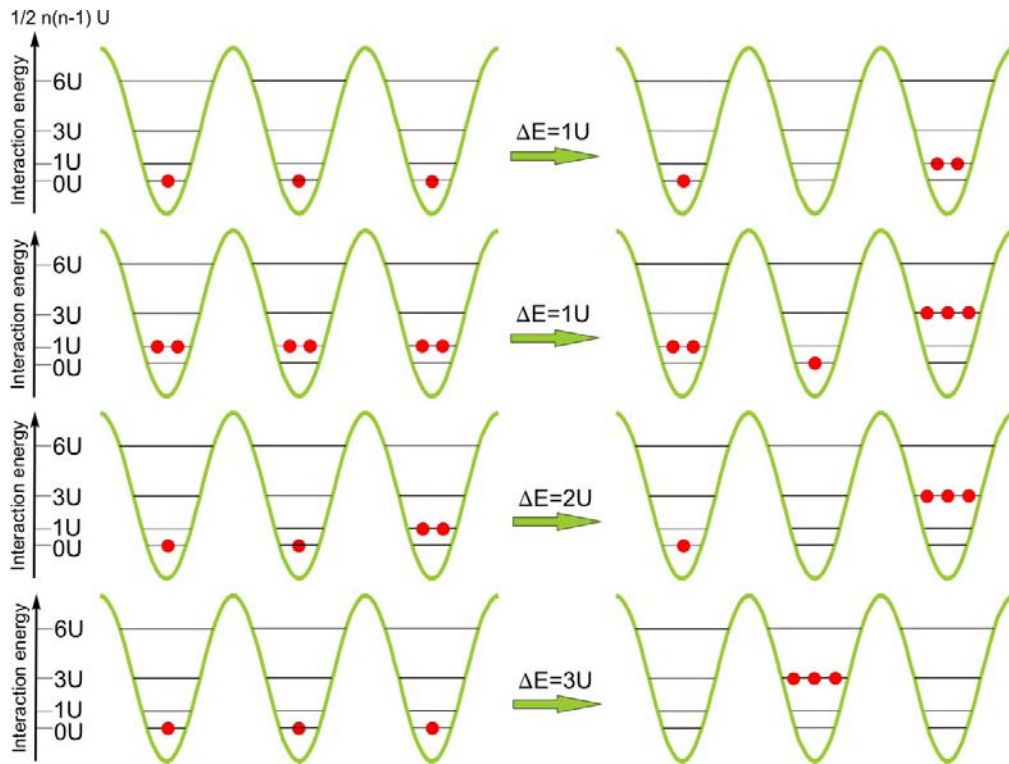


Figure 4.31: Various excitation possibilities and their corresponding change in onsite-interaction energy.

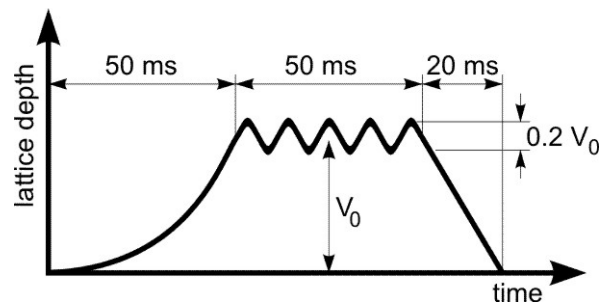


Figure 4.32: Ramping and modulation procedure of the lattice depth. To obtain the excitation spectrum, the width of the cloud was measured as a function of the modulation frequency.

## Observations

Figure 4.33(a) shows the excitation spectrum for a lattice depth of  $5 E_r$ . At this depth the system is still superfluid and therefore no resonance peaks are present. For the spectrum shown in Fig. 4.33(b) the lattice was ramped up to  $13 E_r$ . Here the system is in the Mott insulator regime, and one can clearly recognize two resonance peaks, one at 1060 Hz and one at 2100 Hz, corresponding to  $U = hf_{mod} = 0.80 E_r$  and  $2U = 1.58 E_r$ . The resulting value for  $U$  agrees well with the theoretically expected value as plotted in Fig. 4.35. For this measurement the scattering length  $a_s$  is set to  $300 a_0$ . Additionally a series of measurements with different values is performed. The scattering length is adjusted to the desired value toward the end of the evaporation process, and is left constant during the whole ramping sequence of the lattice. For the levitated TOF expansion it is always set to  $30 a_0$ .

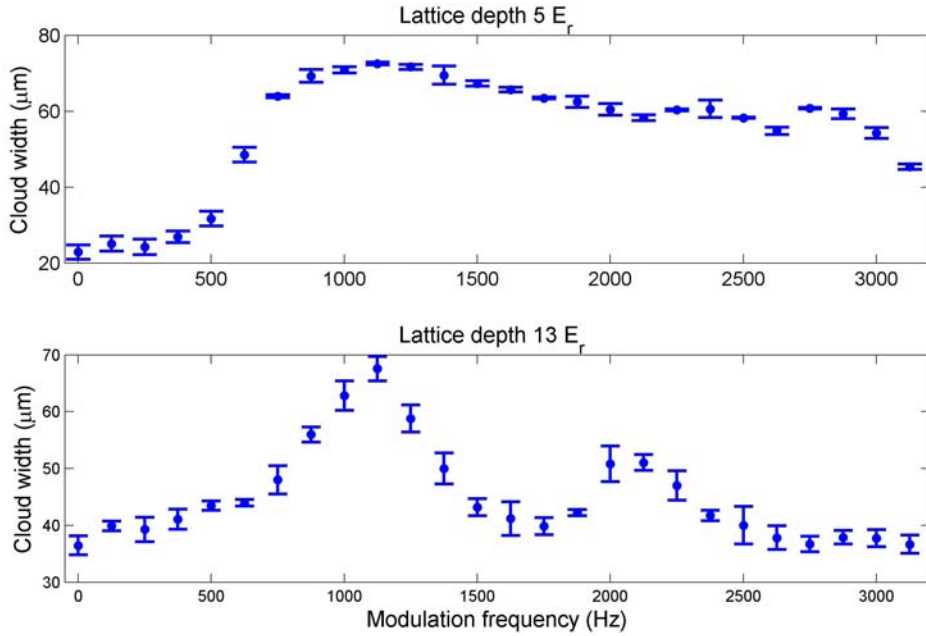


Figure 4.33: Excitation spectra while in the superfluid phase (a), and while in the Mott insulator phase (b). In (a) no resonance peaks are visible, while in (b) two peaks corresponding to  $1U$  and  $2U$  are present. Both spectra are taken with the a scattering length of  $300 a_0$ .

Figure 4.34 shows the excitation spectra for various other scattering lengths. The position of the resonance peaks is obtained by fitting a double Gaussian to the data points. The extracted values for  $U$  are plotted versus the scattering length in Fig. 4.35. The plot exhibits the expected linear dependence from Eq. 4.11, but it also seems to indicate that the calibration of the lattice depth was a bit off for this measurement. A new lattice depth calibration measurement, as described

in sec. 4.2.2, should be performed regularly and especially prior to an important measurement. This was not done prior to this excitation spectrum measurement.

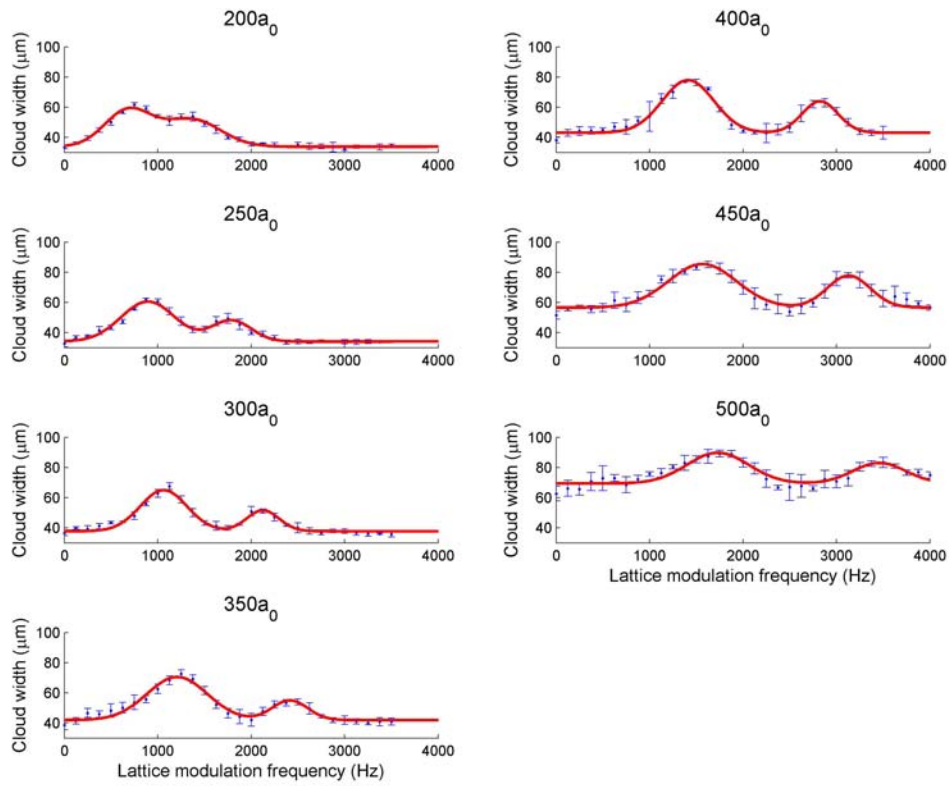


Figure 4.34: Excitation spectra for various scattering values taken at a lattice depth of  $13 E_r$ .

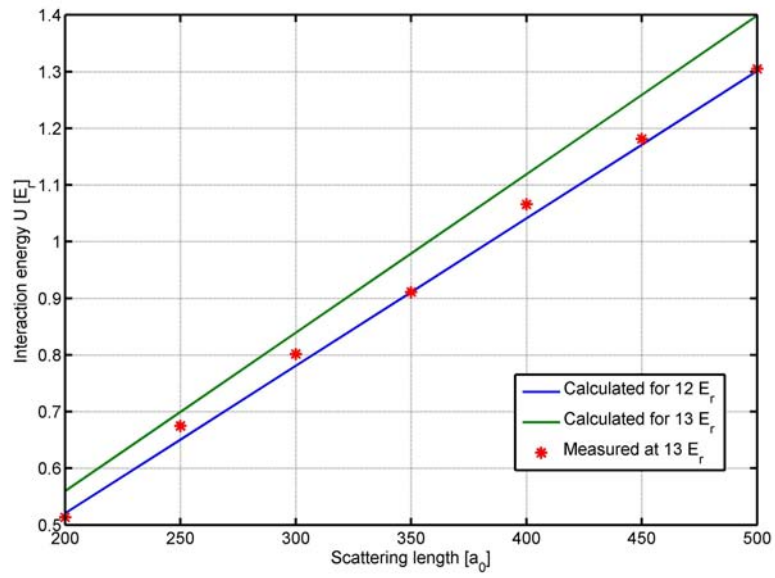


Figure 4.35: Measured onsite interaction energy  $U$  obtained from the spectra shown in Fig. 4.34 versus the scattering length. The calculated dependence for  $12 E_r$  and  $13 E_r$  is also shown.

# 5 Summary and Outlook

This diploma thesis describes the work on the experimental implementation of a three dimensional optical lattice and the realization of the superfluid to Mott insulator transition. The light provided by a fiber-amplified narrow band laser (1064 nm) is split into four beams. The light intensity of each beam can be controlled via an AOM that is driven by an amplified direct digital synthesis device (DDS). This way the light intensity and therefore the lattice depth of each lattice axis can be addressed individually with a time resolution of  $5 \mu\text{s}$ . To cancel any intensity fluctuations, the intensities are stabilized using PI-control devices. The laser light of the four beams is guided to the experimental chamber using four single mode polarization maintaining fibers each with a length of 3 to 6 meters. The optical fibers are terminated in-house with FC/APC connectors. At the glass cell the four beams are arranged to create a simple cubic lattice at the center of the atom trap. Two beams are retro-reflected to generate two mutual orthogonal standing waves (horizontal). The standing wave along the third lattice axis (vertical) is created by two counter-propagating beams. This way the lattice can be accelerated along the vertical direction. To avoid interference effects caused by mutual orthogonal beams, the laser light along the three lattice axes is mutually detuned in the MHz-regime. Therefore we obtain three mutual orthogonal 1D lattice potentials that can be used independently to create a 1D, a 2D, or a 3D lattice. The vertical 1D lattice is tested in a first measurement by the observation of Bloch oscillations.

The waist of the lattice beams ( $500 \mu\text{m}$ ) are chosen to be relatively large compared to the BEC diameter ( $\leq 40 \mu\text{m}$ ), generating a relatively homogeneous lattice potential for the atoms (if no external potential is turned on). For our setup, a laser power (after the optical fiber) of about  $40 \text{ mW}/E_r$  per beam is required. We employ the method presented in [Den02] for the a calibration of the lattice depth. Currently a maximal lattice depth of  $25 - 30 E_r$  can be achieved. On a long time scale (weeks) the maximal lattice depth is currently limited by some sort of a thermal lensing effect. As the other main characterization measurement the heating of the BEC in the lattice is determined. The decrease of the BEC fraction while held in 3D lattice is determined to be approximately  $\frac{0.5\%}{100 \text{ ms } 1 E_r}$ .

In preliminary measurements we are able to drive the superfluid to Mott insulator quantum phase transition by ramping the lattice depth as done in [Gre02a]. The vanishing of the characteristic momentum peaks, attributed to the loss of long range phase coherence, can be observed as the lattice depth is ramped up. The interference pattern can be restored by ramping the lattice depth below the transition point. Additionally -and this is absolutely new- we present promising

indications that we are able to drive the SF to MI transition by tuning the scattering length, i.e. the interaction energy. In yet another experiment we probe the excitation spectrum of the system in the MI regime as a function of the scattering length.

In summary we have implemented a 3D lattice that fulfills the proposed requirements and, as shown in this work, is ready to be used for novel experiments involving a tunable BEC in a lattice potential. For a solid interpretation of effects observed on a long time scale, a thorough characterization of the lattice-potential's imperfections which are possibly caused by technical limitations is necessary. Among other, the mechanical stability of the optical setup is currently investigated. Also the parameters for ramping the lattice depth are examined in more detail, as the intraband adiabaticity criterion might be more stringent than previously assumed, especially for 1D lattices [McK06].

For the immediate future various opportunities for experiments involving a tunable Cs BEC in an optical lattice exist. They include:

- Measurement and characterization of interaction-induced dephasing of Bloch oscillations in a 1D lattice potential [Buc03]. Condensed Cs atoms allow a narrow momentum spread in combination with minimal dephasing by switching the interaction strength to zero. In fact, residual dephasing could be used as a measure to determine the strength of weak interactions. This would be particularly important in view of an atom interferometer relying on near-zero interaction strength.
- To drive the SF to MI transition deep into the MI regime and back with tunable interactions. An improved version of the measurement described in sec. 4.3.2.
- Controlled production of molecules in the ground state of the lattice potential. The MI state allows to prepare the amazing condition where precisely two atoms are located in each lattice site. This makes an controlled association of dimer molecules possible, as recently demonstrated for the case of Rb atoms on a narrow Feshbach resonance near 1000 G [Tha06]. For Cs atoms with sufficiently broad Feshbach resonances at low magnetic fields, further control is within reach because it will be possible to tune onto the resonances in contrast to mere sweeps, for example near the 48 G resonance. Also, the rich molecular structure can be exploited for realization of molecular interferometers [Mar07] in the presence of the lattice and for the controlled investigation of molecular Feshbach resonances [Chi05].

The intermediate and long term goals involving the optical lattice include:

- Measurement of collisional properties for two atoms at a time. In view of the importance of Cs atoms for atomic clocks and for fundamental reasons the collisional properties for Cs atoms in states other than the hyperfine quantum state  $F = 3$ ,  $m_F = 3$  can be mapped out. For this, one would

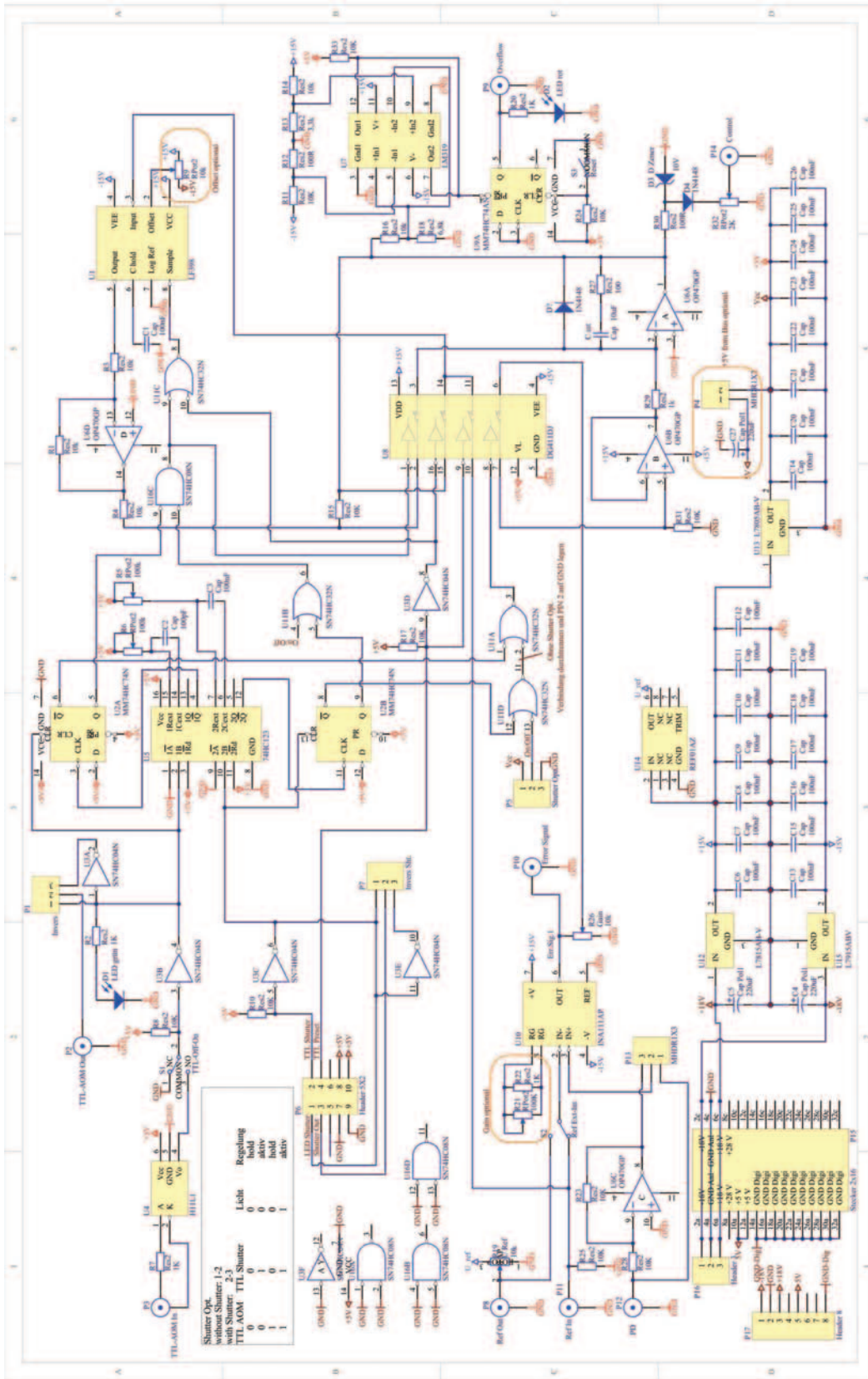
prepare the ideal situation of precisely two ground state atoms per lattice site. Radio-frequency pulses and appropriately chosen magnetic fields can then transfer (coherently) the full population into any desired hyperfine state, in particular into the clock state  $F = 3$ ,  $m_F = 0$ , allowing a measurement of the so-called clock shifts [Leo01] in the regime of ultralow temperatures. Such state-transfer techniques could be used to test the feasibility of BEC in other hyperfine states of the Cs atom, and for the search of new Feshbach resonances.

- Measurement of collisional properties for three atoms at a time. In light of the recent evidence for Efimov quantum states [Kra06], it should be possible to investigate the formation and stability of Efimov trimers in the presence of a lattice [Sto05]. Interferometric techniques might even give information on the three-body collisional phase. A full observation of Efimov's scenario might be possible near broad s-wave Feshbach resonances at 550 G and 800 G.

Another exciting line of research will be the realization of atom interferometers for the precision measurement of fundamental constants, e.g. the fine structure constant  $\alpha$  [Gup02]. Atom interferometers rely on the matter wave diffraction of atoms from a grating in the form of one-dimensional standing laser waves, and they are thus in a natural connection with the matter waves in optical lattices as outlined above. A prime advantage of Cs is again the possibility to tune the interaction strength by tuning the scattering length  $a_s$ , in this case to minimize the mean-field interaction of the condensate.



# Appendix A



Electronic circuit of PI-control. Designed by Gerhard Hendl, Institut fuer Quantenoptik und Quanteninformaton, Austria



## Appendix B

### Calculating the Bloch and Wannier functions

In sec. 4.1.1 we obtained the following Schrödinger equation for  $u_q^n(x)$  by inserting the Bloch ansatz into the time independent Schrödinger equation:

$$H_q u_q^n(x) = E_q^n u_q^n(x), \quad \text{with} \quad H_q = \frac{(\hat{p} + q)^2}{2m} - V_{01D} \cos^2(kx). \quad (5.1)$$

This appendix points out how this equation was numerically solved using MATLAB, to obtain some of the plots that are shown within this work.

Since the potential  $V$  and the functions  $u_q^n(x)$  are periodic with the same periodicity, they both can be written as discrete Fourier sums:

$$-V_{01D} \cos^2(kx) \cos^2(kx) = -V_{01D} (e^{2ikx} + e^{-2ikx} + 2) \quad (5.2)$$

$$u_q^n(x) = \sum_l c_l^{n,q} e^{l2ikx} \quad (5.3)$$

Inserting 5.2 and 5.3 into 5.1 yields

$$\begin{aligned} \frac{1}{2m} \sum_l (2l\hbar k + q)^2 c_l^{n,q} e^{l2ikx} - \sum_l \frac{V_{01D}}{4} c_{l-1}^{n,q} e^{l2ikx} - \sum_l \frac{V_{01D}}{4} c_{l+1}^{n,q} e^{l2ikx} - \\ - \sum_l \frac{V_{01D}}{2} c_l^{n,q} e^{l2ikx} = \sum_l E_q^n c_l^{n,q} e^{l2ikx}. \end{aligned} \quad (5.4)$$

Because all  $e^{l2ikx}$  are mutual orthogonal functions, we obtain  $l$  equations that must be fulfilled independently. They can be written in matrix form as follows

$$\begin{pmatrix} \ddots & \vdots & & & & & \\ \cdots & A_{-1} + C & B & 0 & & & \\ & B & A_0 + C & B & & & \\ & 0 & B & A_{+1} + C & \cdots & & \\ & & & \vdots & \ddots & & \end{pmatrix} \begin{pmatrix} \vdots \\ c_{-1}^{n,q} \\ c_0^{n,q} \\ c_{+1}^{n,q} \\ \vdots \end{pmatrix} = \begin{pmatrix} \vdots \\ c_{-1}^{n,q} \\ c_0^{n,q} \\ c_{+1}^{n,q} \\ \vdots \end{pmatrix} E_q^n, \quad (5.5)$$

where  $A_l = \frac{(2l\hbar k + q)^2}{2m}$ ,  $B = \frac{-V_{01D}}{4}$ , and  $C = \frac{-V_{01D}}{2}$ , or  $A_l = (2l + q)^2$ ,  $B = \frac{-V_{01D}}{4E_r}$ , and  $C = \frac{-V_{01D}}{2E_r}$  if we want the energies to be in units of recoil energies  $E_r$  and the quasimomentum in units of  $\hbar k$ .

Hence, the eigenvalues  $E_q^n$  of this matrix represent the eigenenergies in the  $n^{\text{th}}$  energy band. The corresponding eigenvector  $c^{n,q}$  defines the appropriate Bloch wave function through 5.3 and 4.2. This eigenwert problem can simply be calculated if the matrix is truncated for large positive and negative  $l$ , e.g. a restriction to  $-5 \leq l \leq 5$  is a good choice if only the lowest energy bands are to be considered. Note that the term  $C$  creates only an energy offset and can therefore be chosen

arbitrarily or omitted. The sign of term  $B$  is also irrelevant for the dynamics in a homogeneous lattice, since writing  $V$  with  $\sin^2$  instead of  $\cos^2$ , would yield the opposite sign for  $B$ .

The following is a MATLAB code that plots the energy band structure, the Bloch function of the lowest energyband for different values of  $q$ , the absolute square of the Bloch and Wannier functions of the lowest energy band for various lattice depths. It also plots the tunneling matrix element  $J$  and the onsite interaction energy  $U$  as a function of the lattice depth  $V_0$ . Further, the plane wave decomposition of the Bloch function with  $q = 0$  for the lowest four bands is plotted.

```

clear
%*****Variablendeklaration*****
hbar=1.0545726*10^-34;
m=133*1.6605402*10^-27;
a0=5.2917725*10^-11;
as=200*a0;
lambda=1064*10^-9;
k=2*pi/lambda;
Er=hbar^2*k^2/2/m;
%indizes von V0_vec, von denen Blochbänder,
V0_plot=[1 6 16]; %-funktionen, und Wannierfkten geplottet werden sollen
V0_max=25; %lattice depth
V0_unt=V0_max; % unterteilungen von V0 (rechnet also für jedes Er aus)
V0_vec=linspace(0,V0_max,V0_unt+1);

l_tot=5; %größe vom hamilton operator
l_vec=linspace(-l_tot,l_tot,2*l_tot+1);

xi_range=2; %xi=x/a von e.g. -3 bis +3 gitterplätzen
xi_unt=100; %unterteilungen
xi_vec=linspace(-xi_range,xi_range,xi_unt+1);
dxi=2*xi_range/xi_unt;
dx=dxi*lambda/2;

qi_range=1; %qi=q/(hbar*k) with q quasimomentum
qi_unt=100; % anzahl der unterteilungen von qi
qi_vec=linspace(-qi_range,qi_range,qi_unt+1);
dqi=2*qi_range/qi_unt;
dq=dqi*hbar*k;
H=zeros(2*l_tot+1,2*l_tot+1); %Hamiltonian

E=zeros(2*l_tot+1,qi_unt+1,V0_unt+1); %energie

gitter=(sin(xi_vec*pi)).^2; %erzeugt gitter funktion mit periodizität
%lambda/2, fürs plotten

eb_Wellen2k=zeros(xi_unt+1,2*l_tot+1); %matrix mit den benötigten ebenen Wellen mit
for xii=1:xi_unt+1 %wellenzahl=vielfaches von 2k
    xi=xi_vec(xii); %gleiche zeile=gleicher ort
    for lj=1:2*l_tot+1 %gleiche spalte= gleiche wellenzahl
        li=l_vec(lj);

```

```

        eb_Wellen2k(xii,ljj)=exp(i*li*2*pi*xi);
    end;
end;

uq=zeros(xi_unt+1,2*l_tot+1);          %u-funktionen, gl zeile =gl ort, gl spalte= gl band

Blochfun0=zeros(xi_unt+1,qi_unt+1,V0_unt+1);    %Blochfunktionen für 0. band
Blochfun1=zeros(xi_unt+1,qi_unt+1,V0_unt+1);    %gleiche zeile=gl ort
Blochfun2=zeros(xi_unt+1,qi_unt+1,V0_unt+1);    %gl spalte= gleiches q

Wanfun0=zeros(xi_unt+1,V0_unt+1);                %Wannierfunktion für 0. Band

%*****Berechnungen*****
for VOi=1:V0_unt+1
    V0=V0_vec(VOi);
for qii=1:qi_unt+1
    qi=qi_vec(qii);

    for lii=1:2*l_tot+1          %build up hamiltonian
        li=l_vec(lii);
        for ljj=1:2*l_tot+1
            lj=l_vec(ljj);
            if (li==lj)
                if (li~-l_tot) H(lii,ljj-1)=-V0/4; end;
                H(lii,ljj)=(2*li+qi)^2+V0/2;
                if (li~=l_tot) H(lii,ljj+1)=-V0/4; end;
            end;
        end;
    end;
    %E(:,ai)=eig(H);
    [cqn,E_matrix]=eig(H);          %berechnet eigenwerte, eigenvectoren
    if (qi==0) c0n=cqn;
    end;
    E(:,qii,VOi)=E_matrix*ones(2*l_tot+1,1);
    uq=eb_Wellen2k*abs(cqn);        %berechnet u-Funktionen:uqn=summe(l)cqn*exp(i2lkx)
                                    %absolut ist wichtig da EV zufällig + oder - rauskommen

    %figure(2)
    % plot(xi_vec,real(uq)) %plottet die u-Funktionen für alle q's
    % hold on

for xii=1:xi_unt+1          %stellt bloch funktionen aus den u-funktionen zusammen
    xi=xi_vec(xii);        %gleiche zeile=gleicher ort, gleiche spalte= gleiche wellenzahl
    Blochfun0(xii,qii,V0i)=exp(i*pi*qi*xi)*uq(xii,1);
    Blochfun1(xii,qii,V0i)=exp(i*pi*qi*xi)*uq(xii,2);
    Blochfun2(xii,qii,V0i)=exp(i*pi*qi*xi)*uq(xii,3);
    Blochfun3(xii,qii,V0i)=exp(i*pi*qi*xi)*uq(xii,4);
    Blochfun4(xii,qii,V0i)=exp(i*pi*qi*xi)*uq(xii,5);
end;

end;
Wanfun0_unnorm=sum(Blochfun0(:,:,V0i),2);          %berechnet wannierfunktion, unnormiert

```

```

Norm=sum((abs(Wanfun0_unnorm)).^2)*dx;
Wanfun0(:,V0i)=Wanfun0_unnorm/sqrt(Norm);           %normiert die wannierfkt

J1(V0i)=(max(E(1,:,V0i))-min(E(1,:,V0i)))/4;       %berechnet U und J
U(V0i)=4*pi*hbar^2*as/m/Er*(sum((abs(Wanfun0(:,V0i))).^4)*dx)^3;
end;

%*****Ausgabe / Plotten*****
plnu=length(V0_plot);
if (plnu>3)
    plrow=2;
    plcol=ceil(plnu/plrow);
elseif (plnu>6)
    plrow=3;
    plcol=ceil(plnu/plrow);
else
    plrow=1;
    plcol=plnu;
end;

figure(11) %plottet band struktur
for pli=1:length(V0_plot)
    subplot(plrow,plcol,pli),plot(qi_vec,E(1:5,:,V0_plot(pli))','LineWidth',2)
    axis([-qi_range qi_range 0 V0_max])
    if (pli>(plrow-1)*plcol)
        xlabel('q [ $\hbar k$ '],'interpreter','latex')
    end;
    if (pli/plcol-floor(pli/plcol)==1/plcol)
        ylabel('E [E_r]')
    end;
    title(['V_0 = ',num2str(V0_vec(V0_plot(pli))),' E_r'])
end;

figure(13) %plottet bloch funktionen vom 0.ten band
for pli=1:length(V0_plot)
    subplot(plrow,plcol,pli),plot(xi_vec,real(Blochfun0(:, :, V0_plot(pli))))
    set(gca,'YTick',[])
    if (pli>(plrow-1)*plcol)
        xlabel('x [a]')
    end;
    if (pli/plcol-floor(pli/plcol)==1/plcol)
        ylabel('Re( $\phi_{q^0}$ ) [a.u.]')
    end;
    title(['V_0 = ',num2str(V0_vec(V0_plot(pli))),' E_r'])
end;

figure(14) %plottet betragquadrat der blochfkten vom 0.ten band für q=0 und q=hquer k
for pli=1:length(V0_plot)
    subplot(plrow,plcol,pli),
    plot(xi_vec,(abs(Blochfun0(:,qi_unt/2+1,V0_plot(pli))))).^2,'LineWidth',1)
    hold on
    subplot(plrow,plcol,pli),

```

```

plot(xi_vec, (abs(Blochfun0(:, qi_unt+1, V0_plot(pli))))).^2, '--k', 'LineWidth', 1)
hold off
set(gca, 'YTick', [])
if (pli > (plrow-1)*plcol)
    xlabel('x [a]')
end;
if (pli/plcol - floor(pli/plcol) == 1/plcol)
    ylabel('| $\phi_q^0(x)|^2$  [a.u.]')
end;
title(['V_0 = ', num2str(V0_vec(V0_plot(pli))), ' E_r'])
end;

figure(15) %plottet betragsquad. der wannierfkt des 0ten bandes
for pli=1:length(V0_plot)
    hohe=max((abs(Wanfun0(:, V0_plot(length(V0_plot))))).^2 * dx);
    if (V0_vec(V0_plot(pli)) == 0) gitterhohe=0;
    else gitterhohe=hohe;
    end;
    subplot(plrow, plcol, pli),
    plot(xi_vec, (abs(Wanfun0(:, V0_plot(pli))))).^2 * dx, 'LineWidth', 2)
    axis([-xi_range xi_range 0 hohe])
    hold on
    subplot(plrow, plcol, pli), plot(xi_vec, gitter*gitterhohe, 'r')
    hold off
    %set(gca, 'YTick', [])
    if (pli > (plrow-1)*plcol)
        xlabel('x [a]')
    end;
    if (pli/plcol - floor(pli/plcol) == 1/plcol)
        ylabel('|w_0(x-x_0)|^2')
    end;
    title(['V_0 = ', num2str(V0_vec(V0_plot(pli))), ' E_r'])
end;

figure(16) %plottet tunnelwert J
plot(V0_vec, J1)
xlabel('lattice depth V0 [E_r]')
ylabel('tunnel term J [E_r]')
title('Tunnel Term J')

figure(17) %plottet wechselwirkung U
plot(V0_vec, U)
xlabel('lattice depth V0 [E_r]')
ylabel('interaction energy [E_r]')
title('Onsite Interaction Energy')

figure(18) %plottet die band -> plane wave decomposition
for pli=1:4
    subplot(1,4, pli), bar(l_vec*2, (abs(c0n(:, pli))))).^2)
    axis([-8 8 0 0.6])
    title(['Band n=', num2str(pli-1)])
    if (pli==1) ylabel('probability |a_{n,0}(1)|^2')
end;

```

```

end;
%if (pli==2)
text(2,-0.07,'plane wave with momentum  $p=2l\hbar k$ ','interpreter','latex')
%end;
xlabel('2l')
end;

figure(19) %plottet die plane wave -> band decomposition
for pli=1:4
subplot(1,4,pli),bar([0:10],(abs(c0n(l_tot+pli,:))').^2)
axis([-1 8 0 0.6])
title(['plane wave e^{i2lkx}, l=',num2str(-1+pli)])
if (pli==1) ylabel('probability  $|a_{n,0}^{(1)}|^2$ ')
end;
%if (pli==2) text(5,-0.07,'wavefunction  $|n,0\rangle$ ','interpreter','latex')
%end;
xlabel('n')
end;

```

# Bibliography

- [AL03] H. Z. A. Liem, J. Limpert and A. Tünnermann, *100-W single-frequency master-oscillator fiber power amplifier*, Opt. Lett. **28**, 1537 (2003).
- [Ami98] L. Amico and V. Penna, *Dynamical Mean Field Theory of the Bose-Hubbard Model*, Phys. Rev. Lett. **80**, 2189 (1998).
- [And95] M. H. Anderson, J. R. Ensher, M. R. Matthews, C. E. Wieman, and E. A. Cornell, *Observation of Bose-Einstein Condensation in a Dilute Atomic Vapor*, Science **269**, 198 (1995).
- [And97] M. R. Andrews, C. G. Townsend, H.-J. Miesner, D. S. D. and D. M. Kurn, and W. Ketterle, *Observation of Interference Between Two Bose-Einstein Condensates*, Science **275**, 637 (1997).
- [And98] B. P. Anderson and M. A. Kasevich, *Macroscopic Quantum Interference from Atomic Tunnel Arrays*, Science **282**, 1686 (1998).
- [AS01] J. R. Abo-Shaeer, C. Raman, J. M. Vogels, and W. Ketterle, *Observation of Vortex Lattices in Bose-Einstein Condensates*, Science **292**, 476 (2001).
- [BD96] M. Ben Dahan, E. Peik, J. Reichel, Y. Castin, and C. Salomon, *Bloch Oscillations of Atoms in an Optical Potential*, Phys. Rev. Lett. **76**, 4508 (1996).
- [Bes99] G. Best and O. M. Sezerman, *Shedding light on hybrid optics: A tutorial in coupling* (1999), download: [http://www.ozoptics.com/ALLNEW\\_PDF/ART0002.pdf](http://www.ozoptics.com/ALLNEW_PDF/ART0002.pdf).
- [BIP98] BIPM, *Le System International d'Unites (SI)*, Tech. rep., Bureau International des Poids et Mesures, Sevres, France (1998).
- [Blo29] F. Bloch, *Über die Quantenmechanik der Elektronen in Kristallgittern*, Z. Physik **52**, 555 (1929).
- [Bos24] S. Bose, *Plancks Gesetz und Lichtquantenhypothese*, Z. Phys. **26**, 178 (1924).
- [Bou82] M. Bouchiat, J. Guena, L. Hunter, and L. Pottier, *Observation of a parity violation in cesium*, Physics Letters B **117**, 358 (1982).

- [Buc03] A. Buchleitner and A. R. Kolovsky, *Interaction-Induced Decoherence of Atomic Bloch Oscillations*, Phys. Rev. Lett. **91**, 253002 (2003).
- [Car05] I. Carusotto, L. Pitaevskii, S. Stringari, G. Modugno, and M. Inguscio, *Sensitive Measurement of Forces at the Micron Scale Using Bloch Oscillations of Ultracold Atoms*, Physical Review Letters **95**, 093202 (2005).
- [Chi00] C. Chin, V. Vuletic, A. J. Kerman, and S. Chu, *High Resolution Feshbach Spectroscopy of Cesium*, Phys. Rev. Lett. **85**, 2717 (2000).
- [Chi01a] C. Chin, *Cooling, Collisions and Coherence of Cold Cesium Atoms in a Trap*, Ph.D. thesis, Stanford University (2001).
- [Chi01b] C. Chin, V. Leiber, V. Vuletić, A. J. Kerman, and S. Chu, *Measurement of an electron's electric dipole moment using Cs atoms trapped in optical lattices*, Phys. Rev. A **63**, 33401 (2001).
- [Chi04] C. Chin, V. Vuletic, A. J. Kerman, S. Chu, E. Tiesinga, P. Leo, and C. J. Williams, *Precision Feshbach spectroscopy of ultracold Cs<sub>2</sub>*, Phys. Rev. A **70**, 032701 (2004).
- [Chi05] C. Chin, T. Kraemer, M. Mark, J. Herbig, P. Waldburger, H.-C. Nägerl, and R. Grimm, *Observation of Feshbach-like resonances in collisions between ultracold molecules*, Phys. Rev. Lett. **94**, 123201 (2005).
- [Dal99] J. Dalibard, *Collisional dynamics of ultra-cold atomic gases*, in: M. Inguscio, S. Stringari, and C. E. Wieman (Eds.), *Proceedings of the International School of Physics - Enrico Fermi*, 321, IOS Press, 1999.
- [Dav94] N. Davidson, H. Lee, M. Kasevich, and S. Chu, *Raman Cooling of Atoms in Two and Three Dimensions*, Phys. Rev. Lett. **72**, 3158 (1994).
- [Dav95] K. B. Davis, M.-O. Mewes, M. R. Andrews, N. J. van Druten, D. Durfee, D. M. Kurn, and W. Ketterle, *Bose-Einstein Condensation in a Gas of Sodium Atoms*, Phys. Rev. Lett. **75**, 3969 (1995).
- [Den00] J. Denschlag, J. E. Simsarian, D. L. Feder, C. W. C. and L. A. Collins, J. Cubizolles, L. Deng, E. W. Hagley, K. H. W. P. Reinhardt, S. L. Rolston, B. I. Schneider, and W. D. Phillips, *Generating Solitons by Phase Engineering of a Bose-Einstein Condensate*, Science **287**, 97 (2000).
- [Den02] J. H. Denschlag, J. E. Simsarian, H. Häffner, C. McKenzie, A. Browaeys, D. Cho, K. Helmerson, S. L. Rolston, and W. D. Phillips, *A Bose-Einstein condensate in an optical lattice*, Journal of Physics B **35**, 3095 (2002).
- [Ein25] A. Einstein, *Quantentheorie des einatomigen idealen Gases. Zweite Abhandlung*, Sitzungber. Preuss. Akad. Wiss. **1925**, 3 (1925).

- [Els99] N. Elstner and H. Monien, *Dynamics and Thermodynamics of the Bose-Hubbard model*, Phys. Rev. B **59**, 12184 (1999).
- [Fis89] M. P. A. Fisher, P. B. Weichman, G. Grinstein, and D. S. Fisher, *Boson localization and the superfluid-insulator transition*, Phys. Rev. B **40**, 546 (1989).
- [Fli06] A. Flir, *Implementierung und Untersuchung von Raman-Seitenbandkühlung zur Erzeugung eines ultrakalten Cäsium-gases*, Master's thesis, University of Innsbruck (2006), download: <http://www.ultracold.at>.
- [Geh98] M. E. Gehm, K. M. O'Hara, T. A. Savard, and J. E. Thomas, *Dynamics of noise-induced heating in atom traps*, Phys. Rev. A **58**, 3914 (1998).
- [Ger07] T. Gericke, F. Gerbier, A. Widera, S. Foelling, O. Mandel, and I. Bloch, *Adiabatic loading of a Bose-Einstein condensate in a 3D optical lattice*, Journal of Modern Optics **54**, 735–743 (2007).
- [Gre02a] M. Greiner, O. Mandel, T. Esslinger, and T. W. H. I. Bloch, *Quantum phase transition from a superfluid to a Mott insulator in a gas of ultracold atoms*, Nature **415**, 39 (2002).
- [Gre02b] M. Greiner, O. Mandel, T. W. Hänsch, and I. Bloch, *Collapse and revival of the matter wave field of a Bose-Einstein condensate*, Nature **419**, 51 (2002).
- [Gre03] M. Greiner, *Ultracold quantum gases in three-dimensional optical lattice potentials*, Ph.D. thesis, Ludwig-Maximilians-Universität München (2003).
- [Gri00] R. Grimm, M. Weidemüller, and Y. Ovchinnikov, *Optical dipole traps for neutral atoms*, Adv. At. Mol. Opt. Phys. **42**, 95 (2000),
- [Gui99] L. Guidoni and P. Verkerk, *Optical lattices: cold atoms ordered by light*, Journal of Optics B: Quantum and Semiclassical Optics **1**, R23 (1999).
- [Gup02] S. Gupta, K. Dieckmann, Z. Hadzibabic, and D. E. Pritchard, *Contrast Interferometry using Bose-Einstein Condensates to Measure  $h/m$  and  $\alpha$* , Phys. Rev. Lett. **89**, 140401 (2002).
- [Hal] E. Haller, *Phd thesis unpublished*, university of Innsbruck.
- [Hen00] J. Hensley, A. Whicht, B. Young, and S. Chu, *Progress towards a Measurement of  $h/M$* , in: E. Arimondo, P. D. Natale, and M. Inguscio (Eds.), *Proc. 17th Int. Conf. Atomic Physics*, 43–57, AIP, Melville, New York, 2000.

- [Her03] J. Herbig, T. Kraemer, M. Mark, T. Weber, C. Chin, H.-C. Nägerl, and R. Grimm, *Preparation of a Pure Molecular Quantum Gas*, Science **301**, 1510 (2003), published online 21 Aug 2003, doi10.1126/science.1088876.
- [Her05] J. Herbig, *Quantum degenerate Cesium: Atoms and Molecules*, Ph.D. thesis, Innsbruck University (2005), download: <http://www.ultracold.at>.
- [Ino98] S. Inouye, M. R. Andrews, J. Stenger, H.-J. Miesner, and D. M. S.-K. W. Ketterle, *Observation of Feshbach resonances in a Bose-Einstein condensate*, Nature **392**, 151 (1998).
- [Ino99] S. Inouye, T. Pfau, S. Gupta, A. P. Chikkatur, A. G. D. E. Pritchard, and W. Ketterle, *Phase-coherent amplification of atomic matter waves*, Nature **402**, 641 (1999).
- [Ise05] L. Isella and J. Ruostekoski, *Nonadiabatic dynamics of a Bose-Einstein condensate in an optical lattice*, Physical Review A **72**, 011601 (2005).
- [Jak99] D. Jaksch, *Bose-Einstein condensation and applications*, Ph.D. thesis, University of Innsbruck (1999).
- [Jul05] P. S. Julienne, C. J. Williams, Y. B. Band, and M. Trippenbach, *Loading Bose-Einstein-condensed atoms into the ground state of an optical lattice*, Physical Review A **72**, 053615 (2005).
- [Kam93] A. P. Kampf and G. T. Zimanyi, *Superconductor-insulator phase transition in the boson Hubbard model*, Phys. Rev. B **47**, 279 (1993).
- [Kas02] V. A. Kashurnikov, N. V. Prokof'ev, and B. V. Svistunov, *Revealing the superfluid-Mott-insulator transition in an optical lattice*, Phys. Rev. A **66**, 031601 (2002).
- [Ket99] W. Ketterle, D. S. Durfee, and D. M. Stamper-Kurn, *Making, probing and understanding Bose-Einstein condensates*, in: M. Inguscio, S. Stringari, and C. E. Wieman (Eds.), *Proceedings of the International School of Physics - Enrico Fermi*, 67, IOS Press, 1999, arxivcond-mat/9904034.
- [Köh06] T. Köhler, K. Góral, and P. S. Julienne, *Production of cold molecules via magnetically tuneable Feshbach resonances*, Reviews of Modern Physics **78**, 1311 (2006).
- [Kit04] C. Kittel, *Introduction to solid state physics*, Wiley (8th ed), 2004.
- [Kol04] A. R. Kolovsky, *Bloch oscillations in the Mott-insulator regime*, Physical Review A **70**, 015604 (2004).
- [Kra04] T. Kraemer, J. Herbig, M. Mark, T. Weber, C. Chin, H.-C. Nägerl, and R. Grimm, *Optimized production of a cesium Bose-Einstein condensate*, Appl. Phys. B **79**, 1013 (2004).

- [Kra06] T. Kraemer, M. Mark, P. Waldburger, J. Danzl, C. Chin, B. Engeser, A. Lange, K. Pilch, A. Jaakola, H.-C. Nägerl, and R. Grimm, *Evidence for Efimov quantum states in an ultracold gas of caesium atoms*, Nature **440**, 315 (2006).
- [Leo01] P. J. Leo, P. S. Julienne, F. H. Mies, and C. J. Williams, *Collisional Frequency Shifts in  $^{133}\text{Cs}$  Fountain Clocks*, Phys. Rev. Lett. **86**, 3743 (2001).
- [Mar07] M. Mark, T. Kraemer, P. Waldburger, J. Herbig, C. Chin, H. C. Naegerl, and R. Grimm, *'Stückelberg interferometry' with ultracold molecules* (2007).
- [McK06] S. B. McKagan, D. L. Feder, and W. P. Reinhardt, *An Investigation of Mean-field Effects for a Bose Condensate in an Optical Lattice*, Physical Review A (Atomic, Molecular, and Optical Physics) **74**, 013612 (2006).
- [Met99] H. J. Metcalf and P. van der Straten, *Laser cooling and trapping*, Springer-Verlag, New York, 1999.
- [Mey] T. P. Meyrath and F. Schreck, *Digital RF Synthesizer: DC to 135 MHz*, Atom Optics Laboratory, University of Texas at Austin, <http://george.ph.utexas.edu/control/index.html>, august 10, 2005 ed.
- [New] Newport, *Photonics Tutorial*, [www.newport.com](http://www.newport.com).
- [Orz01] C. Orzel, A. K. Tuchman, M. L. Fenselau, M. Yasuda, and M. A. Kasevich, *Squeezed States in a Bose-Einstein Condensate*, Science **291**, 2386 (2001).
- [Pet94] K. I. Petsas, A. B. Coates, and G. Grynberg, *Crystallography of optical lattices*, Phys. Rev. A **50**, 5173 (1994).
- [Pit03] L. Pitaevskii and S. Stringari, *Bose-Einstein Condensation*, International Series of Monographs on Physics 116, Oxford University Press, 2003.
- [Reg03] C. A. Regal, C. Ticknor, J. L. Bohn, and D. S. Jin, *Creation of ultracold molecules from a Fermi gas of atoms*, Nature **424**, 47 (2003).
- [Ryc04] D. Rychtarik, B. Engeser, H.-C. Nägerl, and Rudolf Grimm, *Two-Dimensional Bose-Einstein Condensate in an Optical Surface Trap*, Phys. Rev. Lett. **92**, 173003 (2004), doi10.1103/PhysRevLett.92.173003.
- [Sch] F. Schreck, *Manual of experiment control system CONTROL*, University of Innsbruck, <http://george.ph.utexas.edu/control/index.html>, march 23, 2003 ed.

- [Sco04] R. G. Scott, A. M. Martin, S. Bujkiewicz, T. M. Fromhold, N. Malossi, O. Morsch, M. Cristiani, and E. Arimondo, *Transport and disruption of Bose-Einstein condensates in optical lattices*, Physical Review A **69**, 033605 (2004).
- [Sel04] J. Selim, *Bose-Einstein Condensation of Molecules*, Ph.D. thesis, University of Innsbruck (2004), download: <http://www.ultracold.at>.
- [SK98] D. M. Stamper-Kurn, H.-J. Miesner, A. P. Chikkatur, S. I. and J. Stenger, and W. Ketterle, *Reversible Formation of a Bose-Einstein Condensate*, Phys. Rev. Lett. **81**, 2194 (1998).
- [Skl02a] S. E. Sklarz, I. Friedler, D. J. Tannor, Y. B. Band, and C. J. Williams, *Flat-phase loading of a Bose-Einstein condensate into an optical lattice*, Phys. Rev. A **66**, 053620 (2002).
- [Skl02b] S. E. Sklarz and D. J. Tannor, *Loading a Bose-Einstein condensate onto an optical lattice: An application of optimal control theory to the nonlinear Schrödinger equation*, Phys. Rev. A **66**, 053619 (2002).
- [Sna98] M. J. Snadden, J. M. McGuirk, P. Bouyer, K. G. Haritos, and M. A. Kasevich, *Measurement of the Earth's Gravity Gradient with an Atom Interferometer-Based Gravity Gradiometer*, Phys. Rev. Lett. **81**, 971 (1998).
- [Sto05] M. Stoll and T. Köhler, *Production of three-body Efimov molecules in an optical lattice*, Phys. Rev. A **72**, 022714 (2005).
- [TH04] H. J. K. T. Hartmann, F. Keck and S. Mossmann, *Dynamics of Bloch oscillations*, New Journal of Physics **6**, 2 (2004).
- [Tha06] G. Thalhammer, K. Winkler, F. Lang, S. Schmid, R. Grimm, and J. H. Denschlag, *Long-lived Feshbach molecules in a 3D optical lattice*, Phys. Rev. Lett. **96**, 050402 (2006).
- [Tie92] E. Tiesinga, A. Moerdijk, B. J. Verhaar, and H. T. C. Stoof, *Conditions for Bose-Einstein condensation in magnetically trapped atomic cesium*, Phys. Rev. A **46**, R1167 (1992).
- [Unt05] P. Unterwaditzer, *Aufbau eines vollständigen Diodenlasersystems zur Laserkühlung und Detektion von gespeicherten Cs-Atomen*, Master's thesis, University of Innsbruck (2005), download: <http://www.ultracold.at>.
- [Wan37] G. H. Wannier, *The Structure of Electronic Excitation Levels in Insulating Crystals*, Phys. Rev. **52**, 191 (1937).

- [Web03a] T. Weber, *Bose-Einstein Condensation of Optically Trapped Cesium*, Ph.D. thesis, University of Innsbruck (2003), download: <http://www.ultracold.at>.
- [Web03b] T. Weber, J. Herbig, M. Mark, H.-C. Nägerl, and R. Grimm, *Bose-Einstein Condensation of Cesium*, *Science* **299**, 232 (2003).
- [Web03c] T. Weber, J. Herbig, M. Mark, H.-C. Nägerl, and R. Grimm, *Three-body recombination at large scattering lengths in an ultracold atomic gas*, *Phys. Rev. Lett.* **91**, 123201 (2003), doi10.1103/PhysRevLett.91.123201.
- [Win06] K. Winkler, G. Thalhammer, F. Lang, R. Grimm, J. H. Denschlag, A. J. Daley, A. Kantian, H. P. Büchler, and P. Zoller, *Repulsively bound atom pairs in an optical lattice*, *Nature* **441**, 853 (2006).
- [Wit05] D. Witthaut, M. Werder, S. Mossmann, and H. J. Korsch, *Bloch oscillations of Bose-Einstein condensates: Breakdown and revival*, *Physical Review E* **71**, 036625 (2005).
- [Zen34] C. Zener, *The Theory of the Change in Resistance in a Magnetic Field*, *Proceedings of the Royal Society of London. Series A* **145**, 268 (1934).
- [Zwe03] W. Zwerger, *Mott-Hubbard transition of cold atoms in optical lattices*, *Journal of Optics B* **5**, S9 (2003).



# Danke

Nicht fehlen darf natürlich die Danksagung.

Als erstes gebührt der Dank meinem Betreuer Hanns-Christoph Nägerl - denn ohne ihn gäbe es diese Diplomarbeit nicht. Als höchst engagierter Forscher und Professor schafft es Hanns-Christoph dennoch für allfällige Fragen immer zur Verfügung zu stehen.

Ich möchte auch Rudi Grimm dafür danken, mir eine Diplomarbeit in seiner Arbeitsgruppe ermöglicht zu haben.

Ganz herzlich bedanken möchte ich mich bei Mattias und Elmar, quasi Pilot und Co-Pilot im CsIII Labor. Als Doktoranden waren sie es, die mein Unwissen und meine Tollpatschigkeit 'auszubaden' hatten. Besonders oft musste Elmar 'dran glauben'. Mit seiner ruhigen Art (muss wohl an Udo Jürgens liegen?) hat er es immer wieder geschafft, mir so manches 'geheimnisvolles' Konzept näher zu bringen. Danke Mattias, Danke Elmar.

Für einen gutes 'Laborklima' mitverantwortlich war sicherlich auch 'Toni Superlegal', dessen heitere Art immer wieder für gute Stimmung sorgte. Während der Zeit des Verfassens war es auch 'El Boludo', der meine Motivation mit seinem entspannten Humor auf Kurs brachte. Gracias ca'on.

Ein grosses Danke auch dem Rest der Truppe, für die ausgesprochene Hilfsbereitschaft bei technischen, physikalischen oder sonstigen Problemchen die mir im Zuge dieser Diplomarbeit so manches Kopfzerbrechen bereiteten, aber vorallem für die kollegiale Atmosphäre.

In Bezug auf diese Arbeit möchte ich ausserdem Andrew, Orlaith und 'The Niko-dude' danken. Als 'native english-speakers' haben Sie sich die qualvolle Mühe gemacht Teile des Manuskripts korrekturlesen.